

Electronic Thesis and Dissertation Repository

---

4-22-2014 12:00 AM

## Design and Development of a Surgical Robot for Needle-Based Medical Interventions

Mostafa Hadavand, *The University of Western Ontario*

Supervisor: Dr. Rajni Patel, *The University of Western Ontario*

Joint Supervisor: Dr. Michael Naish, *The University of Western Ontario*

A thesis submitted in partial fulfillment of the requirements for the Master of Engineering Science degree in Biomedical Engineering

© Mostafa Hadavand 2014

Follow this and additional works at: <https://ir.lib.uwo.ca/etd>



Part of the [Biomedical Devices and Instrumentation Commons](#)

---

### Recommended Citation

Hadavand, Mostafa, "Design and Development of a Surgical Robot for Needle-Based Medical Interventions" (2014). *Electronic Thesis and Dissertation Repository*. 1994.  
<https://ir.lib.uwo.ca/etd/1994>

This Dissertation/Thesis is brought to you for free and open access by Scholarship@Western. It has been accepted for inclusion in Electronic Thesis and Dissertation Repository by an authorized administrator of Scholarship@Western. For more information, please contact [wlsadmin@uwo.ca](mailto:wlsadmin@uwo.ca).

DESIGN AND DEVELOPMENT OF A SURGICAL ROBOT FOR  
NEEDLE-BASED MEDICAL INTERVENTIONS  
(Thesis format: Monograph)

by

Mostafa Hadavand

Graduate Program in Biomedical Engineering

A thesis submitted in partial fulfillment  
of the requirements for the degree of  
Master of Science

The School of Graduate and Postdoctoral Studies  
The University of Western Ontario  
London, Ontario, Canada

© Mostafa Hadavand 2014

## Abstract

Lung cancer is the leading cause of cancer related deaths. If diagnosed in a timely manner, the treatment of choice is surgical resection of the cancerous lesions followed by radiotherapy. However, surgical resection may be too invasive for some patients due to old age or weakness. An alternative is minimally invasive needle-based interventions for cancer diagnosis and treatment.

This project describes the design, analysis, development and experimental evaluation of a modular, compact, patient-mounted robotic manipulator for lung cancer diagnosis and treatment. In this regard, a novel parallel Remote Centre of Motion (RCM) mechanism is proposed for minimally invasive delivery of needle-based interventions. The proposed robot provides four degrees of freedom (DOFs) to orient and move a surgical needle within a spherical coordinate system. There is an analytical solution for the kinematics of the proposed parallel mechanism and the end-effectors motion is well-conditioned within the required workspace. The RCM is located beneath the skin surface to minimize the invasiveness of the surgical procedure while providing the required workspace to target the cancerous lesions. In addition, the proposed robot benefits from a design capable of measuring the interaction forces between the needle and the tissue. The experimental evaluation of the robot has proved its capability to accurately orient and move a surgical needle within the required workspace. Although this robotic system has been designed for the treatment of lung cancer, it is capable of performing other procedures in the thoracic or abdominal cavity such as liver cancer diagnosis and treatment.

**Keywords:** Surgical robotics, needle-based interventions, cancer diagnosis and treatment

## Acknowledgement

First, I would like to thank my supervisors Dr. Patel and Dr. Naish for giving me the opportunity to accomplish this research work at CSTAR. I also wish to express my gratitude to Dr. Richard Malthaner for his clinical advice and valuable comments through out the project.

Special thanks to my dear friend, Iman Khalaji, for his support and sincere friendship during my stay in London and also for helping me during the final experiments. My gratitude also goes to my amazing friends at CSTAR, Ali, Farokh, Nima, Amir, Mahta, Mahya, and Saeed for encouraging me. Special thanks belongs to Christopher Ward and Abelardo Escoto for their technical support during my research work at CSTAR.

Furthermore, without the assistance of the University Machine Services at the University of Western Ontario, the final prototype of the proposed robot would not have been completed. The help and patience of Dan Sweiger and his team is greatly appreciated.

Words fail to express the appreciation I have for my wife Samira whose love, dedication and persistent confidence in me has taken a load off my shoulders. Her kindness and sincere support has always been comforting.

Last but not least, I am thankful to my kind parents who means a lot to me. My parents have provided their unconditional love and support since my childhood, and I am deeply indebted to them and love them from the bottom of my heart.

This research was supported by the Natural Sciences and Engineering Research Council (NSERC) of Canada under grants RGPIN-1345 (R.V. Patel), and 312383-2010 (M.D. Naish); and by an NSERC-CIHR (Canadian Institutes for Health Research) Collaborative Health Research Projects Grant #398137-2011 (PI: R.V. Patel); and by infrastructure grants from the Canada Foundation for Innovation awarded to CSTAR and to Western University. Financial support for M. Hadavand has also been provided through an NSERC Collaborative Research and Training Experience (CREATE) program grant #371322-2009 in Computer-Assisted Medical Interventions (CAMI).

# Contents

<b>Certificate of Examination</b>	<b>ii</b>
<b>Abstract</b>	<b>ii</b>
<b>Acknowledgements</b>	<b>iii</b>
<b>List of Figures</b>	<b>viii</b>
<b>List of Tables</b>	<b>xi</b>
<b>Nomenclature and Acronyms</b>	<b>xii</b>
<b>1 Introduction</b>	<b>1</b>
1.1 Motivation . . . . .	1
1.1.1 Lung Cancer . . . . .	1
1.1.2 Minimally Invasive Needle-Based Interventions . . . . .	1
1.1.3 Minimally Invasive Needle-Based Interventions vs Percutaneous Interventions . . . . .	2
1.1.4 Robotics-Assisted Minimally Invasive Cancer Diagnosis and Treatment	3
1.2 Needle-based Interventions for Lung Cancer Diagnosis and Treatment . . . . .	3
1.2.1 Needle Biopsy . . . . .	3
Manual Needle Biopsy . . . . .	3
1.2.2 Ablation . . . . .	4
1.2.3 Brachytherapy . . . . .	6
1.3 Project Goals . . . . .	6
1.4 Challenges . . . . .	7
1.5 Contributions . . . . .	8
1.6 Organization of Thesis . . . . .	9
Chapter 1 – Introduction . . . . .	9
Chapter 2 – Literature Review . . . . .	9
Chapter 3 – Conceptual Design . . . . .	9
Chapter 4 – Detailed Design . . . . .	9
Chapter 5 – Kinematic Analysis . . . . .	10
Chapter 6 – Simulation . . . . .	10
Chapter 7 – Evaluation of the Final Prototype . . . . .	10
Chapter 8 – Conclusion . . . . .	10

<b>2</b>	<b>Literature Review</b>	<b>11</b>
2.1	Introduction and History of Cancer Diagnosis and Treatment . . . . .	11
2.2	Current Technologies for Needle-Based Interventions . . . . .	12
2.2.1	AcuBot Robotic System . . . . .	12
2.2.2	INNOMOTION Robotic System . . . . .	13
2.2.3	Robot-Assisted Minimally Invasive Lung Brachytherapy . . . . .	14
2.2.4	Percutaneous Needle-Insertion Robot for Prostate Brachytherapy . . . . .	15
2.2.5	Motions of the Robot Relative to the Patient . . . . .	17
2.2.6	Ultrasound-Guided Motion Adaptive Needle-Insertion Instrument (UMI) . . . . .	17
2.2.7	CT-Bot, a Robotic System for CT-Guided Percutaneous Procedures with Haptic Feedback . . . . .	18
2.2.8	Robopsy . . . . .	19
2.3	Conclusion . . . . .	20
<b>3</b>	<b>Conceptual Design</b>	<b>21</b>
3.1	Introduction . . . . .	21
3.2	Design Requirements . . . . .	21
3.2.1	Required Degrees of Freedom and Workspace . . . . .	21
3.2.2	Compact, Patient-Mounted Design . . . . .	22
3.2.3	Remote Centre of Motion (RCM) . . . . .	22
3.2.4	Required Force/Torque . . . . .	23
3.2.5	Modular Design to Support Different Needle Sizes . . . . .	24
3.2.6	Size of Trocar . . . . .	24
3.3	Existing RCM Mechanisms . . . . .	24
3.3.1	Single-Revolute-Joint RCM Mechanisms . . . . .	25
	Serial Sequence . . . . .	25
	Parallel Sequence . . . . .	26
3.3.2	Circular-Prismatic-Joint RCM Mechanisms . . . . .	26
	Probot . . . . .	27
	Light Endoscope Robot (LER) . . . . .	27
3.4	Parallelogram-Based RCM Mechanisms . . . . .	28
	Blue Dragon Robotic System . . . . .	28
	Neurobot . . . . .	28
	Tool-Offset Problem in Double Parallelogram Mechanism . . . . .	29
	The daVinci Robotic Arms (Device Holders) . . . . .	30
3.4.1	A Spherical RCM Mechanism . . . . .	30
	The Raven Surgical Robotic System . . . . .	32
	MC2E Robotic Arm . . . . .	32
3.4.2	Instantaneous RCM mechanism . . . . .	33
	A Compact MR compatible Surgical Manipulator . . . . .	33
3.4.3	A Passive Joint RCM Mechanism . . . . .	34
3.4.4	Software-Based RCM . . . . .	35
	DLR MiroSurge Robotic System . . . . .	35
3.4.5	Conclusions Regarding Existing RCM Mechanisms . . . . .	36
3.5	Choosing a proper RCM Mechanism . . . . .	37

3.5.1	Comparing and Ranking the RCM Mechanism . . . . .	37
3.6	Conclusion . . . . .	38
<b>4</b>	<b>Detailed Design</b>	<b>39</b>
4.1	Introduction . . . . .	39
4.2	Robot Design . . . . .	39
4.2.1	Parallel RCM Mechanism . . . . .	39
4.2.2	Proper location of RCM . . . . .	40
4.2.3	Main Leg of the Robot . . . . .	41
4.2.4	Degrees of Freedom . . . . .	43
4.2.5	Direct Force Measurement . . . . .	44
4.2.6	Crank–Slider Mechanism to Actuate the Pitch And Yaw DOFs . . . . .	44
4.2.7	Linear Insertion . . . . .	45
4.2.8	Modular Design to Support Different Needle Sizes . . . . .	47
4.2.9	Roll Motion . . . . .	47
4.3	Finite Element Analysis (FEA) . . . . .	49
4.3.1	FEA of Critical linkages . . . . .	49
4.4	Actuation . . . . .	51
4.5	Conclusion . . . . .	51
<b>5</b>	<b>Kinematic Analysis</b>	<b>52</b>
5.1	Forward Kinematics . . . . .	52
5.2	Inverse Kinematics . . . . .	55
5.3	Workspace . . . . .	56
5.4	Velocity Analysis . . . . .	56
5.4.1	Velocity Propagation . . . . .	56
5.4.2	Jacobian Matrix . . . . .	59
5.5	Quantitative Measures of Workspace Attributes . . . . .	60
5.5.1	Singularities . . . . .	60
5.5.2	Manipulability Measure . . . . .	61
5.5.3	Isotropy and Condition Number . . . . .	61
Isotropy of the Parallel Mechanism . . . . .	62	
Manipulability Ellipsoid . . . . .	63	
Manipulability Ellipsoid for Each Leg of the Robot . . . . .	64	
5.6	Crank–Slider Mechanism . . . . .	65
5.7	Conclusion . . . . .	67
<b>6</b>	<b>Simulation</b>	<b>68</b>
6.1	Introduction . . . . .	68
6.2	Forward Kinematics Evaluation . . . . .	69
6.3	Inverse Kinematics Evaluation . . . . .	70
6.4	Velocities and Jacobian Evaluation . . . . .	70
6.5	Effect of Possible Mechanical Imperfections . . . . .	72
6.5.1	Effect of Backlash on Positioning Accuracy . . . . .	72
6.5.2	Effect of Possible Machining Errors . . . . .	73

6.6	Conclusion . . . . .	76
<b>7</b>	<b>Evaluation of the Final Prototype</b>	<b>78</b>
7.1	Introduction . . . . .	78
7.2	Overview of the Final Prototype . . . . .	78
7.3	The Graphical User Interface . . . . .	84
7.4	Testing and Validation . . . . .	84
7.4.1	Workspace Evaluation . . . . .	84
7.4.2	RCM Assessment . . . . .	86
7.4.3	Path Planning . . . . .	86
7.4.4	Force Measurements . . . . .	90
7.5	Conclusion . . . . .	91
<b>8</b>	<b>Conclusions</b>	<b>93</b>
8.1	Summary . . . . .	93
8.2	Concluding Remarks . . . . .	93
	Compact, Patient-Mounted Design . . . . .	94
	Novel Parallel RCM Mechanism . . . . .	94
	Measurement of Needle–Tissue Interaction . . . . .	94
8.3	Recommendations and Future Work . . . . .	94
8.3.1	Mechanical Recommendations . . . . .	94
8.3.2	Control Recommendations . . . . .	95
8.3.3	Testing and Validation Recommendations . . . . .	96
<b>A</b>	<b>Kinematics Equations</b>	<b>97</b>
	<b>Bibliography</b>	<b>100</b>
	<b>Curriculum Vitae</b>	<b>105</b>



# List of Figures

1.1	TNM staging of lung cancer [11]. . . . .	2
1.2	Manual biopsy of lung cancer using CT images [22]. . . . .	4
1.3	Electrode configuration of 4 different systems; (a): Multi Expandable 8-tine monopolar dry electrode; (b) Multi-Expandable 3-tine monopolar dry electrode; (c) Single monopolar perfusion electrode; and (d) Single monopolar dry, cool-tip electrode (internally cooled electrode) [33] . . . . .	5
1.4	The propose robotic system for minimally invasive delivery of needle based interventions. . . . .	8
2.1	The surgical field during the first robot-assisted cancer diagnosis under image guidance [44]. . . . .	12
2.2	PAKY-RCM robot connected to a passive arm which can be mounded on the surgical bed [55, 66]. . . . .	13
2.3	AcuBot robotic system attached during a phantom study [77]. . . . .	14
2.4	INNOMOTION robotic system [88]. . . . .	14
2.5	The experimental test-bed for lung brachytherapy consists of a VATS box, surgical robotic arms, a seed injector, an ultrasound machine, an electromagnetic tracking system, video monitors and an endoscope [99]. . . . .	15
2.6	Graphical user interface for ultrasound navigation [99]. . . . .	16
2.7	A robotic manipulator for 3D Ultrasound Guided Percutaneous Needle Insertion [1010]. . . . .	16
2.8	Ultrasound-guided, motion adaptive device for needle insertion [1111]. . . . .	17
2.9	Prototype of CT-bot under test [1212, 1313]. . . . .	18
2.10	Parallel mechanism of CT-Bot robotic system[1212]. . . . .	19
2.11	Robopsy system[1414]. . . . .	19
2.12	Schematic view of Robopsy mechanism [1414]. . . . .	20
3.1	The required degrees of freedom. . . . .	22
3.2	Experimental setup to measure tissue-needle interaction forces . . . . .	23
3.3	Axial forces applied to a 13 GA ablation probe inserted into porcine lung tissue. . . . .	23
3.4	Single revolute joint RCM. . . . .	25
3.5	Schematic of a 3R (Revolute) wrist of Puma 560 [1515]. . . . .	25
3.6	The parallel sequence of the single revolute mechanism used by Immersion [1616]. . . . .	26
3.7	Circular prismatic joint RCM mechanism. . . . .	26
3.8	Details of Probot’s RCM mechanism.[1717, 1818] . . . . .	27
3.9	LER mechanism (obtained from [1919]) . . . . .	27

3.10	Different configurations of a double parallelogram RCM mechanism [2020]	28
3.11	parallelogram-based RCM mechanism of Blue Dragon robotic system [2121]	29
3.12	Neurobot [2222]	29
3.13	Basic configuration of a double parallelogram mechanism (obtained from [2323])	30
3.14	Modified double-parallelogram mechanism [2424]	30
3.15	The parallelogram mechanism used in daVinci robotic arms	31
3.16	Spherical RCM mechanism.	31
3.17	Serial and parallel configurations of a Spherical RCM mechanism [?]	32
3.18	The Raven surgical manipulator [2525].	32
3.19	The RCM mechanism of MC2E [2626].	33
3.20	An example of instantaneous RCM mechanisms [2020].	34
3.21	MR compatible robot with an instantaneous RCM mechanism [2727].	34
3.22	AESOP robotic arm [2828].	35
3.23	A Mitsubishi, PA10-7C robot used in minimally invasive surgery configuration [2929].	36
3.24	The DLR MiroSurge robotic arm (obtained from [3030]).	36
4.1	The proposed patient-mounted robot with a novel parallel RCM mechanism.	40
4.2	The main leg of the parallel mechanism and its connection to the ancillary leg.	41
4.3	Inclining each leg of the robot to move the RCM downward.	42
4.4	General configuration of a double parallelogram mechanism.	42
4.5	The main leg of the proposed parallel RCM mechanism.	43
4.6	Details of the mechanism and its degrees of freedom.	43
4.7	Surgical needle goes through a cannula to avoid interaction with the trocar.	44
4.8	The crank–slider mechanism used to actuate the pitch and yaw DOFs.	45
4.9	Details of linear insertion actuation.	46
4.10	Linear insertion actuation force.	47
4.11	Needle adaptor and linear insertion actuation.	48
4.12	Details of roll motion actuation.	48
4.13	Finite element analysis.	50
4.14	Finite element analysis of critical link number 1.	50
4.15	Finite element analysis of critical link number 2.	50
5.1	Coordinate frames attached to the right leg of the robot.	53
5.2	Coordinate frames attached to the left leg of the robot.	55
5.3	Robot’s workspace inside its base coordinate system.	57
5.4	Manipulability measure within the required workspace.	61
5.5	Directional uniformity within the robot workspace.	63
5.6	Distribution of the motion ratio with the workspace.	63
5.7	Manipulability ellipsoid for each leg of the robot.	64
5.8	Crank–slider mechanism.	65
5.9	Geometry-based solution for crank–slider mechanism.	66
6.1	Model of the robot in SimMechanics.	68
6.2	End-effector’s absolute position along the X axis.	69

6.3	End-effector's absolute position along the Y axis. . . . .	69
6.4	End-effector's absolute position along the Z axis. . . . .	70
6.5	The desired circular path for tracking. . . . .	71
6.6	Tracking a circular path. . . . .	71
6.7	End-effector's absolute velocity along the X axis. . . . .	72
6.8	End-effector's absolute velocity along the Y axis. . . . .	72
6.9	End-effector's absolute velocity along the Z axis. . . . .	73
6.10	End-effector's absolute velocity along the Y axis. . . . .	74
6.11	Positioning error caused by machining imperfections along X axis. . . . .	75
6.12	Positioning error caused by machining imperfections along Y axis. . . . .	75
6.13	Positioning error caused by machining imperfections along Z axis. . . . .	76
6.14	Maximum possible positioning error caused by the joint deviations. . . . .	76
6.15	Cylindrical joints that prevent the mechanism from locking due to possible mechanical imperfections. . . . .	77
7.1	The final prototype of the robot. . . . .	78
7.2	The pitch and Yaw DOFs. . . . .	79
7.3	The main and ancillary legs of the robot's mechanism. . . . .	79
7.4	The belt tensioning mechanism. . . . .	80
7.5	The crank–slider mechanism. . . . .	81
7.6	The connection between two legs of the mechanism. . . . .	81
7.7	The Roll and linear insertion degrees of freedom. . . . .	82
7.8	The surgical needle supported by the robotic manipulator. . . . .	82
7.9	The stationary based of the robot. . . . .	83
7.10	The linkage of the robot's legs. . . . .	83
7.11	The connection between the tow legs. . . . .	83
7.12	Graphical user interface to control the robot and monitor the applied forces. . . . .	85
7.13	Range of motion for the Pitch and Yaw degrees of freedom. . . . .	85
7.14	Tracking the tip of the needle using the optical tracking system. . . . .	86
7.15	Tracking the RCM position along the X axis of the camera. . . . .	87
7.16	Tracking the RCM position along the Y axis of the camera. . . . .	87
7.17	Tracking the RCM position along the Z axis of the camera. . . . .	88
7.18	Tracking a circular path by the tip of the needle. . . . .	88
7.19	The generated circular path by the tip of the needle in camera coordinate frame and its plane. . . . .	89
7.20	The generated circular path and desired one in robot's base coordinate frame. . . . .	89
7.21	Error of tracking the circular path by the tip of the needle. . . . .	90
7.22	Needle insertion into animal tissue using the proposed patient-mounted robot. . . . .	91
7.23	Insertion force applied to the surgical needle during the experiment. . . . .	91

# List of Tables

3.1	List of design requirements . . . . .	24
3.2	Comparing available RCM mechanisms. . . . .	37
4.1	Finite element analysis of the critical linkages . . . . .	49
4.2	Details of actuation for each degree of freedom. . . . .	51
5.1	Denavit-Hartenberg Parameters . . . . .	54
5.2	Range of motion at each degree of freedom. . . . .	56
6.1	The positioning errors caused by actuation backlash. . . . .	74

# Nomenclature and Acronyms

## Latin Letters

<i>L</i>	Length of the linkages
<i>d</i>	Prismatic joint variable related to the insertion degree of freedom
<i>J</i>	The Jacobian matrix
<i>T</i>	Transformation matrix between the coordinate frames
<i>S</i>	Sliding motion of the crank–slider mechanism

## Greek Letters

$\theta$	Joint variable related to a revolute joint
$\alpha$	Incline angle to move the RCM downward
$\phi$	Offset angle of the mechanism linkages
$\beta$	Rotational motion of the crank-slider

## Acronyms

RCM	Remote Centre of Motion
CT	Computed Tomography
DOF	Degree Of Freedom
DOFs	Degrees Of Freedom
CPT	Counts Per Minute
HDR	High Dose Rate
LDR	Low Dose Rate
PET	Positron Emission Tomography
SCLC	Small Cell Lung Cancer
NSCLC	Non Small Cell Lung Cancer
TNM	Tumour-Node-Metastasis
RFA	Radio Frequency Ablation
MWA	Micro Wave Ablation
OR	Operation Room
FEA	Finite Element Analysis
PID	Proportional-Integral-Derivative
PI	Proportional-Integral

# Chapter 1

## Introduction

### 1.1 Motivation

#### 1.1.1 Lung Cancer

Lung cancer refers to uncontrolled cell-growth in tissue of the lung. It is the second most common type of cancer in the world and the most common cause of cancer-related deaths. In 2013, it was estimated that more than 25,400 Canadians would have been diagnosed with lung cancer and 20,200 would have died of lung cancer [3131]. In addition, the long term survival rate of lung cancer is reported to be very low [3232]. There are two main types of lung cancer: Non-small Cell Lung Cancer (NSCLC) and Small Cell lung cancer (SCLC). SCLC grows quickly and often spreads to distant parts of the body while NSCLC grows more slowly. NSCLC is the top cause of lung cancer mortality, accounting for 80% of all lung carcinomas. Currently NSCLC staging is specified in TNM<sup>1</sup> system which describes the extent of spread of cancer cells from their original source [11]. Figure 1.11.1 shows the TNM staging of lung cancer. Stage IA and IV are the earliest and the worst prognosis stages of NSCLC, respectively. The staging process is done by using a combination of different imaging modules like CT<sup>2</sup> or PET<sup>3</sup> and biopsy, which provides the clinician with enough information to choose the best treatment alternatives.

#### 1.1.2 Minimally Invasive Needle-Based Interventions

For NSCLC in early stages, surgical resection of the tumour is the safest way to ensure complete removal of cancerous cells; however, many patients cannot undergo surgery due to weakness or old age [3333]. An alternative is minimally invasive needle-based interventions. In these approaches, direct access to the malignant tissue is obtained through inserting surgical needles into the targeted tumour under medical image guidance. Thus, the malignant tissue can be collected for further examination or the therapeutic agents can be delivered to the malignant

---

<sup>1</sup>Tumour-Node-Metastasis, a cancer staging system developed by the American Joint Committee on Cancer (AJCC) and the international Union Against Cancer (UICC).

<sup>2</sup>Computed Tomography.

<sup>3</sup>Positron Emission Tomography.

**TNM STAGING OF LUNG CANCER**

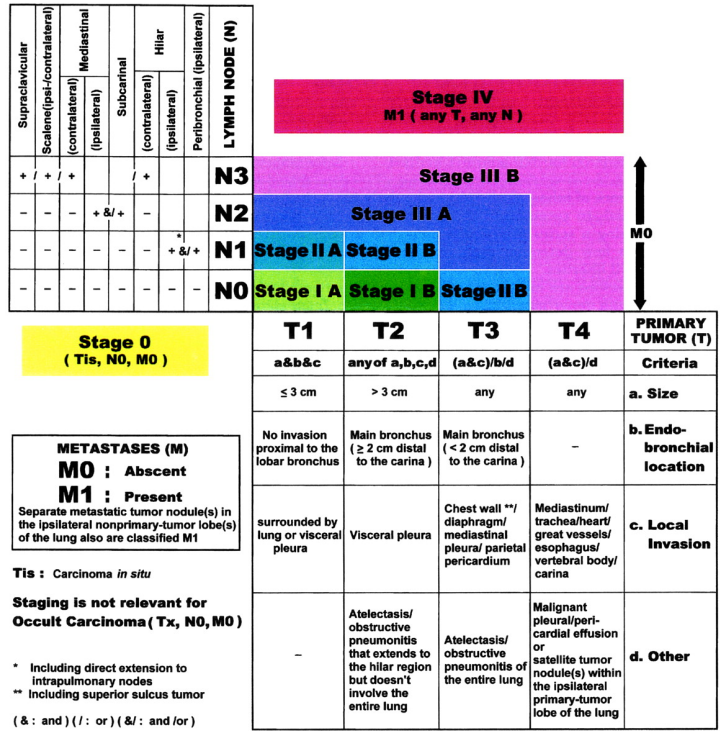


Figure 1.1: TNM staging of lung cancer [11].

cells to eradicate the cancer. Image-guided biopsy, ablation, drug delivery and brachytherapy are examples of such needle-based interventions.

**1.1.3 Minimally Invasive Needle-Based Interventions vs Percutaneous Interventions**

A percutaneous intervention pertains to any medical procedure where access to inner organs or other tissue is done via needle-puncture of the skin. Thus, after passing the skin, it is not possible to reorient the needle and correct the targeting path for reaching tumours. On the other hand, during a minimally invasive needle-based intervention, the surgical needle may be introduced into the patient’s body using a trocar<sup>4</sup>. As a result, it is possible to orient the needle and find the best targeting angles before inserting the needle into tissue. In this regard, during a minimally invasive intervention it may be required to provide a fixed centre of rotation for the surgical tool (i.e., needle) to avoid applying excessive forces into the patient’s body. This constraint has resulted in the idea of using Remote Centre of Motion (RCM) mechanisms for surgical applications.

<sup>4</sup>A trocar is a medical instrument with a sharply pointed end, often three-sided, that is used inside a hollow cylinder (cannula) to introduce this into blood vessels or body cavities.

### **1.1.4 Robotics-Assisted Minimally Invasive Cancer Diagnosis and Treatment**

The success rate of needle-based interventions for soft tissue organs such as the lung and liver highly depends on the precise insertion of the needle into the tissue [3434, 3535]. While advanced imaging technologies such as CT provide accurate localization of cancerous tumours, manual delivery of needle-based interventions often does not provide the accuracy required for the procedure. In addition, the mental registration between medical images and a patient's anatomy is a challenging task for the clinicians. The hazards of radiation exposure during some interventions impose further limitations. In this regard, special purpose surgical robots have been developed to perform image-guided percutaneous procedures.

## **1.2 Needle-based Interventions for Lung Cancer Diagnosis and Treatment**

Needle biopsy is an effective diagnostic procedure to sample suspicious cells detected in medical images. Further examinations on sampled cells can reveal the possible type and stage of cancer. Thus, biopsy is a required procedure for any type of cancer including lung cancer. According to an expert's opinion, for NSCLC in early stages, ablation is the standard therapeutic needle-based intervention if surgical resection is not possible. Brachytherapy is another type of needle-based intervention for cancer treatment which has been shown to be a possible treatment option for lung cancer [3636]. The proposed robotic system is developed to support these three types of needle-based interventions.

### **1.2.1 Needle Biopsy**

Biopsy refers to a surgical procedure during which a small part of tissue is resected for clinical diagnosis purposes. It is claimed that biopsies require high accuracy in targeting the living tissue that needs to be analysed considering the small size of some tumours [3434]. Manual biopsies are routinely performed on tumours of 2-6 cm, while recent CT scans allow for detection of 10 mm and below abnormalities.

#### **Manual Needle Biopsy**

It has been proven that CT-guided manual biopsy is a relatively accurate way of diagnosing cancerous lesions within the lung [3737]. The manual biopsy procedure begins with a CT scan of the thorax to locate the tumour. Usually, a radio-opaque targeting grid is attached to the patient that helps the interventionist to locate the proper entry point on the patient's body. Using this initial scan, the interventionist plans the needle's insertion angle and depth from the entry point which was located by the grid. Then, he/she slides the patient out of the CT scanner and manually starts to insert the needle based on the initial measurements. This procedure is iterative and the interventionist insert needle step by step while checking the result by other successive CT images. Asking the patient to hold his/her breath helps to improve the accuracy of the procedure. The manual biopsy procedure may take 2 h, especially



when samples are acquired from multiple sites within the lesion, requiring post-insertion needle adjustment [1414]. The interventionist has to accurately orient the needle prior to insertion to avoid surrounding structures which can be often stressful and fatiguing. The discomfort for the patient during the procedure and long-term radiation exposure are other disadvantages of manual biopsy.

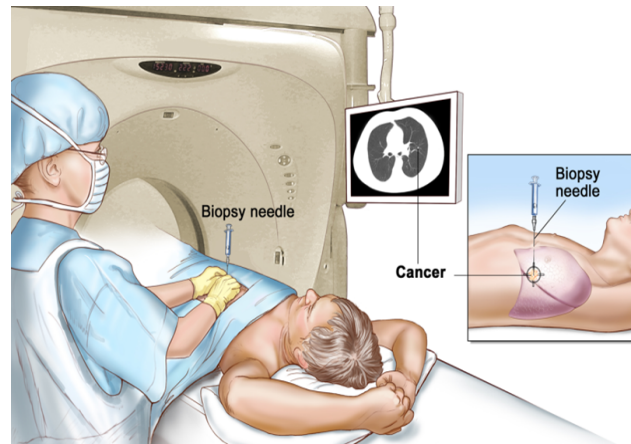


Figure 1.2: Manual biopsy of lung cancer using CT images [22].

Using the standard manual biopsy, lesions smaller than 10 mm cannot be reliably targeted, and the overall successful sample acquisition rate is only 77% [3737]. In addition, it is not possible to reliably target specific portions of a lesion, such as those that have been shown to be metabolically active on a PET scan [1414]. Multiple needle insertions performed after the needle has crossed the lung's pleurae increase the risk of pneumothorax<sup>5</sup>. Some interventionists do attempt to biopsy sub-centimeter lesions but tissue yield plummets as lesion size decreases [3737]. For lesions between 5 and 10 mm in diameter, the accuracy is 52%, and for lesions less than 5 mm, the manual biopsies are often inadequate. Sub-centimeter lesions may also significantly require more needle passes, thus increasing the risk of pneumothorax.

However, the manual biopsy is an effective diagnosis procedure, but it lacks sufficient accuracy and stability for precise sampling of small cancerous lesions. Moreover, it takes a lot of effort and time to perform the procedure which may be fatiguing for the interventionist and also harmful for the patient. These limitations have urged researchers to develop robotic needle insertion systems that work under image guidance and improve the accuracy and stability of the biopsy procedure considerably.

## 1.2.2 Ablation

Ablation refers to a group of therapies which involve placing a special kind of surgical needle (i.e., probe) inside a tumour which uses extreme temperatures to destroy the tumour. There are three main kinds of ablation: Radio-Frequency Ablation (RFA), Microwave Ablation (MWA), and Cryo ablation. The RF and Microwave ablation devices implement high temperatures to

<sup>5</sup>A pneumothorax (pl. pneumothoraces) is an abnormal collection of air or gas in the pleural space that separates the lung from the chest wall and which may interfere with normal breathing.

“cook” the cancerous cells, while during Cryo ablation very low temperatures are used to freeze the tumour.

While RF and Microwave ablation are common treatment options for lung cancer, Cryo ablation is not currently a standard procedure due to complications related to its equipment. During RFA (Radio Frequency Ablation), high-frequency alternating current is transferred into the tissue. The current creates molecular friction resulting in local production of heat, denaturation of proteins and cell membrane disintegration [33]. RFA is the most common modality which is currently used in hospitals because of its effectiveness in both surgical and percutaneous procedures and also ease of use [3838]. However, RFA needs to conduct electricity through the patient’s body which causes a basic restriction in producing high temperatures. In this regard, as temperatures reach  $100^{\circ}\text{C}$  and boiling occurs, increased impedance limits further deposition of electricity into tissue [3939]. To minimize this effect, a number of different algorithms of energy deposition and several different types of electrodes have been used [3838]. Electrode types include multitined expandable electrodes, perfusion electrodes, and cooled-tip RF probes. Figure 1.31.3 depicts different types of RF probes.

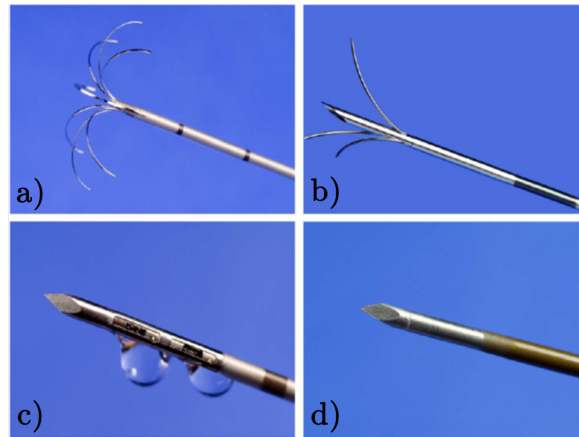


Figure 1.3: Electrode configuration of 4 different systems; (a): Multi Expandable 8-tine monopolar dry electrode; (b) Multi-Expandable 3-tine monopolar dry electrode; (c) Single monopolar perfusion electrode; and (d) Single monopolar dry, cool-tip electrode (internally cooled electrode) [33]

A further limitation associated with RFA is the relatively small active heating zone produced by ionic agitation which is on the order of a few millimeter [4040]. In RFA the majority of tissue heating is done by thermal conduction which descends exponentially away from the source. Thus, for a large tumour several RFA probes may be used to cover the whole cancerous area. Heat distribution around the probe is a function of tissue impedance, native tissue temperature, thermal conductivity and heat loss through the blood flow [33]. This makes it really difficult to determine the ablation zone during RFA.

On the other hand, MWA offers many of the advantages of RFA while possibly overcoming some of the limitations [3838]. MW ablation does not rely on conducting electricity into the tissue; thus, there is no limitation to produce temperatures greater than  $100^{\circ}\text{C}$ . This enables MW ablation to have a relatively larger ablation zone, faster treatment time, and more complete

tumour kill [3838]. Additionally, MW ablation has a much broader power field than RF ablation (up to 2 cm in diameter) [4141]. This may allow for larger zones of thermal ablation and a more uniform tumour kill which makes MW ablation a preferred method for large tumour eradication. The protective effect of blood flow near the vascular areas is another issue that reduces the effectiveness of ablation. Blood flow acts as a cooling system which is referred as the heat sink effect. The cooling effect of blood flow is most pronounced within the zone of conductive rather than active heating. Thus MW ablation which has a larger power field may also enhance treatment of perivascular tissue in comparison with RFA.

Both RFA and MW ablation are regarded as standard treatment procedures for lung tumour eradication. The size of the tumour and existing equipment are the main contributing factors to choose the type of ablation probe.

### 1.2.3 Brachytherapy

Brachytherapy also known as internal radiotherapy from its Greek derivation refers to “short range therapy” and has been described as the first form of conformal radiation therapy [4242]. In this method, radiation sources are placed within or very close to the tumour, allowing higher cancerous to normal tissue eradication in comparison with external radiation therapy. Cancers with clinically and well-defined margins, usually those in early stages with a low risk of regional and metastatic spread, are the most suitable for brachytherapy. There are two main categories of brachytherapy regarding the dose rate:

- Low dose rate (LDR): a range of 4.0 to 2 Gy<sup>6</sup> per hour. In clinical practice, the usual range is 3.0 to 1 Gy per hour, although in some countries this is extended to 1.9 Gy per hour.
- High dose rate (HDR) over 12 Gy per hour, which must be delivered by an automatic afterloading device.

In LDR brachytherapy, small radioactive seeds are placed near or inside the targeted tumour to eradicate the cancerous cells gradually. However, this type of brachytherapy is not a standard treatment practice for lung cancer due to the possibility of migration of the radioactive seeds from their desired location after the intervention is done. On the other hand, high dose rate brachytherapy has been shown to be effective for lung cancer treatment and it can be considered as a possible treatment option [3636].

## 1.3 Project Goals

The main objective of this project is effective delivery of needle-based interventions for lung cancer diagnosis and treatment. Here the term needle is used to refer to both needles and probes used for biopsy, brachytherapy and ablation. It is expected that tumours embedded within lung tissue can be automatically targeted based on information obtained from preoperative CT images.

---

<sup>6</sup>One gray (Gy) is the absorption of one joule of energy, in the form of ionizing radiation, per kilogram of matter.

To achieve this goal, development of a compact, patient-mounted surgical robot was undertaken to target the cancerous tumours embedded within the lung and insert an appropriate surgical needle inside cancerous lesions to extract tissue samples from internal organs or eradicate cancerous cells. The location of the tumour relative to the patient's anatomy is known from a combination of preoperative CT imaging and tactile/ultrasound/kinesthetic sensors. On the other hand, the proposed robotic manipulator is attached to the patient's body and can be registered into the medical images, so the exact location of the targeted tumour relative to the robot's base is constantly known during the intervention. The robot provides the required degrees of freedom to orient and move a surgical needle within a spherical coordinate system to target the exact position of the tumour. The robot proposed in this project is developed to support different types of needle-based interventions including needle biopsy, RF and MW ablation and HDR brachytherapy. The mechanical design, along with the use of a trocar to introduce the needle into the body cavity, makes it possible to directly measure the interaction forces between the needle and the tissue. It benefits from a novel parallel Remote Centre of Motion (RCM) mechanism with a simple analytical kinematic solution. The proposed mechanism provides four decoupled DOFs and has a good manipulability and directional uniformity within the required workspace. The subcutaneous location of RCM is the main advantage of the proposed robot over the existing patient-mounted robotic systems. It helps to minimize the invasiveness of the surgical procedure while providing the required workspace. The design is compact and lightweight without compromising the structural stiffness of the system. A passive spring-based holder is used to support the weight of the robot while it is attached to the patient's body. Having the robot fixed to the patient's body reduces errors that may be caused by physiological motions such as respiration and repositioning of the patient during the clinical procedure. Figure 1.41.4 shows a CAD model of the proposed robotic system.

## 1.4 Challenges

Access to the lung is made difficult by the presence of the rib cage. In addition, motions caused by respiration and heartbeat make it difficult to target the tumours accurately within lung tissue. The proposed robotics system is intended to be patient-mounted to reduce the errors caused by the patient's motion relative to the bed during the intervention. Thus, a major challenge in the development of the robotics manipulator is the constraint on its size. It is required to be compact so that it can be attached to the patient's body and also fit inside a typical medical imaging scanner. In addition, the surgical needle has to pass through a relatively small trocar (standard trocar size 5 mm). It is also required to have a proper RCM mechanism to reduce trauma to the patient's body. Providing sufficient degrees of freedom with good manipulability and kinematic performance is another challenging requirement for the proposed robot. Direct measurement of interaction forces between the surgical needle and lung tissue required proper mechanical design to integrate a force sensor into the robot's structure. Finally, sterilizability and reducing the overall cost of developing the robotic system are other major challenges.

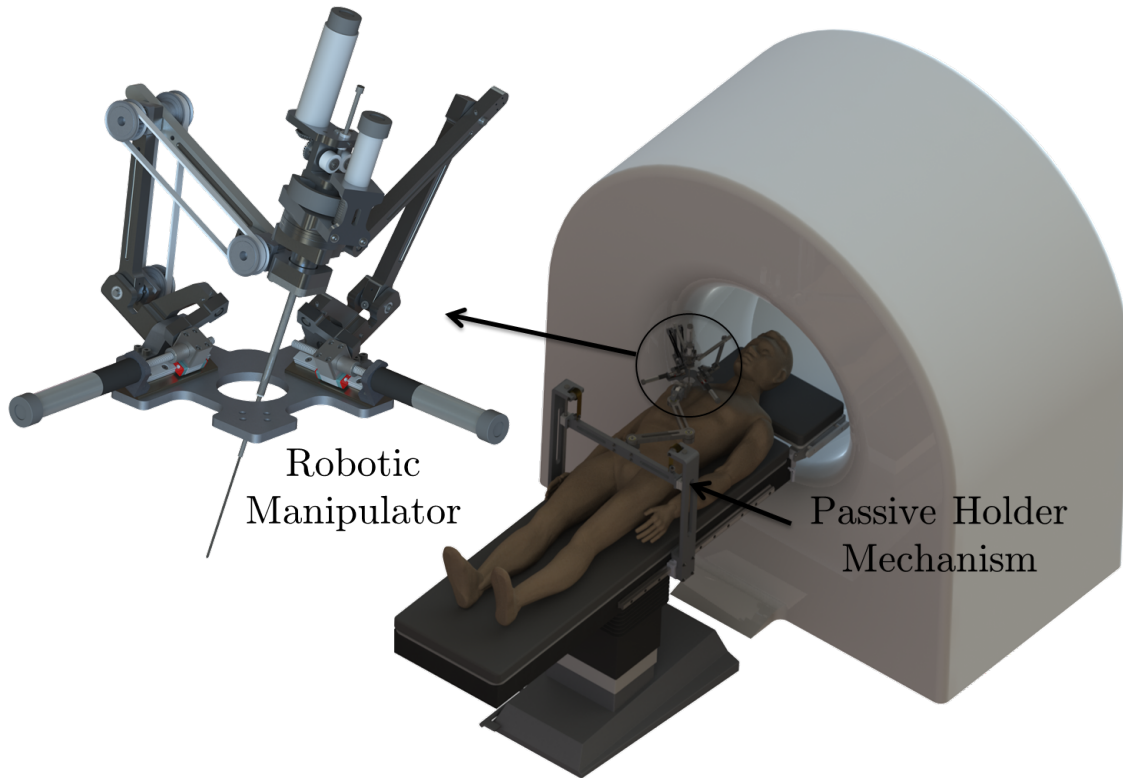


Figure 1.4: The propose robotic system for minimally invasive delivery of needle based interventions.

## 1.5 Contributions

The robot proposed in this project is developed to support different types of needle/probe-based interventions for minimally invasive cancer diagnosis and treatment. For that reason, it has a modular design to support different needle/probe sizes based on the type of the intervention. It is also possible to measure pure interaction forces between the surgical needle and tissue which may be helpful to minimize needle deflection and also confirm the location of the tumour based on stiffness variations. In addition, the robot has a novel parallel RCM mechanism with a simple, analytical kinematic solution. The RCM mechanism provides four decoupled DOFs with a good manipulability and directional uniformity within its workspace. Proper location of the RCM helps to minimize the invasiveness of the surgical procedure while providing the required workspace to orient a surgical needle and target cancerous tumours. The proposed robot benefits from a compact and lightweight design without compromising structural stiffness of the robot which improves its robustness. Although the robot is designed to be lightweight, its weight will be mainly supported by a passive spring-based holder, while it is fixed onto the patient's body. Thus, errors caused by repositioning of the patient during a clinical intervention and presence of physiological motions such as that due to respiration may be reduced.

## 1.6 Organization of Thesis

This thesis is divided into eight chapters that progress through the conceptual design, detailed design, analysis, simulation and validation of the presented robotic manipulator. A brief description of each chapter is as follows:

### Chapter 1 – Introduction

This chapter outlines the main motivations and objectives for this research work. It introduces the technique of needle-based interventions for lung cancer diagnosis and treatment and also identifies the important challenges and restrictions in current techniques and technologies for minimally invasive cancer diagnosis and treatment. In addition, the main challenges of developing a robotic manipulator for effective delivery of needle-based interventions are described and the contributions of this work are summarized.

### Chapter 2 – Literature Review

In this chapter, the state of the art in robotics-assisted needle insertion for cancer diagnosis and treatment is presented. Several current robotic manipulators for cancer diagnosis and treatment are introduced and discussed in detail and their main features and weak points are outlined. Finally, the main challenges and shortcomings in robotic delivery of needle-based interventions are summarized.

### Chapter 3 – Conceptual Design

This chapter outlines the main design requirements of a robotic manipulator that is designed for minimally invasive needle-based interventions for lung cancer diagnosis and treatment. The necessity of having an RCM mechanism is explained and the main difference between a percutaneous procedure and a minimally invasive intervention is discussed. Through a comprehensive investigation, existing RCM mechanisms are introduced, analysed, compared and the most appropriate mechanism for the current application is introduced. Finally, it is concluded that there are several known types of RCM mechanisms and the main contribution is to choose a suitable one and try to apply appropriate modifications to develop an original mechanism capable of satisfying all the design requirements for the current project.

### Chapter 4 – Detailed Design

This chapter covers the entire mechanical design of the proposed robotic manipulator. A novel parallel RCM mechanism capable of providing 4 degrees of freedom (DOFs) to orient and position a surgical needle within a spherical coordinate system is introduced and its mechanical design is discussed in detail. The actuation systems of the four degrees of freedom (pitch, yaw, roll and insertion) are presented and the main feature of the proposed design are highlighted. Finite element analysis of the critical linkages is reported and the selection of the actuators is presented.

### **Chapter 5 – Kinematic Analysis**

In this chapter the kinematic performance of the robot is comprehensively described. It starts with forward and inverse kinematics and continues into velocity analysis and finding the Jacobian matrices for each leg of the robot. In addition, detailed analysis of the crank–slider mechanism is performed to provide a complete analytical solution for the kinematics of the robot. Ultimately, the quantitative measures of the kinematic performance including a manipulability measure and isotropy analysis are presented.

### **Chapter 6 – Simulation**

The simulation model of the robot in the SimMechanics environment(Matlab R2012b, the MathWorks Inc.) is the main focus of this chapter. The simulation environment is used to validate the analytical forward kinematics, inverse kinematics and velocity analysis of the robot. In addition, it is used to study the effect of possible mechanical imperfections such as backlash of the actuators and machining errors on the performance of the robot.

### **Chapter 7 – Evaluation of the Final Prototype**

This chapter describes the final prototype of the robot and its validation. A comprehensive overview of the final prototype is presented and the main features of the design are discussed. Finally, a number of experiments are performed to evaluate the overall performance of the robotic system..

### **Chapter 8 – Conclusion**

This chapter summarizes the work presented in this thesis and offers some recommendations for future work.

# Chapter 2

## Literature Review

Presented in this chapter is an overview of surgical robotic systems developed for cancer diagnosis and treatment. It begins with a historical study of robotics-assisted cancer diagnosis and treatment. It is then followed by a comprehensive investigation of the existing technologies and robotic systems developed for cancer diagnosis and treatment. Finally, the possible improvements for robotics-assisted cancer diagnosis and treatment are outlined.

### 2.1 Introduction and History of Cancer Diagnosis and Treatment

Cancer is the general name of a group of disease originating from uncontrolled cell growth inside the biological tissue. From the dawn of history, people have been writing about this mysterious disease. The oldest description of cancer was discovered in Egypt and dates back to about 3000 BC [4343]. Considering the long history of knowing about this disease, it can be realized that cancer diagnosis and treatment has gone through a slow process. Until near the end of the 20th century, cancer diagnosis often required exploratory surgery [4343]. Starting from 1970s, the development of medical imaging technologies has revolutionized cancer diagnosis and treatment. However, still one of the major concerns in cancer diagnosis and treatment is the ability of delivering therapies and diagnostic tools to the cancerous lesions while minimizing damage to the surrounding healthy tissue and reducing the side-effects for the patient. In this context, much research has been conducted to improve the quality of cancer diagnosis and treatment by reducing the invasiveness level of the medical interventions. Recent advances in medical imaging have enabled clinicians to accurately locate the cancerous lesions but it has been realized that humans are not capable of providing the required accuracy to perform image guided interventions in a minimally invasive manner. Moreover, mental registration between the medical images and the patient's anatomy is a challenging task and in some cases the hazards of radiation exposure impose further limitations on the clinicians. These limitations have provided the motivation for engineers to develop robotic systems capable of performing medical interventions for cancer diagnosis and treatment under image guidance. Historically, the first robot-assisted surgical procedure was performed in 1985 for cancer diagnosis [44]. During this procedure, a standard industrial robot PUMA 560 was used to hold a fixture next to the patient's head to guide a biopsy needle under CT image guidance.



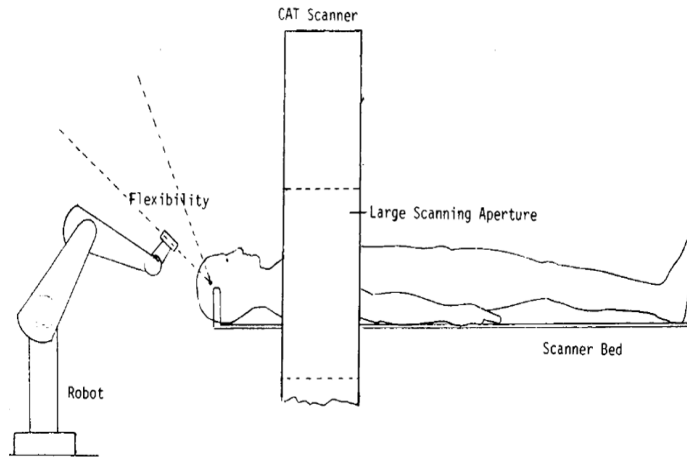


Figure 2.1: The surgical field during the first robot-assisted cancer diagnosis under image guidance [44].

The combination of robot capabilities and precise image-based navigation has significantly improved the overall success rate of cancer diagnosis and treatment [44, 4444, 1111, 88]. It is expected that future developments in this research area will lead to more effective and reliable solutions for cancer diagnosis and treatment.

## 2.2 Current Technologies for Needle-Based Interventions

Most of the robotic systems developed for cancer diagnosis and treatment are designed to perform percutaneous interventions. However, minimally invasive interventions may offer better targeting accuracy while being capable of performing percutaneous procedures as well. The most effective solutions for robotics-assisted needle-based interventions are presented to introduce the state of the art in cancer diagnostic and treatment using needle-base approaches.

### 2.2.1 AcuBot Robotic System

AcuBot from Johns Hopkins University is an early example of a special purpose robotic system [4545] developed for cancer diagnosis and treatment. AcuBot was initially developed for performing percutaneous procedures on the kidney but it has been also used for spine RF ablation [4646]. As is depicted in Figure 2.22.2, it consists of three main parts: a 1-DOF radiolucent needle driver known as PAKY (percutaneous access of the kidney), a 2-DOF RCM<sup>1</sup> mechanism that orients the needle around two axes, and a passive positioning arm attached to a 3 DOF X-Y-Z stage that mounts onto the scanner bed [4747]. The combination of the passive arm and the 3-DOF stage is used to position the PAKY above the patient; then the RCM mechanism is used to tilt the needle, and PAKY inserts the needle. However, for percutaneous procedures an RCM is not necessary because after passing through the skin it is not possible to reorient the needle.

<sup>1</sup>Remote Centre of Motion

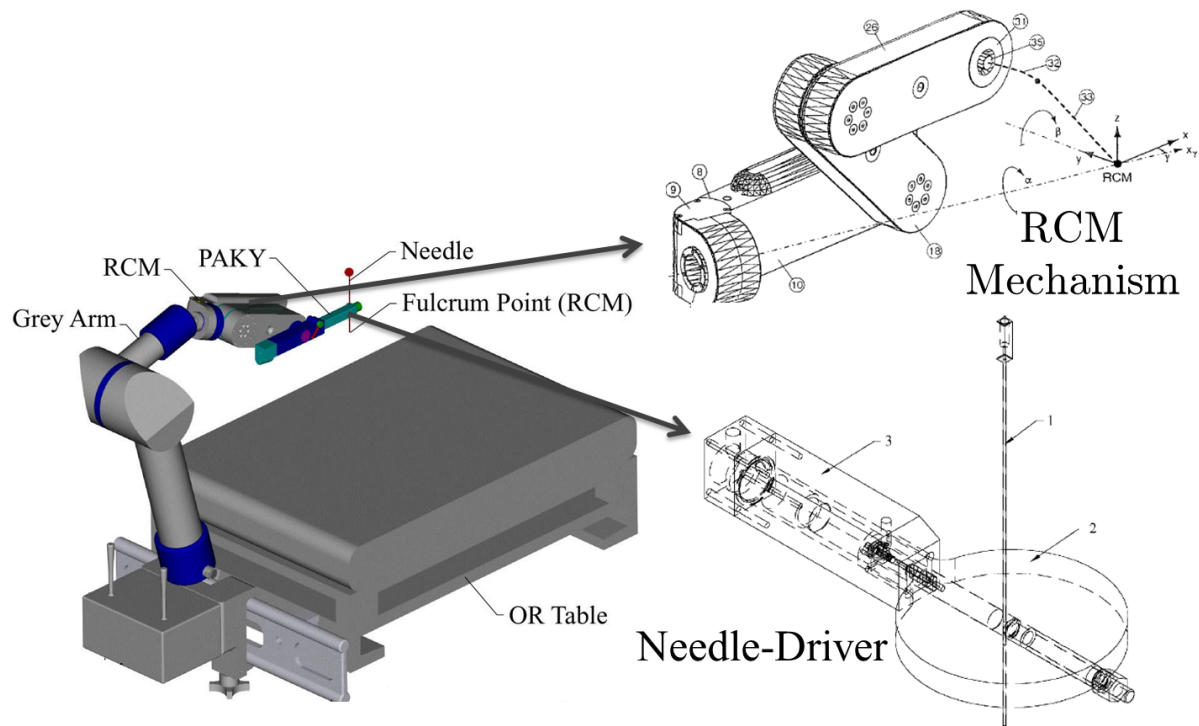


Figure 2.2: PAKY-RCM robot connected to a passive arm which can be mounted on the surgical bed [55, 66].

CT and intra-operative fluoroscopy are the two imaging modalities that Acubot uses to locate the cancerous tumours within the tissue. Since Acubot was developed in 1998, several research teams have worked on improving its performance. Implementing different robot-image registration techniques [4444, 4646, 77], improving the mechanical design and performing a variety of experiments and animal trials are some of these efforts. In a cadaver study conducted at Georgetown University, 12 metal balls of 1mm diameter were placed in a lumbar spine from L1 to L4 vertebra and targeted using the PAKY-RCM via an anterior/posterior approach and lateral fluoroscopic guidance. The average needle placement error was reported to be 1.44 mm with a standard deviation of 0.66 mm [4848].

AcuBot can be realized as one of the most advanced solutions for CT-guided needle-based interventions. It can be used for different interventions including lung cancer diagnosis [77]. Figure 2.32.3 shows the AcuBot robotic system performing experiments on a lung phantom under CT image guidance. The main drawbacks associated with this robotic system include the lack of force feedback during needle insertion and also the lack of an effective compensation of the patients movements during the intervention which are mainly caused by physiological motions such as those due to heart beat and respiration.

### 2.2.2 INNOMOTION Robotic System

INNOMOTION (Innomedic Inc., Herxheim, Germany), is another example of a robotic manipulator that is mounted on the scanner bed [88]. It was developed for percutaneous interventions under MRI guidance. Using MR compatible materials, pneumatic actuators and optical sensors

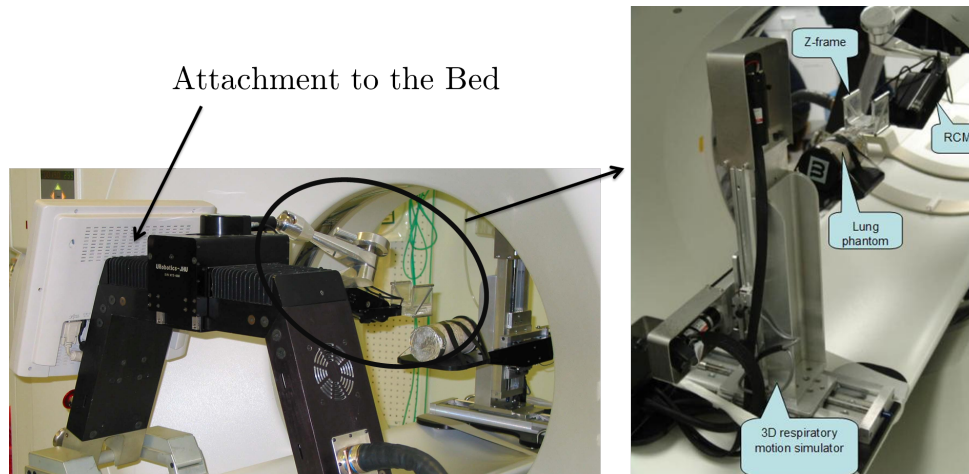


Figure 2.3: AcuBot robotic system attached during a phantom study [77].

make INNOMOTION an MRI-safe robotic manipulator. In other words, operating the robot inside the MRI scanner does not cause any hazard for the patient, robot or the scanner, and the MRI images would not be significantly degraded by the robot.

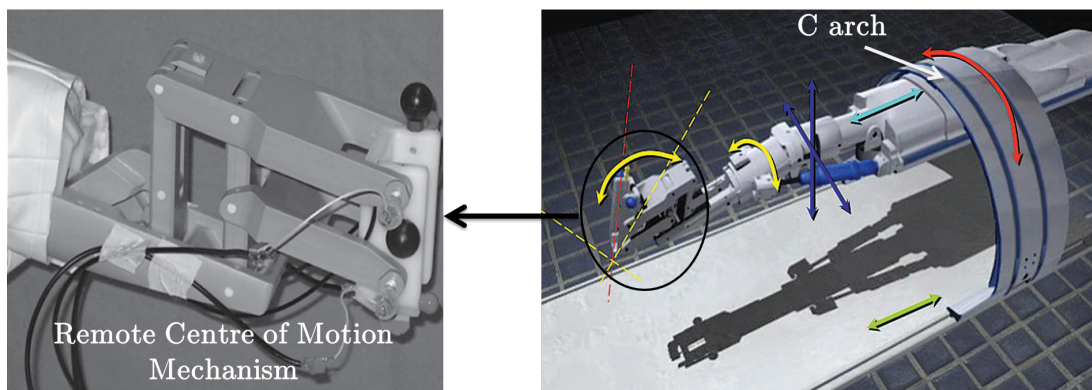


Figure 2.4: INNOMOTION robotic system [88].

As can be seen in Figure 2.42.4, there is a parallelogram mechanism to provide the required rotational degrees of freedom at a fixed point. Overall, there are 5 DOFs which are pneumatically actuated and the robotic manipulator is attached to a C-Arch to manually position the robot at the proper position depending of the type of intervention.

### 2.2.3 Robot-Assisted Minimally Invasive Lung Brachytherapy

In a research project at Canadian Surgical Technologies and Advanced Robotics (CSTAR), London, Canada, the feasibility of low dose rate brachytherapy for lung cancer treatment was studied [99]. The method consists of accessing the lung through small incisions on the thoracic cavity in order to place radioactive seeds inside cancerous lesions. The procedure is performed under ultrasound image guidance. The experimental set-up is shown in Figure 2.52.5. The set

up consists of a video-assisted thoracic surgery (VATS) box to mimic the thoracic cavity, surgical robotic arms, a seed injector, an ultrasound machine, an electromagnetic tracking system, video monitors, a computer and an endoscope. The robotic arms of the Zeus surgical system were used to hold the seed injection device and the ultrasound probe as shown in Figure 2.52.5.

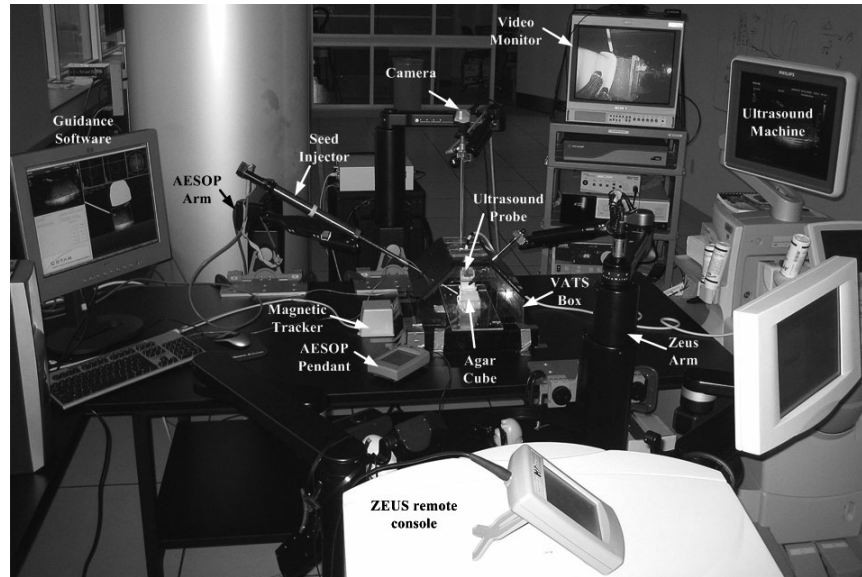


Figure 2.5: The experimental test-bed for lung brachytherapy consists of a VATS box, surgical robotic arms, a seed injector, an ultrasound machine, an electromagnetic tracking system, video monitors and an endoscope [99].

The position and orientation of the ultrasound probe and the seed injection device are determined by an electromagnetic tracking system. On the other hand, a graphical user interface provides the 2D ultrasound image and the 3D virtual representation of the ultrasound probe and the seed injection needle (Figure 2.62.6). Once the target has been identified it can be selected in the Ultrasound View. The software automatically calculates its physical position and places it in the World View as a sphere. This view already contains the Tracked Ultrasound Probe and Tracked Needle. The Interventionist can use the needle's virtual tip extension to properly orient the needle and then move the needle along the targeting trajectory. Although LDR brachytherapy is not a standard method for lung cancer treatment, the solution proposed in this work can be used for any kind of needle-based intervention. The main challenge associated with using 2D ultrasound images is the fact that it is not possible to see the whole needle inside the imaging plane all the time. In this research work, the virtual representation of the needle and the 2D ultrasound image helps the interventionist to properly orient the needle prior to targeting the cancerous lesions.

#### 2.2.4 Percutaneous Needle-Insertion Robot for Prostate Brachytherapy

Figure 2.72.7 shows a robotic manipulator developed at University of Western Ontario for percutaneous prostate brachytherapy [1010]. The real-time tracking of cancerous tumours is provided by 3D ultrasound imaging, while the robotic manipulator orients the surgical needle to

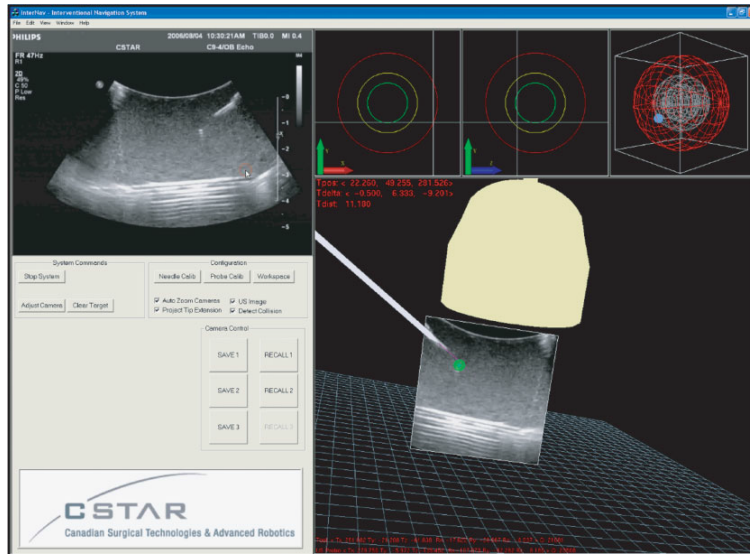


Figure 2.6: Graphical user interface for ultrasound navigation [99].

target the cancerous lesions. This robotic system has a double parallelogram RCM mechanism that provides the required rotational degrees of freedom to orient the surgical needle, rotate it about its axis of insertion to control needle bending resulting from its bevel tip, and also linear insertion of the needle into the tissue. Placing the radioactive seeds within the prostate tissue and in the proximity of targeted tumour is performed manually. Using cable-driven systems and placing more actuators near the stationary base of the robot is one of the main features of its mechanical design. Although it benefits from an RCM, for percutaneous procedures having an RCM is not necessary because after passing the skin it is not possible to reorient the needle.

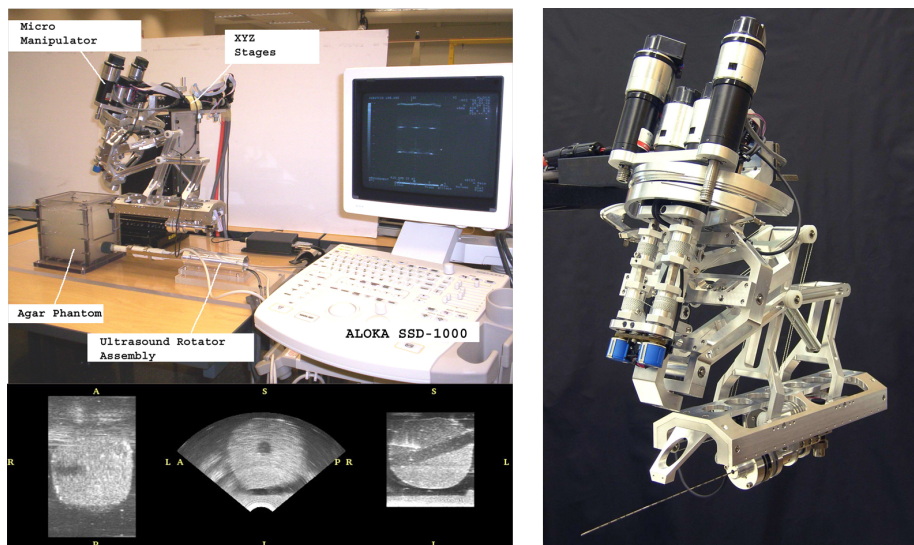


Figure 2.7: A robotic manipulator for 3D Ultrasound Guided Percutaneous Needle Insertion [1010].

### 2.2.5 Motions of the Robot Relative to the Patient

For image-guided, needle-based interventions, accurate positioning of the needle's tip plays a key role in the success of a procedure. The physiological motions of the patient's anatomy caused by heart beat and respiration along with movement of the patient inside and outside the scanner bore during the procedure can introduce errors in both image-robot registration and positioning of the robot's end-effector (i.e., the needle). Having the robot fixed to the patient's body is a simple and effective approach to compensate for such motions [4949]. In this regard, the concept of mounting a robotic manipulator on the patient's body has been proposed to passively compensate for such motions during different types of surgical interventions [5050, 1111, 2626, 1212, 5151].

### 2.2.6 Ultrasound-Guided Motion Adaptive Needle-Insertion Instrument (UMI)

UMI from the University of Tokyo, Japan [1111] is a needle insertion robotic system developed for percutaneous cholecystostomy<sup>2</sup>. It utilizes intra-operative ultrasound imaging to provide real-time monitoring of needle via ultrasound which helps to minimize the negative effects of unwanted organ motion. In addition, real-time visual servoing was designed especially for tracking the gallbladder in ultrasound images. The robot consists of a 5-DOF passive arm to position the needle at the skin entry point and a 2-DOF needle-driving part for automatic needle-insertion control. There is a spring buffer between the active control part and the 5-DOF passive arm to absorb body tremors and maintain a tolerable pressure between the ultrasound probe and the patient's skin. The ultrasound probe and the needle driver are connected to form a single unit. This structure allows the target (i.e., the tumour) and needle to be placed on the same image plane. A combination of attachments to the patient's body and visual servoing helps to minimize the errors that may be caused by the physiological motions.

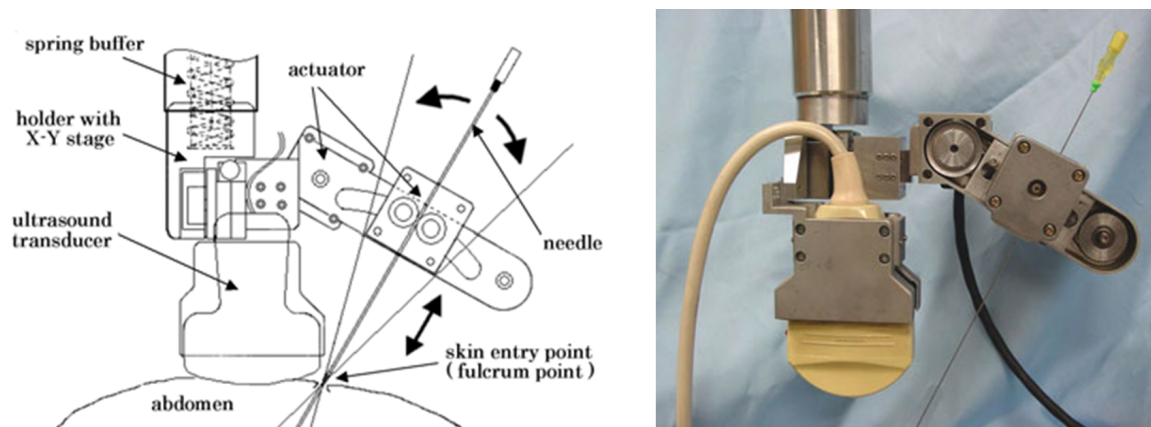


Figure 2.8: Ultrasound-guided, motion adaptive device for needle insertion [1111].

Experiments on moving phantoms were done to evaluate the performance of UMI. The

<sup>2</sup>A cholecystostomy is a procedure where a stoma is created in the gallbladder, which can facilitate placement of a tube for drainage.

final insertion error of 2.99 mm on average was obtained at the phantom moving speed of 10 mm/s. The gallbladder recognition error was also less than 1.5 mm under ordinary breathing conditions. In the animal experiment, the needle could be placed in the target with 2.0 mm error [1111]. Although this robotic system offers a solution for real-time monitoring of a specific anatomy, the poor quality of the imaging device does not make accurate targeting easy to achieve.

### 2.2.7 CT-Bot, a Robotic System for CT-Guided Percutaneous Procedures with Haptic Feedback

The CT-Bot, developed at Louis Pasteur University, France [3434] is a 7-DOF patient-mounted robotic manipulator for percutaneous procedures under CT image guidance. This robotic system was developed after PAKY and UMI robotic systems. Providing force feedback and being mounted on the patient's body are the main contributions of this robotic system. It is also claimed that the robot has an optimized structure which minimizes flexibility and vibrations.

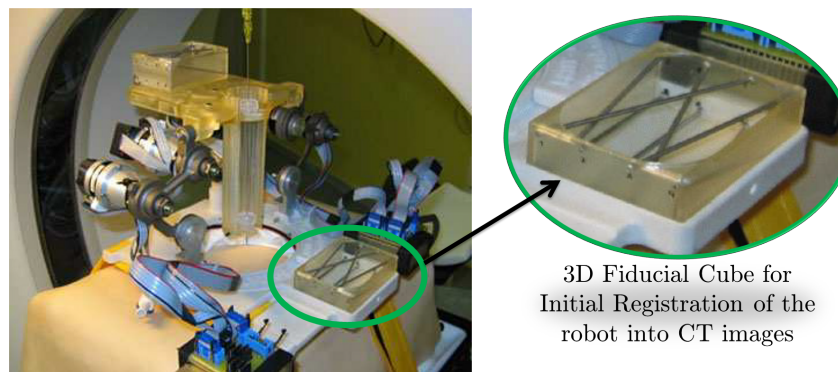


Figure 2.9: Prototype of CT-bot under test [1212, 1313].

The CT-Bot is made of two parts: a 5-DOF positioning device and a 2-DOF needle-driving tool. The positioning device weighs about 3 kg and is mounted on the patient's body using straps. The needle driver is controlled by a haptic interface (such as a commercially available haptic interface) which lets the clinician to decide on the applied force and speed for inserting the needle into the targeted tissue. A parallel mechanism is used to develop the positioning part. In general, parallel structures are used in applications requiring high rigidity and compactness in spite of heavy loads. In addition, they offer a very good absolute positioning accuracy for their end-effectors. However, the proposed parallel mechanism for the CT-Bot lacks a simple analytical kinematic solution [5252] which complicates the robot modelling and control. As can be seen in Figure 2.102.10 there are three serial chains (i.e., legs ) connecting the positioning platform to the robot's base. ‘

The latest version of the CT-Bot can apply up to 20 N force in the needle insertion direction and a mean targeting error of less than 3 mm was reported at a distance of 300 mm beneath the skin level [1212]. The CT-Bot is developed only for percutaneous procedures and it does not have an RCM mechanism.

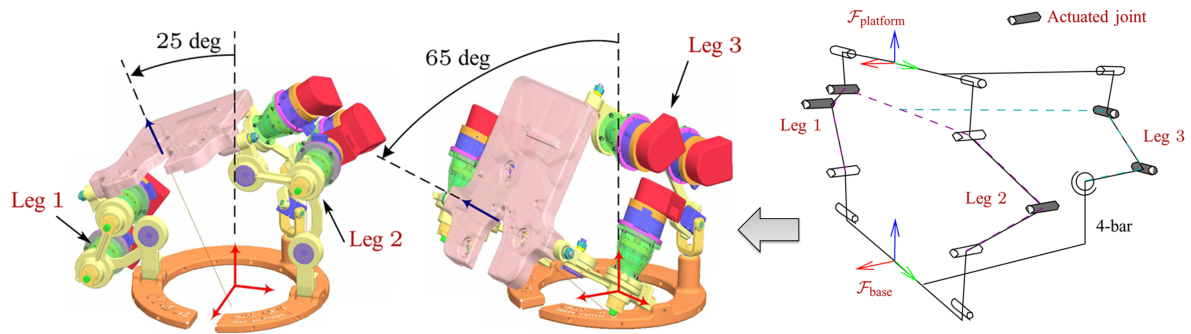


Figure 2.10: Parallel mechanism of CT-Bot robotic system[1212].

### 2.2.8 Robopsy

Robopsy from MIT is another patient-mounted robotic system developed for lung biopsy [1414]. This light-weight robot works under CT guidance and provides essential degrees of freedom for percutaneous lung biopsy. By partitioning the tasks between the interventionist and the robot, the required degrees of freedom are reduced to four which include two tilt angles for needle orientation (pitch and yaw), selective gripping of the needle, and needle insertion/retraction. Figure 2.112.11 shows Robopsy needle insertion system.

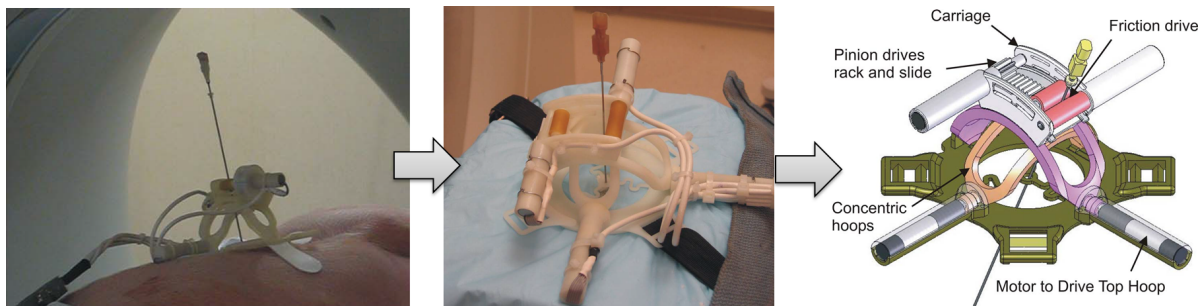


Figure 2.11: Robopsy system[1414].

As shown in Figure 2.112.11, a parallel spherical-based mechanism provides two rotational degrees of freedom to orient the needle and a friction-based mechanism is used to provide linear insertion/retraction motion of the needle. In addition, a rack and pinion linkage is used for selective gripping of the needle as shown in Figure 2.122.12.

As a patient breathes while the surgical needle is inside the lung, the part remaining outside the body is observed to move in a periodic fashion often referred to as waggle back and forth, describing approximately a 25 degree cone [1414]. This motion occurs because the lung's parenchyma, or the respiratory tissue, moves relative to the skin surface. If the robot fixes the needle during this motion it will lead to laceration of the lung tissue. Thus, once the needle has traversed the pleura, the device must be capable of only firmly gripping the needle for long enough to orient or insert it, after which it must be promptly released. The rack and pinion mechanism shown in Figure 2.122.12 provides the selective gripping of the needle during lung biopsy.

Robopsy utilizes a parallel combination of two spherical mechanisms which improves its



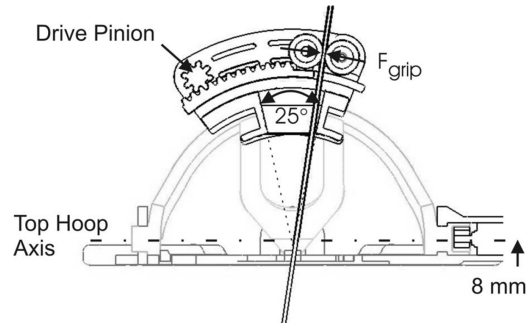


Figure 2.12: Schematic view of Robopsy mechanism [1414].

accuracy and locates more actuators near the stationary base of the robot. Although this mechanism has an RCM, there is an 8 mm offset between the provided RCM and the patient's body. During a percutaneous procedure, this offset distance does not cause any problems, but if it is used for a minimally invasive needle-based intervention, it can apply excessive force into the patient's body and also affect the targeting accuracy. The overall accuracy of this robotic system is not mentioned.

## 2.3 Conclusion

Needle insertion surgical robots have been proven to be effective for use in cancer diagnosis and treatment. Improving the targeting accuracy, fast and effective registration into medical imaging, reducing the procedure time and removing the hazard of radiation exposure by separating the clinician from the operating site are the main achievements of such robotic systems. It has been realized that for accurate needle insertion procedures, the surgical robot needs to be compact, lightweight, simple and with relatively high structural stiffness. Although most of the needle insertion robotic manipulators are developed for percutaneous interventions, a minimally invasive approach along with using a trocar can offer an effective solution to reduce needle deflection and the overall targeting error. In this regard, it is required to provide an RCM to rotate the trocar around a fixed anchor point. Patient mounted RCM mechanisms generally suffer from an improper location of the RCM [1414, 5353] due to the fact that it is not possible to shift the RCM downward to the proper position by moving the robot downward as it is mounted on the patient's body. This results in an undesired offset between the RCM and the skin of the patient.

After a comprehensive study of the available robotic systems for needle-based interventions, it was concluded that improving the mechanical design, proper location of the RCM, having a simple analytical kinematic solution, safety and comfort of the patient, and low-cost, effective delivery of needle-based interventions are the main challenges in this field of research.

# Chapter 3

## Conceptual Design

### 3.1 Introduction

In this chapter, the design requirements for effective delivery of needle-based interventions for lung cancer diagnosis and treatment are introduced. The Remote Centre of Motion (RCM) mechanisms are studied and compared. The best mechanism based on the design requirements is chosen and the required modifications to provide better performance are discussed. A novel parallel RCM mechanism is introduced and details of its performance and advantages are described.

### 3.2 Design Requirements

The design requirements are based on consideration of the requirements for the minimally invasive delivery of needle-based interventions for lung cancer diagnosis and treatment. During such interventions, the surgical needle is introduced into the patient's body using a trocar, which is the main difference from percutaneous interventions. The most common types of needle-based interventions that may involve the use of a trocar include image-guided needle biopsy, Radio Frequency (RF) ablation and microwave ablation. In addition, high dose rate brachytherapy has been shown to be effective for lung cancer treatment and it can be considered as a possible treatment option [3636]. All of these interventions were investigated and the surgical procedures were carefully studied through watching surgeries and consulting with thoracic surgeons.

#### 3.2.1 Required Degrees of Freedom and Workspace

Based on my observations, four DOFs were identified to perform a needle-based intervention with a robotic manipulator: Two rotations (i.e., pitch and yaw) about the entry port into the patient's body to target the tumour prior to inserting the needle inside the living tissue, one translational motion to insert the needle towards the target after achieving the correct targeting angles, and the rotation of the needle around its longitudinal axis (i.e., Roll), which can be used for needle steering [5454] and also to reduce static insertion displacement errors [5555]. The required range of motion was investigated through consultation with surgeons, observing

the related surgical procedures and also from the literature review [1414]. The entry port into the patient's body is determined based on the location of the tumour in medical images. Thus, a range of 30 degrees for the two targeting motions (pitch and yaw) was determined to be sufficient to access the tumours embedded within the lung. Figure 3.13.1 introduces the required DOFs.

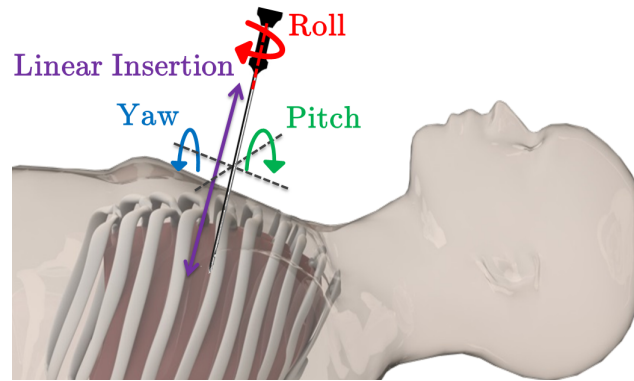


Figure 3.1: The required degrees of freedom.

### 3.2.2 Compact, Patient-Mounted Design

Fixing a surgical robot to the patient's body is a simple effective approach to reduce errors that may be caused by physiological motions such as respiration and repositioning of the patient during the surgical procedure. In this regard, the robot should be designed to be compact and light-weight so it can be easily mounted on the patient's body during the medical interventions. In some applications, the surgical robot may need to be compact enough to fit inside a typical medical imaging scanner for better integration of medical image guidance.

### 3.2.3 Remote Centre of Motion (RCM)

During a minimally invasive needle-based intervention, the surgical needle may be introduced into the patient's body through a trocar. In this way, it is possible to correct the needle's orientation (i.e., pitch and yaw) prior to insertion into the target tissue, while during a percutaneous procedure no orientation correction is possible after passing through the skin. Thus, orienting the surgical tool (i.e., surgical needle) at the entry port into the patient's body is a basic requirement for a robotic system involved in a minimally invasive intervention to prevent damage to the patient's body. This constraint can be met using Remote Centre of Motion (RCM) mechanisms that can decouple the rotational and translational motions of a surgical tool at a remote point some distance from the mechanical structure of the mechanism. It is required to design a proper RCM mechanism to rotate the surgical needle while it is introduced into the patient's body through a trocar.

### 3.2.4 Required Force/Torque

For targeting tumours embedded within a living tissue it is required to orient the surgical needle and in turn the trocar using pitch and yaw DOFs. The maximum required torques to orient the trocar are reported to be 0.7 Nm [5656]. On the other hand, an experimental setup was developed to find the interaction forces between the needle and the lung using different needle sizes and different insertion velocities. As shown in Fig. 3.23.2, a T-LSR300B motorized linear stage (Zaber Technologies) is used to insert the needle into fresh porcine lung tissue using different insertion velocities. The needle is attached to a force sensor (Nano 43, ATI Industrial Automation) using a rapid-prototyped adaptor.

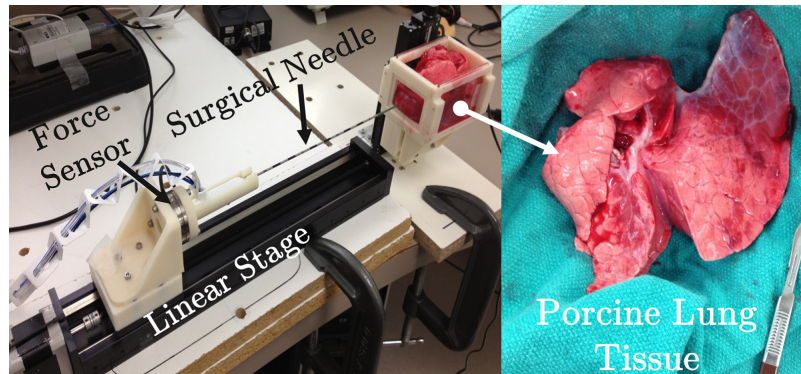


Figure 3.2: Experimental setup to measure tissue-needle interaction forces

Obviously, larger needles cause higher forces. It was also observed that the puncture force decreases when the insertion speed is increased. Fig. 3.33.3 shows the axial forces applied to a 13 GA ablation probe inserted into a fresh porcine lung tissue for different insertion velocities.

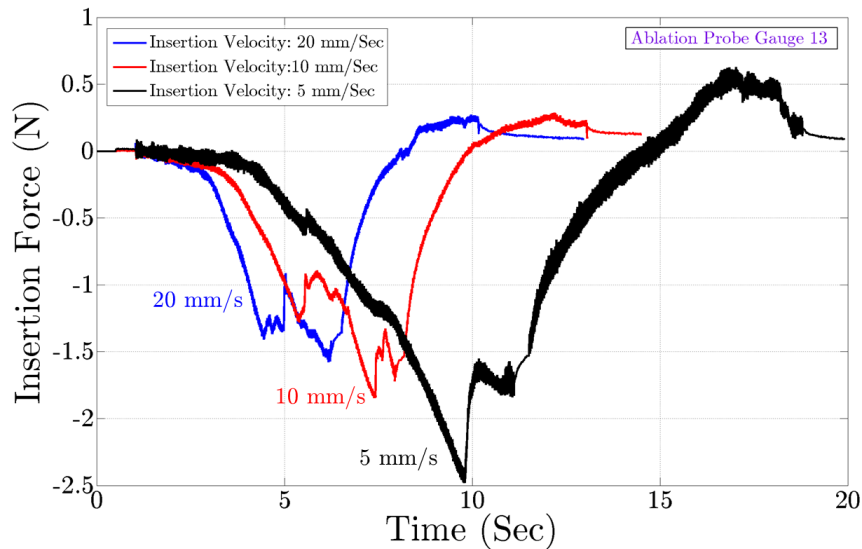


Figure 3.3: Axial forces applied to a 13 GA ablation probe inserted into porcine lung tissue.

The maximum axial interaction force applied to a 13 GA needle was 2.5 N. However, a

10 N axial force maybe considered to be the maximum external force applied to the needle to ensure that the robot is capable of performing needle-based interventions for various organs.

### 3.2.5 Modular Design to Support Different Needle Sizes

Based on our investigations and consultations with radiologists and thoracic surgeons, it was concluded that needle sizes between 25 GA to 13 GA are typically used for lung cancer diagnosis and treatment. One of the main contributions of this research is to develop a robotic system capable of supporting different types of needle-based interventions including biopsy, ablation and brachytherapy. Thus, one of the design requirements is to find a simple effective approach to support different needle sizes.

### 3.2.6 Size of Trocar

After consultation with a thoracic surgeon and considering the range of needle sizes that the robot should support, a standard trocar size of 5 mm was chosen to introduce the surgical needle into the patient's thoracic cavity. Thus, the corresponding part of the robot which enters the trocar needs to be 5 mm in diameter in order to fit inside the trocar.

Table 3.13.1 represents the main design requirements for robotics-assisted needle-based interventions. There are some other requirements such as sterilizability, a simple and low-cost construction procedure and safety that must be considered during the design process.

Table 3.1: List of design requirements

Design Considerations	Requirements
Type of Mechanism	Remote Centre of Motion
Required DOFs	pitch, yaw, roll and linear insertion
Needle Sizes	25 GA – 13 GA
Material	Light-weight, high-stiffness and sterilizable
Trocar Size	Standard troca size of 5 mm
Required Workspace	$\pm 15^\circ$ for pitch and yaw
Maximum Required Force/Torque	0.7 Nm for pitch and yaw; 10 N for insertion into the tissue

## 3.3 Existing RCM Mechanisms

In this section, the existing RCM mechanisms used in minimally invasive interventions are investigated and their advantages and disadvantages are discussed. Most of the RCM mechanisms have at least 2 rotational degrees of freedom around the entry port into the patients body, while they can be considered as a combination of several 1-DOF mechanisms. Thus, the existing 1-DOF RCM mechanisms are introduced and classified to provide a basic picture of the concept of an RCM. Multi DOFs RCM mechanisms used in different robotic systems are

analysed and the type or types of RCM mechanisms implemented in such robotic systems are introduced.

### 3.3.1 Single-Revolute-Joint RCM Mechanisms

Generally, if a link is connected to a revolute joint at its end, all the points of the link excluding the ones which are located on the axis of the revolute joint rotate around the axis of the joint [2020]. Thus, any point on this axis can be considered as an RCM. Figure 3.43.4 shows a 1 DOF single revolute joint RCM mechanism.

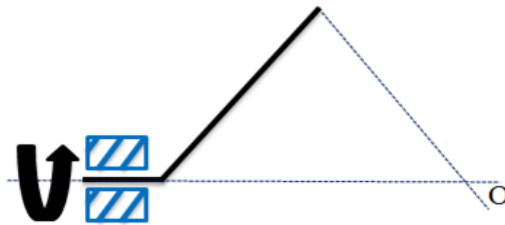


Figure 3.4: Single revolute joint RCM.

More degrees of freedom can be achieved by using a serial or parallel sequence of this 1 DOF mechanism.

#### Serial Sequence

The wrist mechanism of the industrial robot “Puma 560” is a good example of serial sequence of single revolute joints. Figure 2 shows the schematic of a Puma 560 wrist mechanism.

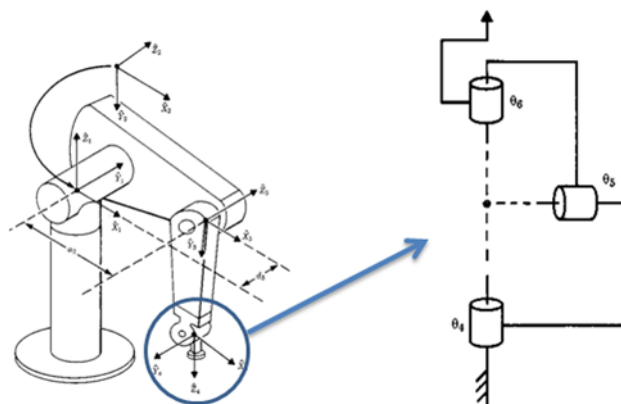


Figure 3.5: Schematic of a 3R (Revolute) wrist of Puma 560 [1515].

As can be seen in Figure 3.53.5, all three axes of rotation intersect at a single point (RCM) and all the axes are mutually orthogonal. Thus, the end-effector connected to this wrist can provide any possible orientation [1515].

**Parallel Sequence**

The Immersion laparoscopic surgery simulation device, implements a parallel sequence of single revolute RCM mechanisms to produce two rotational degrees of freedom at a fixed point. Figure 3.63.6 depicts the details of this mechanism. As can be seen, two rotational degrees of freedom can be actuated at the base of the mechanism through a gimbal which reduces the floating inertia. However, this mechanism needs precise manufacturing and the dynamic solution of the mechanism is complicated.

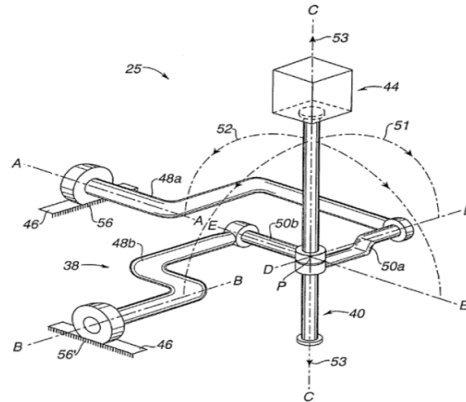


Figure 3.6: The parallel sequence of the single revolute mechanism used by Immersion [1616].

A single revolute mechanism has useful features such as a fixed remote centre of motion, simple extension to multi degrees of freedom in either a serial or parallel sequence. The parallel sequence needs high precision manufacturing and the range of motions are limited because of a collision possibility. With the actuators located at the base of the mechanism, high stiffness, low inertia and backlash are the key advantages of the parallel sequence. On the other hand, the serial sequence has the problem of high floating inertia because each joint has to support all the distal linkages connected to the end-effector so more powerful actuators are required.

**3.3.2 Circular-Prismatic-Joint RCM Mechanisms**

Since the basic idea behind an RCM mechanism is rotation at the remote centre, some mechanisms use circular prismatic joints to produce the RCM. Figure 3.73.7 presents this kind of RCM mechanism.

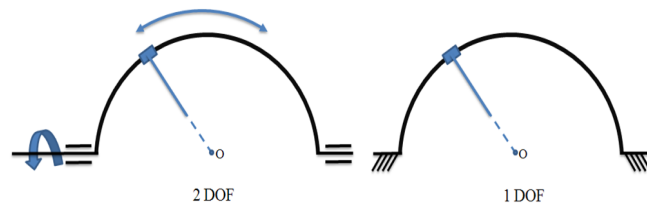


Figure 3.7: Circular prismatic joint RCM mechanism.

### Probot

Probot, developed at Imperial College London, UK [1717], implements a circular-prismatic-joint RCM mechanism to orient the surgical tool. Figure 3.83.8 represents Probot's mechanism and its application inside the OR. As shown in Figure 3.83.8, there are two rotational degrees of freedom at the RCM to orient the cutter and two translational motions, to place the robot in the proper location to insert the cutter inside the patient's body.

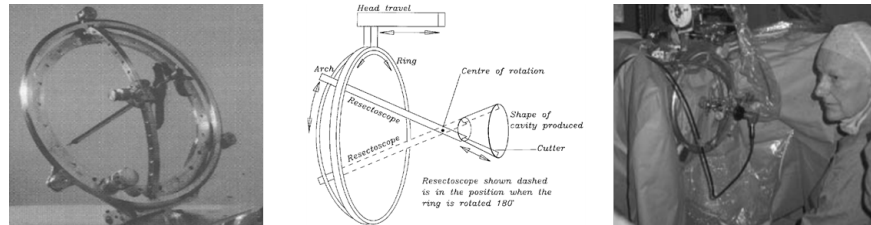


Figure 3.8: Details of Probot's RCM mechanism.[1717, 1818]

### Light Endoscope Robot (LER)

LER is a 3 DOF robotic manipulator that was initially developed as an endoscope holder, but in later versions it was modified to hold surgical tools as well [1919, 5353]. Being light-weight and cost effective is the main feature of this robotic system. As illustrated in Figure 3.93.9, the base of the mechanism attaches to the patient's body and the trocar is mounted on the mechanism as well. The RCM mechanism used in this robotic system is a combination of a circular prismatic joint and a single revolute joint which provides two rotational degrees of freedom around a remote centre of rotation. The circular prismatic joint rotates the endoscope around axis 1 and it consists of two circular rings. The inclination motion around axis 2 is produced by a single revolute joint mechanism.

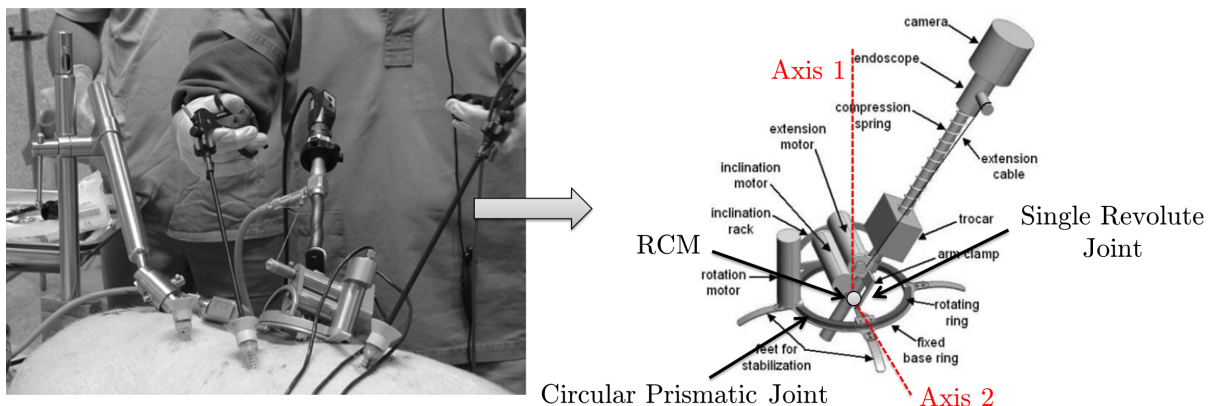


Figure 3.9: LER mechanism (obtained from [1919])

Possibility of having decoupled rotational degrees of freedom and simplicity are the main advantages of using circular revolute joints for an RCM mechanism. However, there are some weak points associated with this kind of an RCM mechanism. For instance, this mechanism



occupies a large space for a specific range of motions, precise fabrication is needed for circular guides and transferring the actuators to the base of this type of mechanism is quite challenging.

### 3.4 Parallelogram-Based RCM Mechanisms

Double parallelogram mechanism is arguably the most recognized type of an RCM mechanism in surgical robotics [5757, 5858, 2121]. Figure 3.103.10 depicts the basic configurations of a double parallelogram mechanism. In configuration (a), the BCDE loop contains some redundant motion constraints, so by eliminating the redundant constraints other configurations can be found as can be seen in Figure 3.103.10. A main feature of the double parallelogram mechanism is the fact that the centre of rotation is located at an adjustable distance from the body of the mechanism. By changing the length of specific linkages, the location of the RCM can be adjusted.

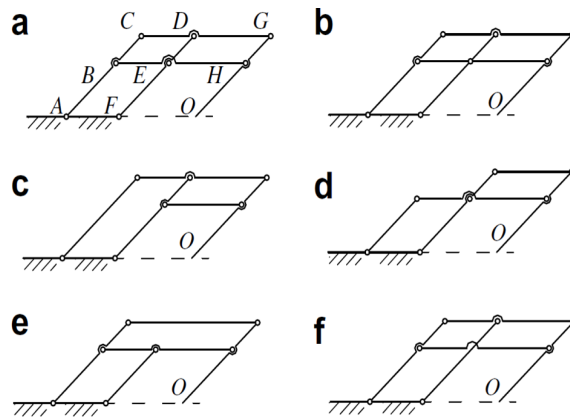


Figure 3.10: Different configurations of a double parallelogram RCM mechanism [2020]

#### Blue Dragon Robotic System

Blue Dragon, developed at the University of Washington [2121], is a good example of using a double parallelogram mechanism to provide an RCM as shown in Figure 3.113.11. The Blue Dragon was developed for acquiring the kinematics and the dynamics of two endoscopic tools along with the visual view of the surgical scene.

The double parallelogram configuration used in the Blue Dragon provides three rotational degrees of freedom at the RCM point as shown in Figure 3.113.11.

#### Neurobot

Neurobot from Imperial College, London, UK, is a special-purpose surgical robot for neurosurgery [2222]. Figure 3.123.12 illustrates the double parallelogram mechanism used in Neurobot.

The linear motion is produced at the base of the robot by adding two translational motions along the linkages of Parallelogram 1 as shown in Figure 3.123.12. This reduces the floating

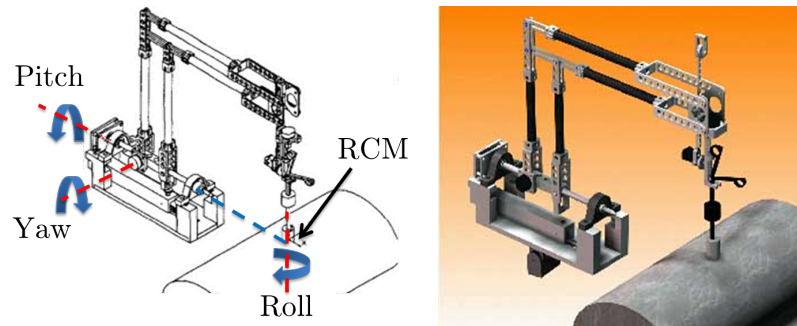


Figure 3.11: parallelgram-based RCM mechanism of Blue Dragon robotic system [2121]

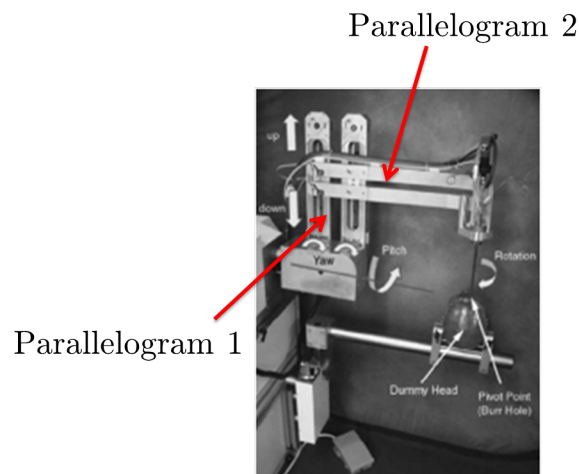


Figure 3.12: Neurobot [2222]

inertia; however, these two sliding motions near the base of robot must be controlled separately and synchronously to produce the linear motion of the surgical tool which complicates the control of the mechanism.

### Tool-Offset Problem in Double Parallelogram Mechanism

Figure 3.133.13 presents the basic configuration of a double parallelogram mechanism. As can be seen in Figure 3.133.13, the point “O” is the RCM and the axis “I” connects the two last joints of the mechanism. In this regard, the surgical tool must be mounted along axis I to rotate at the RCM. In other words, there is no offset between the last joints of mechanism and the surgical tool’s axis. This limitation makes it difficult to mount the surgical tool and the required actuators at the end of a double parallelogram mechanism.

This problem can be solved by using curved linkages that provide some space to mount the surgical tool at the end of the parallelogram mechanism [2424]. As shown in Figure 3.143.14, the link BDF is curved at joint D by the angle  $\phi$  that provides an offset distance,  $L_3$ , between the link EG and the surgical tool’s axis. There is a geometrical relation between the offset distance and the curve angle which arises from the geometry of the double parallelogram mechanism. According to this geometrical relationship,  $L_3 = L_4 \cdot \sin(\phi)$ .

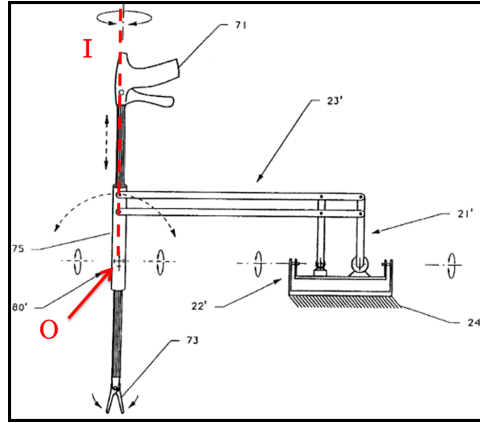


Figure 3.13: Basic configuration of a double parallelogram mechanism (obtained from [2323])

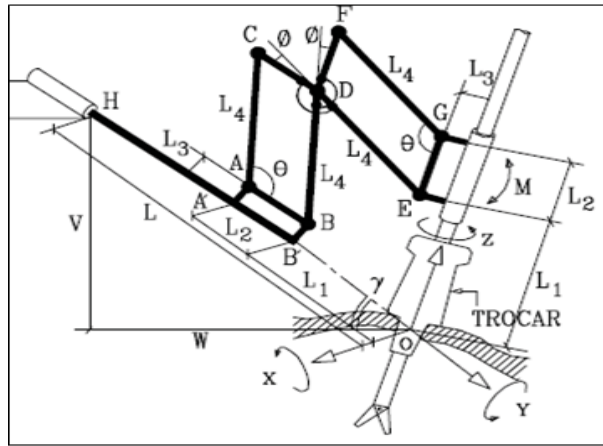


Figure 3.14: Modified double-parallelgram mechanism [2424]

### The daVinci Robotic Arms (Device Holders)

The daVinci surgical system has several robotic manipulators to hold the surgical tools. This robotic system implements a double parallelogram RCM mechanism to orient the surgical tool at a fixed point [5757]. As is shown in Figure 3.15, the double parallelogram configuration used for holding the surgical tool uses curved links to provide an offset distance for mounting the surgical tool.

A parallelogram-based mechanism is the most common type of RCM mechanism and it has been modified for different types of applications. A fixed RCM, a wide range of motion, high manipulability and a simple analytical solution for the kinematics are the key features of a double parallelogram-based RCM. On the other hand, collision and possible singularities are the weak points of this type of mechanism which should be considered in design.

#### 3.4.1 A Spherical RCM Mechanism

A spherical RCM mechanism is a spatial mechanism in which all the joint axes intersect at a fixed point which is the centre of a sphere. Therefore, the links can be placed on the surface

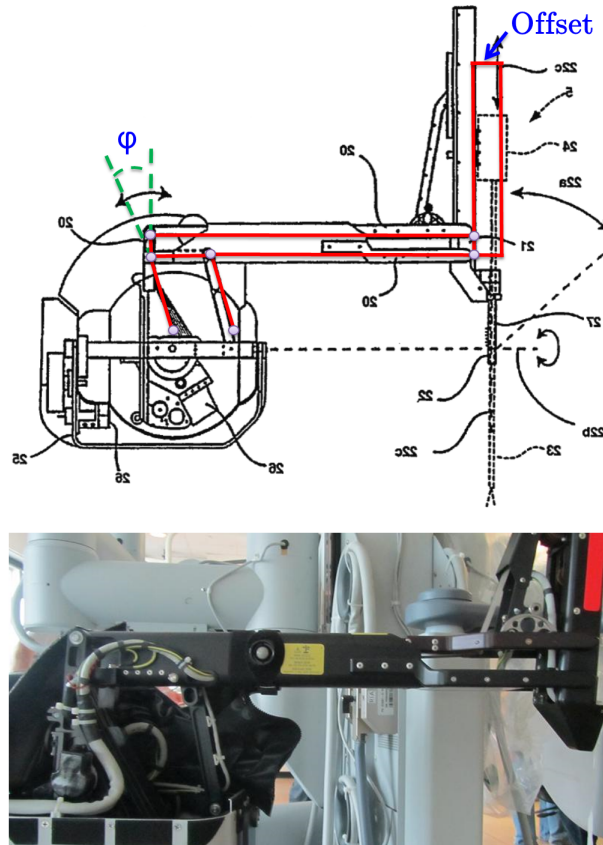


Figure 3.15: The parallelogram mechanism used in daVinci robotic arms

of this virtual sphere. Figure 25 shows how a spherical mechanism works. This kind of mechanism can be also regarded as a serial sequence of a single-revolute-joint RCM mechanism which was described above.

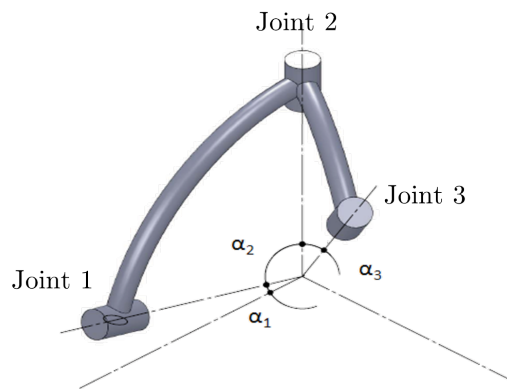


Figure 3.16: Spherical RCM mechanism.

### The Raven Surgical Robotic System

The Raven system, developed at the University of Washington, USA, is another surgical robotic system for minimally invasive surgery. Development of this surgical manipulator was based on the design analysis of two simple spherical manipulators in serial and parallel combinations [5959]. As shown in Figure 3.173.17, the serial and the parallel mechanisms are both connected to a circular prismatic joint to provide the required relational DOFs. It was shown both experimentally and analytically that the serial mechanism is better suited since the parallel mechanism has weak points such as a limited workspace with kinematic singularities inside the workspace, self-collision, robot–robot collision and robot–patient collision possibilities [2525].

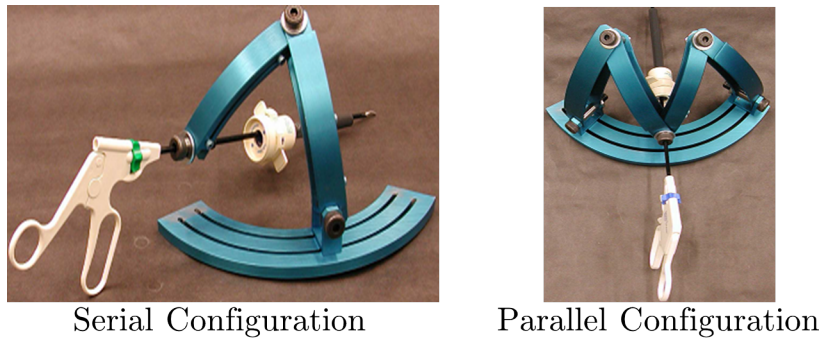


Figure 3.17: Serial and parallel configurations of a Spherical RCM mechanism [?]

The Raven surgical manipulator is totally cable driven and all the actuators are transferred to the static base which reduces the floating inertia, but as shown in Figure 3.183.18, this manipulator occupies lots of space. The part of the manipulator which produces linear motion is almost 80 cm long which takes lots of space above the patient's body. The Raven surgical system was developed for research purposes and not for clinical use.

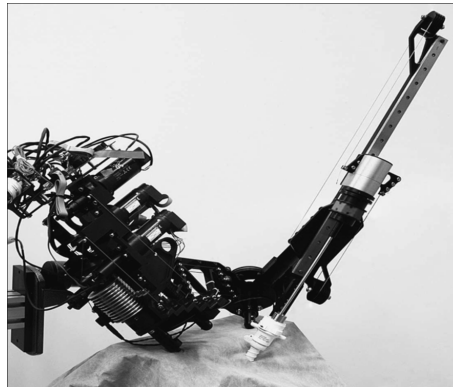


Figure 3.18: The Raven surgical manipulator [2525].

### MC2E Robotic Arm

MC2E (French acronym for compact manipulator for endoscopic surgery) is a light-weight robotic arm (about 1.3 Kg) that is used for minimally invasive surgery [2626]. As shown in

Figure 3.193.19, there is a serial combination of spherical linkages which provides an RCM at the entry port. The lower part of the arm is a compact 2-DOF spherical mechanism which is mounted on the patient's body and then clipped to the trocar. Thus, the robotic arm moves not only the surgical tool but also the trocar.

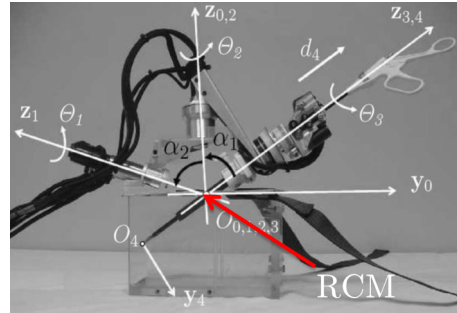


Figure 3.19: The RCM mechanism of MC2E [2626].

The main advantage of this robotic arm is the ease of installation, because once the robot is attached to the trocar, the RCM is correctly aligned at the entry point. However, being totally supported by the patient's body is the main problem associated with this robotic arm.

As shown in Figure 3.163.16, the kinematic performance of the spherical linkage mechanism can be manipulated by changing the angles between the joints (i.e.,  $\alpha_1, \alpha_2, \alpha_3$ ). This means that the kinematics of such a mechanism can be optimized to gain better workspace and kinematic performance. A simple forward kinematic solution along with having two responses for the inverse kinematics is another advantage of this type of RCM mechanism which may be helpful in avoiding collisions. On the other hand, there are some weaknesses associated with the spherical RCM mechanism. First, the rotational degrees of freedom (pitch, yaw and roll) are not decoupled. Furthermore, just one of the actuators (pitch motion) is located at the base of robot while the others are floating. Finally, low rigidity and backlash accumulation which are the main features of any serial mechanism are the other drawbacks that should be considered.

### 3.4.2 Instantaneous RCM mechanism

Although instantaneous RCM mechanisms do not exactly comply with the definition of RCM mechanisms, in some applications they can be helpful. In this type of mechanism, the RCM is created in certain linkage configuration, so it is not flexible and permanent.

The four-link mechanism shown in Figure 3.203.20 is an example of an instantaneous RCM mechanism. The four-link mechanism forms an isosceles trapezoid, and point  $O$  is an instantaneous RCM since link  $AB$  has a pure rotation around this point.

### A Compact MR compatible Surgical Manipulator

Figure 3.213.21 shows an MRI<sup>1</sup> compatible robot which implements an instantaneous RCM mechanism [2727].

<sup>1</sup>Magnetic Resonance Imaging

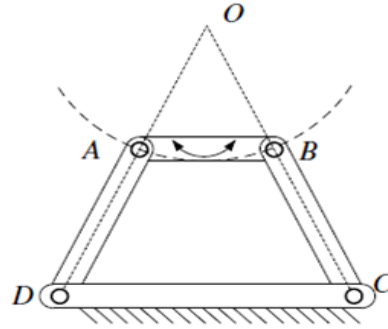


Figure 3.20: An example of instantaneous RCM mechanisms [2020].

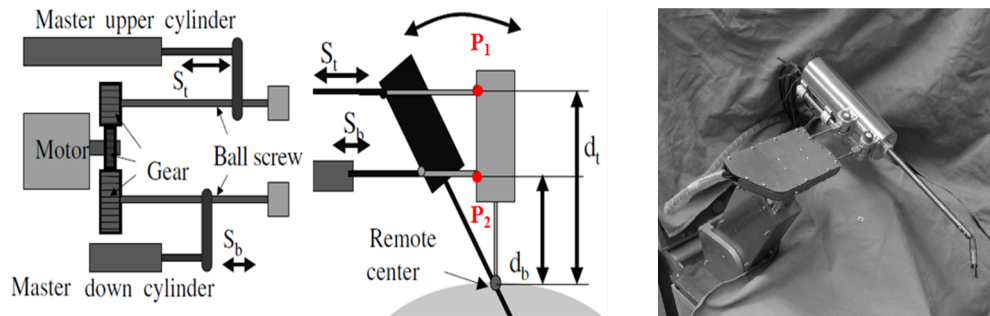


Figure 3.21: MR compatible robot with an instantaneous RCM mechanism [2727].

As shown in Figure 3.213.21, there are two prismatic joints connected to the surgical tool at points  $P_1$  and  $P_2$ . In order to enforce the rotation of the surgical tool at the RCM, i.e.,  $\frac{S_b}{S_t} = \frac{d_b}{d_t}$  [2727].

The main problem of an instantaneous mechanism is the fact that the rotational and translational motions of the surgical tool are not decoupled; so whenever the interventionist wants to rotate the surgical tool, there will also be an unwanted translational motion of the tool inside/outside the patient's body. However, for certain applications, this type of mechanism may be of some value.

### 3.4.3 A Passive Joint RCM Mechanism

The main reason for using an RCM mechanism in minimally invasive interventions is to avoid applying excessive forces to the patient's body. In this regard, the AESOP (Automated Endoscopic System for Optimal Positioning) robotic arm uses a different approach to provide an RCM. As shown in Figure 3.223.22, AESOP has seven degrees of freedom. There are four active joints including the linear axis (1) and three rotational degrees of freedom ( $\theta_2, \theta_3, \theta_7$ ) and two passive joints including  $\theta_5$  and  $\theta_6$  [2828]. These two passive joints are not motor driven and have no brakes. They are used to ensure that no forces are exerted at the entry point.

In addition, the robot has another revolute joint ( $\theta_4$ ) that can be used to suit the geometry to the actual situation. A passive joint RCM mechanism can guarantee that no forces are exerted on the patient's body even if the patient moves during the surgical intervention. However, there are two degrees of freedom that are not actuated; so the position of the surgical tool is more

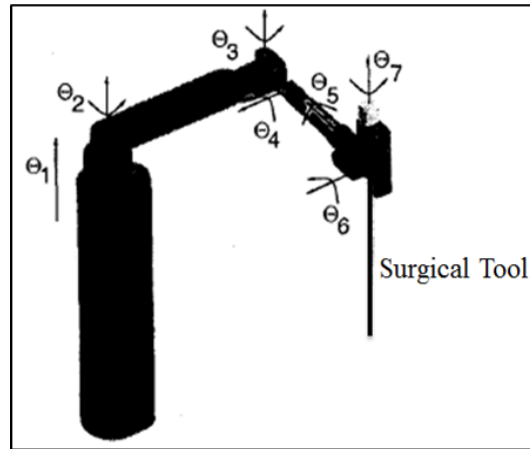


Figure 3.22: AESOP robotic arm [2828].

complicated. In this regard, the location of the entry point should be determined by solving iterative mathematical equations [2828] to solve the forward kinematics. Thus, position or force control for this type of RCM mechanism is challenging.

#### 3.4.4 Software-Based RCM

Some surgical robots do not have an RCM mechanism; instead they control two degrees of freedom in a way to produce a virtual RCM. This approach is called software-based RCM, because there is no mechanical constraint to create an RCM. There are two main approaches to create a software-based RCM. One way is Cartesian position or impedance control about a virtual point of entry, which is assumed to be stationary or detected by some sensors. The second approach is to control two joints of the robot to output zero torque at the entry point [3030].

In this regard, industrial robots with sufficient degrees of freedom such as Mitsubishi PA10-7C can be used as a robotic arm in minimally invasive configuration (Figure 3.233.23).

#### DLR MiroSurge Robotic System

The MiroSurge system, developed at the Institute of Robotics and Mechatronics, German Aerospace Centre is a versatile robotic system for general surgical applications including minimally invasive interventions [3030]. The MiroSurge robot is a light-weight robotic arm (around 10 kg) which can hold the surgical tool like a human hand. To achieve this, a serial mechanism with seven degrees of freedom, which resembles those of the human arm, has been developed and optimized for medical procedures [3030]. As shown in Figure 3.243.24 there is a shoulder (roll-pitch-yaw), an upper arm, an elbow (pitch-roll), a forearm and a wrist (pitch-roll). Each group of joints have intersecting axes which makes the inverse kinematics of the robot solvable. For minimally invasive interventions, two revolute joints are controlled either by Cartesian position or impedance control about a virtual point of entry or by a torque control system to ensure that no forces are exerted at the entry port on the patient's body.

Although a software-based approach can provide a virtual RCM without any mechanical



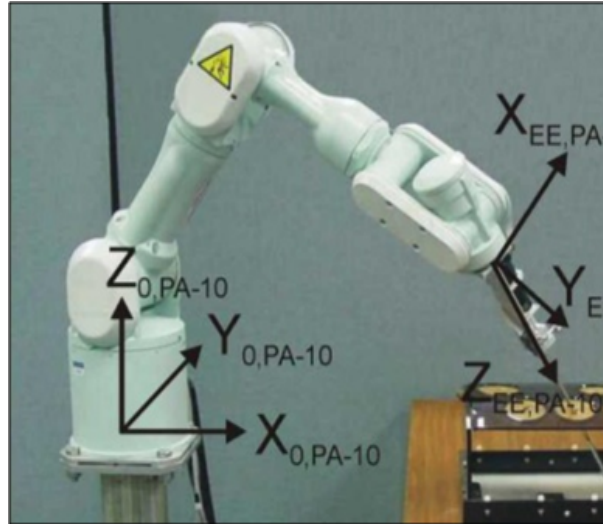


Figure 3.23: A Mitsubishi, PA10-7C robot used in minimally invasive surgery configuration [2929].

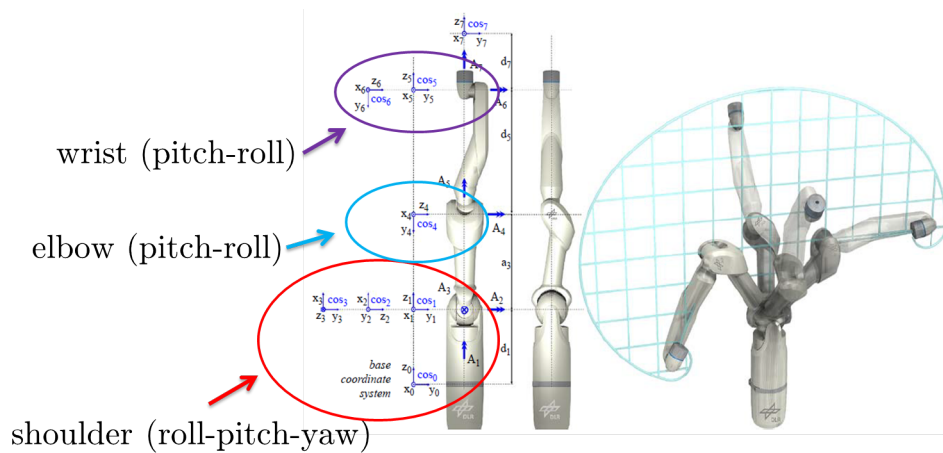


Figure 3.24: The DLR MiroSurge robotic arm (obtained from [3030]).

constraint, there are some basic drawbacks associated with this approach. At least two actuated degrees of freedom are required to provide an RCM. Furthermore, the low reliability of such an approach that is totally dependent on software is another limitation to be considered. Thus, for a general-purpose robotic arm which is not specialized for minimally invasive interventions but has sufficient DOFs, software-based RCM mechanism is a plausible approach.

### 3.4.5 Conclusions Regarding Existing RCM Mechanisms

A comprehensive investigation on different types of RCM mechanisms used in existing robotic systems was done. It was realized that there are several techniques for producing an RCM. The main challenge is to choose a proper mechanism considering the design requirements and then try to modify it and improve its performance. There are several contributing factors

that researchers have focused on to improve the performance of existing RCM mechanisms including using an appropriate actuation method, reducing the linkages and floating inertia, optimizing a mechanism for a specific purpose, and increasing the structural stiffness. It can be concluded that there is not an ideal RCM mechanism that is suitable for all applications. The choice of an RCM mechanism should be based on the type of intervention, applied forces, required workspace and the surgical environment. Effective approaches can then be found to improve the performance of the chosen RCM.

## 3.5 Choosing a proper RCM Mechanism

### 3.5.1 Comparing and Ranking the RCM Mechanism

In order to evaluate different types of RCM mechanisms, the design requirements are classified and weighted with regard to their level of importance. In this context, the design requirements are divided into three main groups: functionality, construction, and safety with assignment of importance specified as 60%, 30%, and 10% respectively. Within the category of functionality, producing a fixed RCM is assigned 40% (equalling 24% of the total), sufficient workspace 25% (equalling 15% of the total), extension to more DOFs accounts 15% (equalling 9% of the total), and precision 20% (equalling 12% of the total). In the construction category, being compact and lightweight is assigned 50% (equalling 20% of the total), and having simple and low cost machining is assigned 50% (equalling 20% of the total). Finally, safety is assigned 10% of the total weighting.

Type of RCM Mechanism	Having a Fixed RCM	Sufficient Workspace	Extension to More DOFs	Positioning Accuracy	Compact and lightweight	Simple, low-cost construction	Safety	Total score
Single revolute joint	5	3	3	3	3	4	4	408
Circular-prismatic-joint	5	3	2	3	2	2	4	339
Parallelogram Based	5	5	4	4	4	4	4	479
Spherical Linkage	5	4	3	3	4	3	4	423
Instantaneous	1	1	1	2	3	3	1	202
Passive	1	4	3	3	3	4	5	337
Software based	3	4	4	3	3	2	2	324
Scores: 1 stands for weak and 5 for strong.								

Table 3.2: Comparing available RCM mechanisms.

As shown in Table 3.5.13.5.1, the double parallelogram mechanism gets the highest scores among the various RCM mechanisms. Good kinematics performance and directional uniformity, multi-rotational DOFs around a fixed RCM and low-cost of construction are some of the main advantages of this type of mechanism. The double parallelogram mechanism and its modifications have been widely used in minimally invasive surgical applications [6060]. However, it cannot be claimed that this type of RCM mechanism is an ideal choice for all of the applications. Based on the design requirements for minimally invasive delivery of needle-based interventions, it was concluded that double parallelogram based RCM mechanism is the most suitable.

## 3.6 Conclusion

After a comprehensive study of the available RCM mechanisms and their strengths and weaknesses, it was concluded that a double parallelogram-based RCM mechanism is the best fit for effective delivery of needle-based interventions for cancer diagnosis and treatment. It was also realized that there are certain techniques available to produce an RCM. Thus, it is not required to start from scratch and invent a new mechanism; instead the main challenge is to choose a basic mechanism which satisfies the design requirements and then try to improve its performance. In this regard, a double parallelogram-based mechanism was the inspiration to develop an original RCM mechanism with a compact parallel configuration for precise and effective delivery of needle-based interventions.

# Chapter 4

## Detailed Design

### 4.1 Introduction

In this chapter, the process of designing a patient-mounted robotic manipulator for minimally invasive lung cancer diagnosis and treatment is described in detail. The design requirements introduced in Chapter 33 were considered to design a proper robotic system. The proposed design benefits from a novel parallel RCM mechanism which provides the required DOFs to orient and position a surgical needle within a spherical coordinate system. The parallel configuration improves the structural stiffness of the mechanism while providing the required torques and forces to perform needle-based interventions. The proposed design is light-weight, compact and patient-mounted without compromising the structural stiffness of the mechanism. The proper location of the RCM is the main advantage of the proposed robot over existing patient-mounted robotic systems. Finally, a comprehensive Finite Element Analysis (FEA) has been done to evaluate the structural performance of the proposed design.

### 4.2 Robot Design

The proposed robot and its novel parallel RCM mechanism is shown in Figure 4.14.1. The robot weighs about 1.6 kg and its overall size is 30×30×25 cm. As can be seen in the CAD model of the robotic system, a passive holder mechanism supports the weight of the robot while it is attached to the patient's body.

#### 4.2.1 Parallel RCM Mechanism

Double parallelogram mechanisms have been widely used in medical robotics to provide an RCM at the entry port into the patient's body [5858, 2121, 5757, 6161]. A fixed RCM, a wide range of motion, high manipulability and a simple analytical solution for the kinematics are the main features of a double parallelogram-based RCM. However, having a large number of linkages is the main drawback associated with this design. As is shown in Figure 4.14.1, the proposed parallel RCM mechanism has two main kinematic chains (i.e., legs) that connect the body of the mechanism to the stationary base of the mechanism. The main leg of the mechanism provides the RCM in a way similar to the double parallelogram mechanism while having

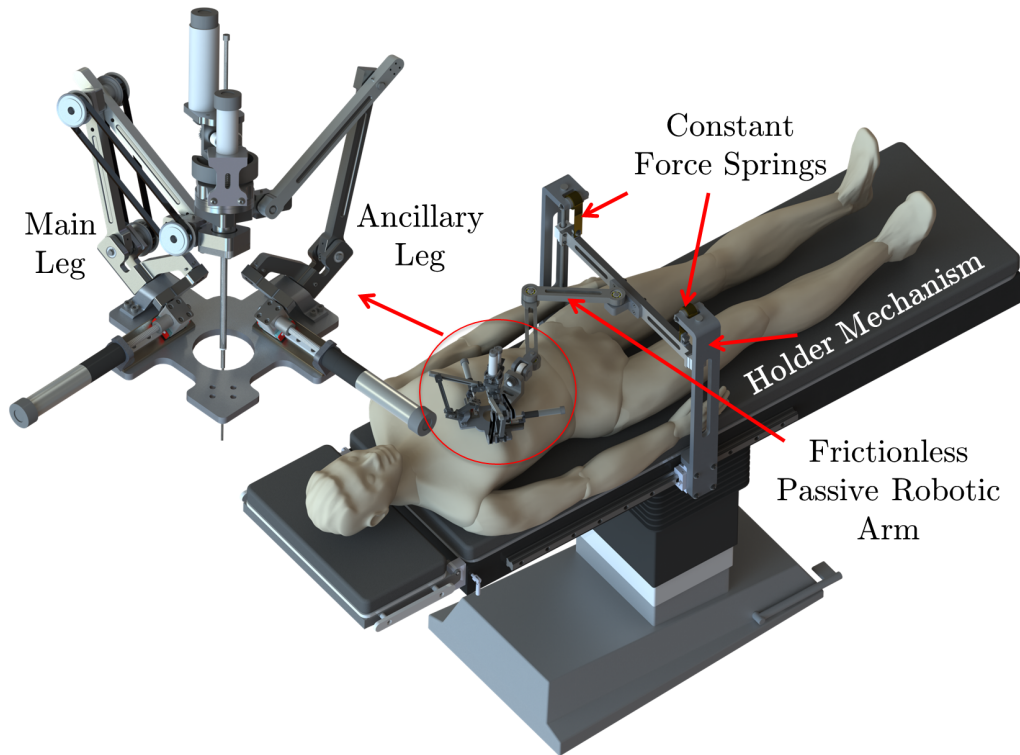


Figure 4.1: The proposed patient-mounted robot with a novel parallel RCM mechanism.

a fewer number of rigid linkages. As a result the design becomes more compact and light-weight. As depicted in Figure 4.24.2, the main leg has four linkages shown as coloured bars and two motion constraints. The motion constraints (i.e., timing belts and pulleys) transfer rotation from Link 1 to Link 3 and from Link 2 to Link 4 to provide the RCM. Thus, link 1 is always parallel with Link 3 and link 4 rotates around a fixed point (i.e., the RCM). The ancillary leg is connected to the main leg as depicted in Figure 4.24.2 and forms the parallel configuration. The two legs have a rotational degree of freedom relative to each other; otherwise, the mechanism would be locked. This rotational degree of freedom is related to the geometry of the mechanism and plays a key role in finding the kinematic solution for the parallel configuration. The ancillary leg has the same number of links but it does not require any motion constraints, as it moves in combination with the main leg.

#### 4.2.2 Proper location of RCM

RCM mechanisms that are developed to be patient-mounted suffer from the problem of the RCM not being properly located. [1919, 1414] due to the fact that it is not possible to shift the RCM downward to an appropriate position by moving the entire robot downwards. This results in an offset, shifting the RCM away from the skin of the patient. However, the ideal position of the RCM is in the middle of the wall of the cavity through which the surgery is performed to minimize the damage. For surgical interventions in the abdominal cavity, this imperfection can be neglected since all of the forces resulting from tool rotation around the RCM are applied to the fat and muscles. In the thoracic cavity, the ideal position of the RCM is between two

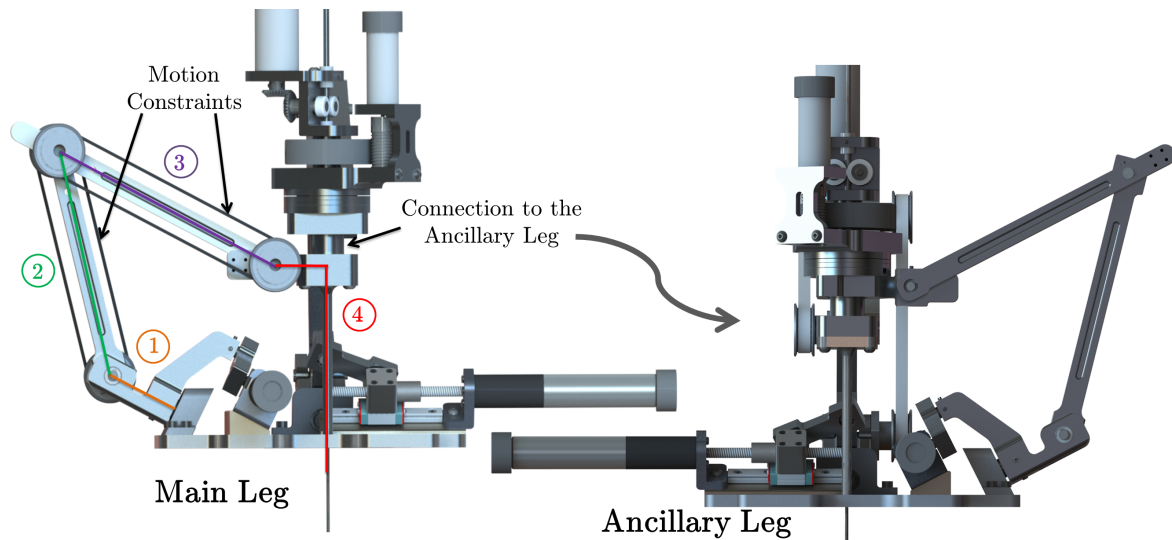


Figure 4.2: The main leg of the parallel mechanism and its connection to the ancillary leg.

adjacent ribs. If there is an offset between the location of the RCM and the ribs, the available workspace for orienting the surgical needle while it is inside the thoracic cavity would be limited by the ribs and the application of excessive forces to the ribs may result in a lot of pain for the patient after surgery. The proposed design is capable of moving the RCM downward up to a certain limit to maintain the compactness of the design. It was realized that placing the RCM on the skin is insufficient and it must be moved downward to gain more workspace without applying excessive force to the ribs. The RCM was moved 2 cm below skin level with the proposed compact design to maintain the required workspace while minimizing the applied forces to the adjoining ribs during the procedure. Considering the fact that the entry point is near the tumor location within the lung, this location is suitable for a wide range of patients. This issue was checked with a thoracic surgeon to ensure that the RCM is located in a proper position. Moving the RCM downward was achieved by inclining each of the mechanism's legs downward as is shown in Figure 4.34.3 and placing the base of each leg at the appropriate position. There is a geometric relationship between the incline angle, the relative position of each leg and the length of Link 2 which will be discussed below in more detail. To move the RCM downward, it is required to increase the length of Link 2 while increasing the incline angle. The proposed mechanism is intended to be mounted on the patient's body and it needs to be compact. Thus, the amount that the RCM can be moved downward is limited.

### 4.2.3 Main Leg of the Robot

As was explained previously, the main leg of the robot provides the RCM. The main leg is a special kind of RCM mechanism designed for this project and can be considered as a double parallelogram-based mechanism. In a general double parallelogram mechanism (shown in Figure 4.44.4), at least 6 linkages are required to provide the RCM. However, two of these linkages can be replaced by motion constraints to transfer rotation from one link to another. As a result, the mechanism becomes more compact and light-weight. In addition, using a proper motion transfer system can provide the same stiffness as the extra linkages.

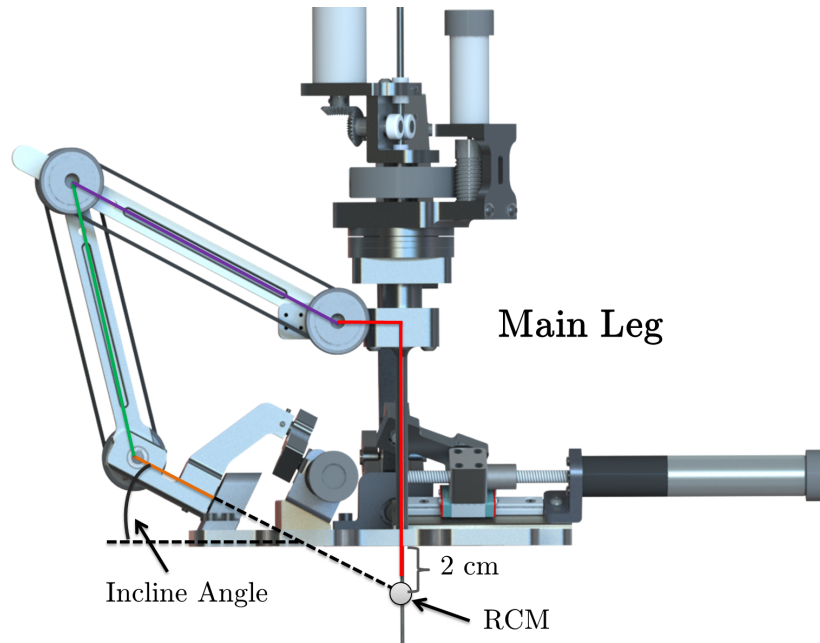


Figure 4.3: Inclining each leg of the robot to move the RCM downward.

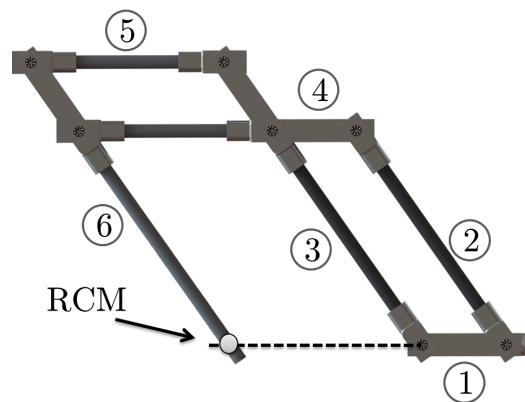


Figure 4.4: General configuration of a double parallelogram mechanism.

Figure 4.54.5 shows the right leg of the robot when it is not inclined to move the RCM downward. The main leg is a serial kinematic chain consisting of 4 linkages (shown as coloured bars) and two motion constraints (i.e., timing belts and pulleys). This RCM mechanism acts like the modified double parallelogram mechanism which was discussed in Chapter 33. In such a double parallelogram mechanism, there is an offset distance between the last joint of the mechanism and the axis of the surgical tool which facilitates attachment of the surgical tools to the end of the mechanism.

As can be seen in Figure 4.54.5, there is a geometric relation between the length of Link 2 ( $L_1$ ) and the offset distance between the last joint and the axis of the surgical tool. The offset distance is  $L_1 \sin(\phi)$ .

Although the main leg is an independent serial RCM mechanism, adding the ancillary leg is required to get a parallel configuration. Placing more actuators at the stationary base of the

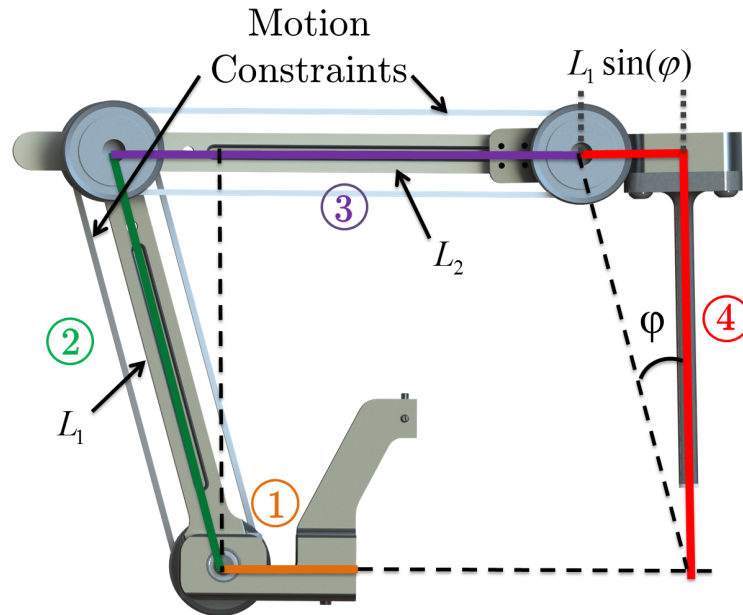


Figure 4.5: The main leg of the proposed parallel RCM mechanism.

robot and more structural stiffness are the main advantages of having a parallel configuration. The proposed parallel configuration is originally a hybrid mechanism since it is composed of two serial mechanisms (i.e., legs).

#### 4.2.4 Degrees of Freedom

The proposed robot provides four DOFs to move the surgical needle within a spherical coordinate system. Figure 4.6.4 introduces these DOFs and shows the details of the actuation methods.

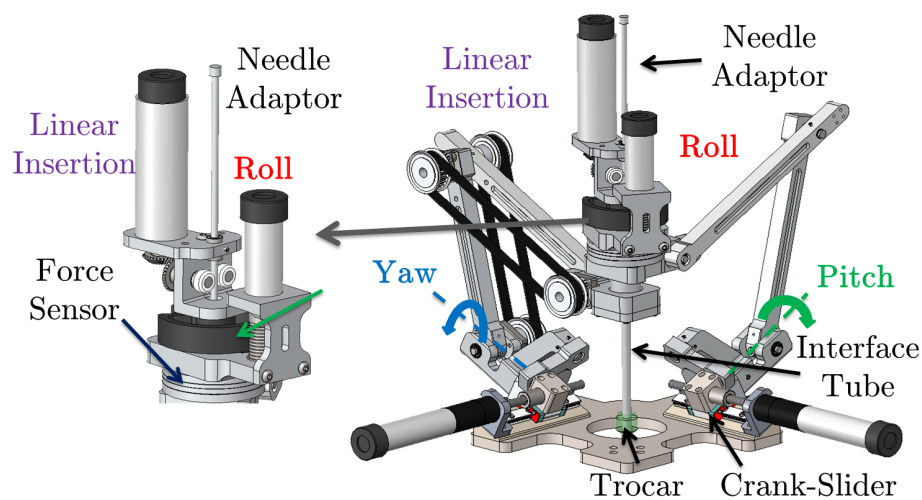


Figure 4.6: Details of the mechanism and its degrees of freedom.

Pitch and yaw are the two DOFs used to tilt the needle around the RCM to target the



tumours based on medical image guidance. These two DOFs are actuated using crank–slider mechanisms which will be discussed in more detail. As can be seen in Figure 4.64.6, the pitch and yaw DOFs rotate the interface tube to perform the targeting tasks while roll and linear insertion are actuated independently using two actuators located at the top of the mechanism.

### 4.2.5 Direct Force Measurement

As can be seen in Figure 4.64.6, there is a force sensor integrated inside the mechanism to measure the interaction forces between the surgical needle and tissue. The pitch and yaw DOFs orient the interface tube which is inside the trocar to target the cancerous lesions. The needle-adaptor contains the needle and is actuated by the roll and Linear insertion motors to move through a hollow force sensor (Nano 43 6-DOF force/torque sensor, ATI Industrial Automation), the body of the mechanism, the interface tube and the trocar. The force sensor is attached to the mechanism’s legs on one side while the other side supports the roll and linear insertion actuation system. As a result, the needle has no interaction with the trocar and directly interacts with the tissue. Figure 4.74.7 shows the cannula through which the surgical needle passes.

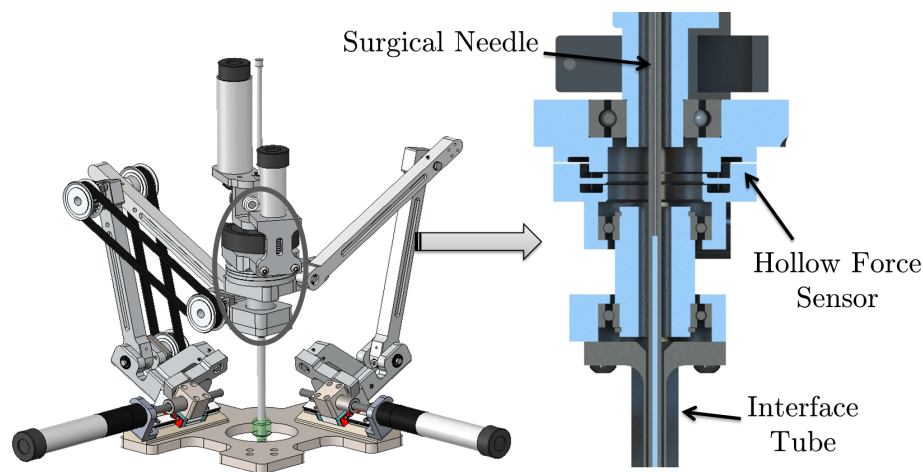


Figure 4.7: Surgical needle goes through a cannula to avoid interaction with the trocar.

The position of the force sensor along with the design of the mechanism makes it possible to measure the pure interaction forces between the needle and lung tissue. The force measurement can be used to minimize the needle deflection and to confirm the location of tumours by reflecting the appropriate forces to the surgeon’s hand through the use of a haptic interface.

### 4.2.6 Crank–Slider Mechanism to Actuate the Pitch And Yaw DOFs

The parallel configuration of the robot’s mechanism makes it possible to actuate both the pitch and yaw motions at the stationary base of the robot which reduces the floating inertia. It is required to provide sufficient torque to orient a trocar while it is inserted inside a body cavity. In addition, the proposed robot is intended to be compact so it can be mounted on the patient’s body while he/she is positioned inside a medical imaging scanner. In addition,

each leg of the robot is inclined to move the RCM downward which makes it more difficult to accommodate the required actuators. In this regard, a crank–slider mechanism was designed to provide a compact actuation mechanism capable of providing sufficient torques to rotate the trocar around the RCM while having appropriate motion resolution. Figure 4.84.8 shows the crank-slider mechanism in detail.

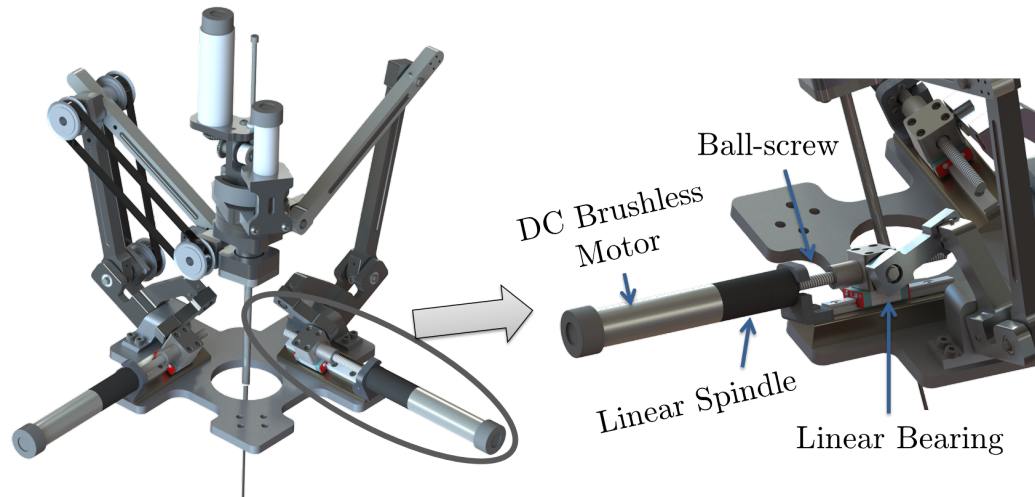


Figure 4.8: The crank–slider mechanism used to actuate the pitch and yaw DOFs.

The crank–slider mechanism is driven by a linear actuators (i.e., spindle and ball-screw). The combination of the crank–slider and ball screw provides a considerable mechanical advantage to provide the torque required to tilt the trocar while minimizing the amount of angular backlash in the pitch and yaw DOFs. A combination of a small-size brushless DC motor (EC 16, Maxon Motor) and a linear spindle drive and ball-screw (GP 16, Maxon Motor) were chosen to actuate the crank-slider mechanism. The nominal torque (maximum continuous torque) of the brushless motor is  $17.5 \text{ mNm}$  and the crank-slider mechanism is capable of producing  $1.4 \text{ Nm}$  to orient the trocar using the pitch or yaw motions, while the brushless motor is in its nominal operating condition. Thus, the overall mechanical advantage of the crank–slider mechanism is around 80. On the other hand, the overall mechanical positioning accuracy of the linear spindle is reported to be  $0.039 \text{ mm}$  which causes less than  $0.08^\circ$  backlash in the pitch and yaw degrees of freedom. The effect of this backlash on the positioning accuracy of the robot’s end-effector (i.e., tip of the needle) was shown to be quite negligible (see Chapter 66 for more details). The crank–slider mechanism was designed to provide a compact and proper actuation system for the pitch and yaw DOFs which are used for targeting the tumours.

### 4.2.7 Linear Insertion

After successful targeting of tumours using the pitch and yaw DOFs, linear insertion of the surgical needle is required to move the needle towards the target. The linear insertion of the needle is decoupled from the pitch and yaw DOFs and targeting and insertion of the needle can be performed in completely separated steps. The insertion motion is actuated at the top of the mechanism structure using a small-size brushless DC motor (EC 22, Maxon Motor) and a friction-based actuation method. Figure 4.94.9 shows the details of insertion motion actuation.

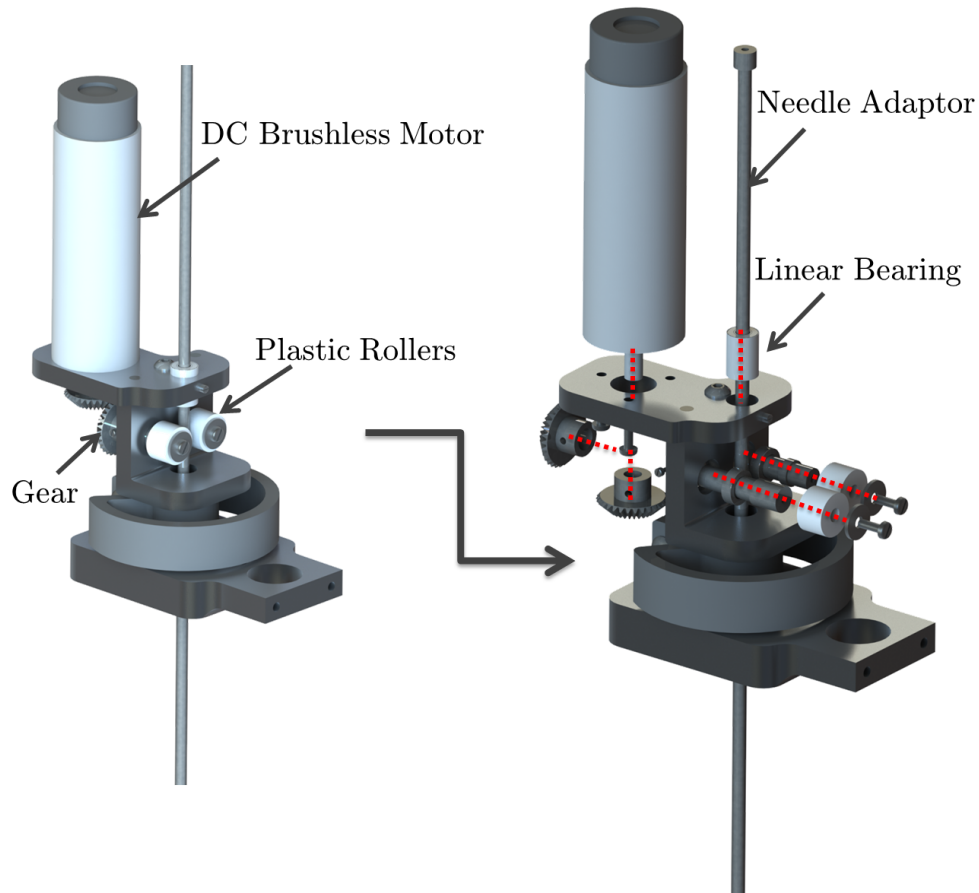


Figure 4.9: Details of linear insertion actuation.

As can be seen in Figure 4.94.9, small gears transfer rotational motion of the DC motor to the plastic rollers. There is also a linear bearing integrated into the mechanism to ensure that the needle is co-centred with the interface tube (see Figure 4.74.7). There are many options available for actuation of linear insertion including: rack and pinion, ball-screw, linear motors, etc. However, for a surgical application, it is required to choose a compact actuation method with high positioning accuracy. Thus, friction-based actuation using plastic rollers was chosen to provide a compact zero backlash translational motion for the surgical needle.

The plastic rollers was designed to produce enough normal force against the needle adaptor to ensure that sufficient friction is provided in order to avoid slipping of the needle adaptor during linear insertion. As can be seen in Figure 4.104.10, the insertion force to drive the surgical needle is produced by the roller torque.

$$\begin{aligned}\tau_{\text{Roller}} &= F_{\text{Insertion}} \times r_{\text{roller}} \\ F_{\text{Gripping}} &= F_{\text{Insertion}} / \mu_{\text{Roller}}\end{aligned}$$

(4.1)

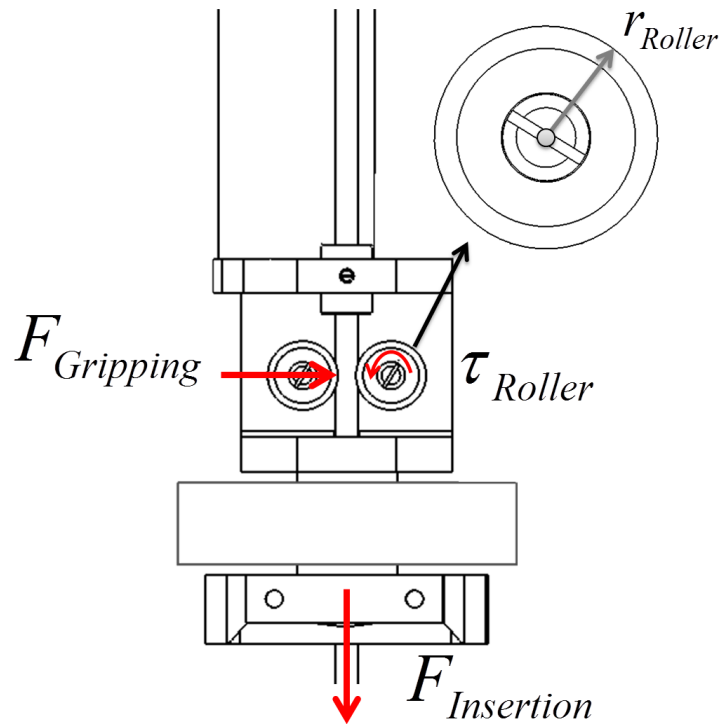


Figure 4.10: Linear insertion actuation force.

### 4.2.8 Modular Design to Support Different Needle Sizes

Based on our investigations and consultations with radiologists and thoracic surgeons, it was concluded that needle sizes between 25 GA to 13 GA are typically used for lung cancer biopsy and treatment. A simple approach was chosen to handle different needle sizes. A simple circular needle adaptor (shown in Figure 4.114.11) was designed for each needle size. It has a fixed outside diameter and a hole in the middle sized for the corresponding needle. Thus, each needle size has its own simple adaptor, and all of the adaptors have the same outside diameter. The adaptors are squeezed between two plastic rollers to provide friction-based linear motion. As is shown in Figure 4.114.11, the rollers are fixed in position to apply sufficient gripping force to the adaptor to avoid slippage during linear insertion. One of the rollers is actuated using the linear insertion motor to produce the linear motion of the needle through the trocar.

### 4.2.9 Roll Motion

The roll motion rotates the surgical needle around its longitudinal axis and is decoupled from the pitch, yaw and insertion DOFs. Considering the application of the roll motion which was described in Chapter 33, a limited range of motion (less than  $180^\circ$ ) is required for this degree of freedom. The roll motion is actuated by a small-size DC brushless motor (EC-max 16, Maxon Motor) and a cable-driven mechanism to obtain zero-backlash motion transfer from the motor axis into the roll axis. Figure 4.124.12 shows the details of roll motion actuation.

As can be seen in Figure 4.124.12, the entire actuation system related to the insertion motion is rotated around the longitudinal axis of the needle using a cable-driven mechanism. The

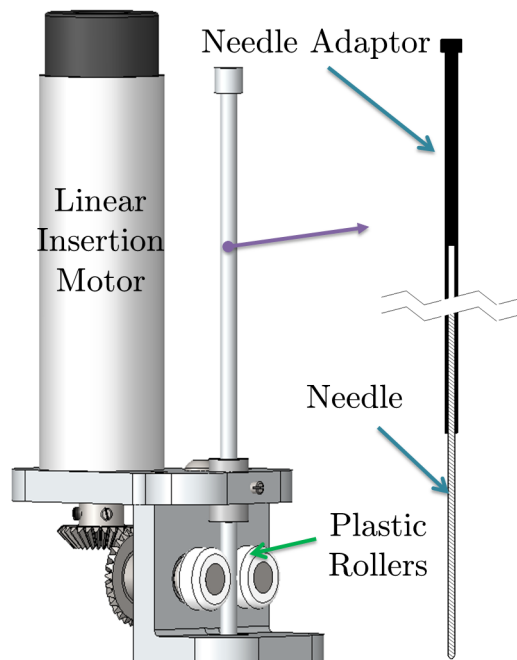


Figure 4.11: Needle adaptor and linear insertion actuation.

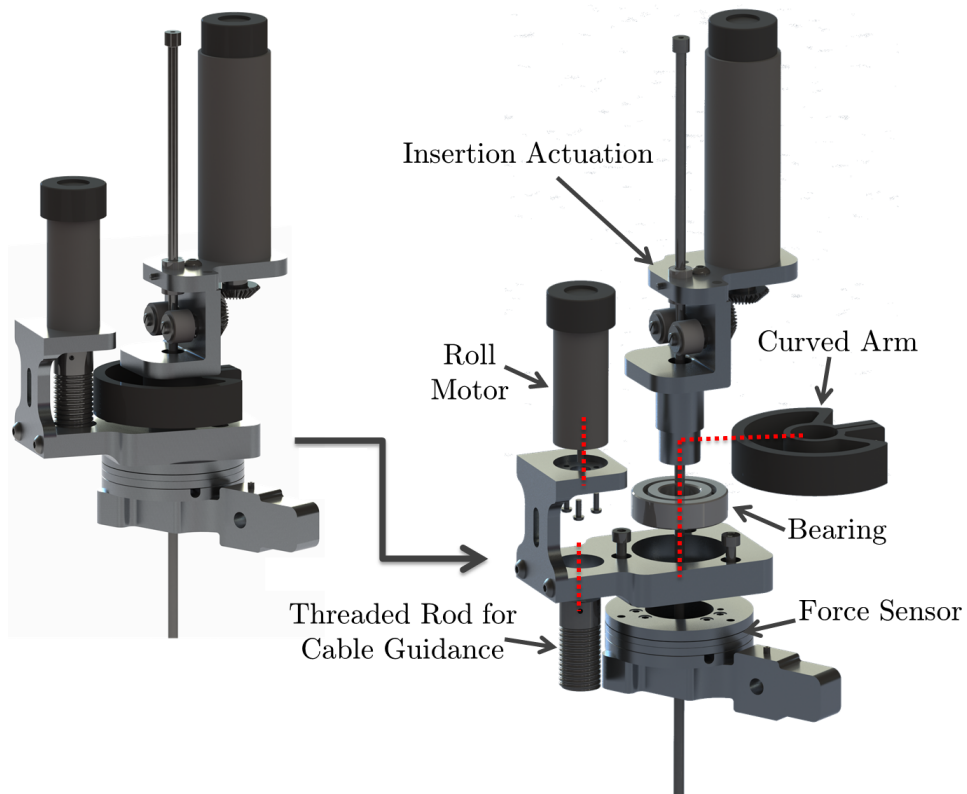


Figure 4.12: Details of roll motion actuation.

cable is wrapped around a threaded rod and then is anchored at the two sides of the curved arm. The threaded rod is used to provide appropriate guidance for the cable during the roll motion actuation.

### 4.3 Finite Element Analysis (FEA)

Material selection was done based on a number of requirements including: sufficient mechanical strength, being light-weight, radiolucency<sup>1</sup>, low cost machining and sterilizability. In this regard, aluminum was selected as a proper material for almost all of the components. However, stainless steel was chosen for some of the parts including all of the small shafts and the interface tube to provide sufficient mechanical strength. Finite element analysis was done using Abaqus (Dassault Systems) to determine the maximum amount of stress and deflection caused by the external loading applied to the robot's structure.

#### 4.3.1 FEA of Critical linkages

One approach is to run the FEA just for the critical components in the robot's mechanism to find the maximum stress and deflection. For that purpose, it is required to find the loads applied on the critical links which are caused by the external loads applied to the needle and also the interface tube. In this regard, a simulation model of the robot was used to find the loads applied to the critical links (see Chapter 66 for details of simulation model). Figure 4.134.13 shows the external loads and the critical parts. The maximum applied torques at the trocar and also the maximum insertion force applied on the needle are determined as was described in chapter 33. The critical parts are the two longest linkages of the mechanism which are more susceptible to being deflected by the applied loads.

The external loads were applied to the simulation model of the robot and the end-effector was moved within the required workspace while the applied loads on the critical linkages were recorded. The maximum values of the applied loads within the workspace were obtained and used for finite element analysis of the critical links. The material of the linkages is Aluminum Alloy 6061 with Young's modulus  $69\text{ GPa}$ , Poisson's ratio 0.33 and tensile strength of  $240\text{ MPa}$ . Figures 4.144.14 and 4.154.15 show the results of the FEA for the critical linkages which are related to the ancillary leg of the robot. In addition, Table 4.14.1 shows the maximum values for stress and deflection for the critical linkages.

Table 4.1: Finite element analysis of the critical linkages

Critical Linkages	Maximum Von Mises Stress (MPa)	Maximum Deflection (mm)
Number 1	28	0.2
Number 2	30	0.3

The designed robot benefits from a parallel configuration which improves the structural strength of the whole robot and reduces the deflection caused by external loads. In this regard,

<sup>1</sup>Permitting the passage of radiant energy, such as x-rays, with little attenuation

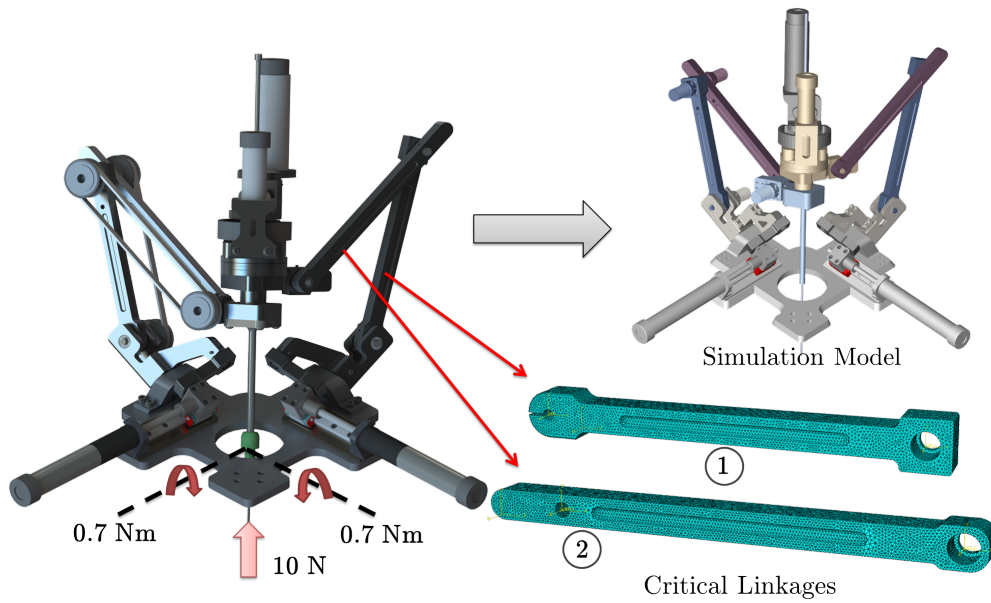


Figure 4.13: Finite element analysis.

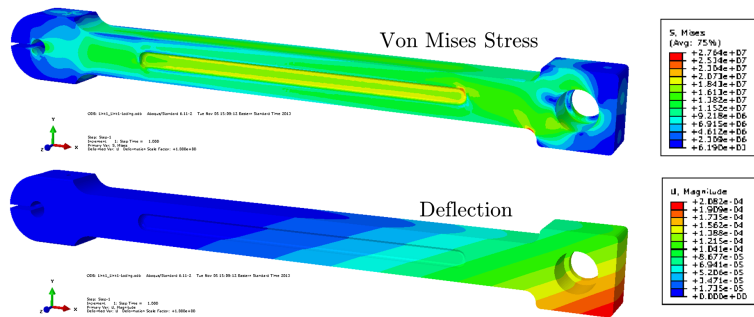


Figure 4.14: Finite element analysis of critical link number 1.

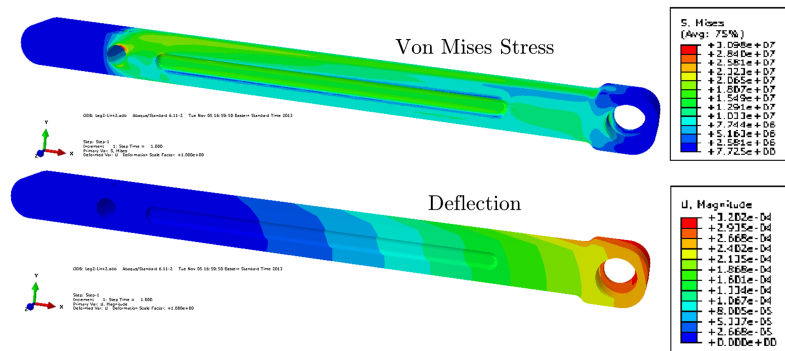


Figure 4.15: Finite element analysis of critical link number 2.

FEA analysis of the entire parallel mechanism may be required to see the overall effect of external loading on the robot's structure.

## 4.4 Actuation

Considering the application of the proposed robotic manipulator, choosing a proper actuator for each degree of freedom is of a significant importance. Fine motion resolution, being compact and light-weight while providing the required power to orient and position the surgical needle are some of the main requirements of a suitable actuator for such surgical application. The actuators were chosen based on a kinematic analysis (see Chapter 55) and results of simulation (see Chapter 66). small-size DC Brushless motors (Maxon Motor, Inc.) were chosen for actuation of the robot. Table 4.44.4 shows the details for the actuators for each degree of freedom. The Maxon servomotors benefit from a powerful controller unit capable of controlling motion, velocity and output torque of the motors. The torque control is provided by controlling the current of the motor's windings. The current and velocity modes are controlled using PI<sup>2</sup> controllers while the positioning mode is controlled by a PID<sup>3</sup> controller.

Degree of Freedom	Motor	Spindle	Encoder
Pitch	EC 16 $\Phi$ 16 mm, brushless, 60 Watt, with Hall sensors	Spindle Drive GP 16 S $\Phi$ 16 mm, Ball Screw, $\Phi \times 2$	Encoder MR, Type ML, 512 CPT*, 3 Channels, with Line Driver
Yaw	EC 16 $\Phi$ 16 mm, brushless, 60 Watt, with Hall sensors	Spindle Drive GP 16 S $\Phi$ 16 mm, Ball Screw, $\Phi \times 2$	Encoder MR, Type ML, 512 CPT, 3 Channels, with Line Driver
Roll	EC-max 16 $\Phi$ 16 mm, brushless, 8 Watt, with Hall sensors	...	Encoder MR, Type ML, 512 CPT, 3 Channels, with Line Driver
Linear Insertion	EC 22 $\Phi$ 22 mm, brushless, 100 Watt, with Hall sensors	...	Encoder MR, Type ML, 512 CPT, 3 Channels, with Line Driver
* CPT: Count Per Turn.			

Table 4.2: Details of actuation for each degree of freedom.

## 4.5 Conclusion

The mechanical design of the robot was described in detail and the actuation system related to each DOF was explained. A finite element analysis of critical linkages of the robot was performed to ensure that sufficient mechanical strength is provided. The actuators were chosen based kinematic analysis and results of simulation. Next two chapters discuss kinematic analysis and simulation of the robot.

<sup>2</sup>Proportional-Integral

<sup>3</sup>Proportional-Integral-Derivative



# Chapter 5

## Kinematic Analysis

Finding an analytical solution for parallel mechanisms is often difficult due to the intrinsic complexity of such mechanisms. An analytical solution facilitates control of the robot and improves its overall accuracy.

### 5.1 Forward Kinematics

As mentioned previously, the proposed design benefits from a parallel configuration. There are two kinematic chains (i.e., legs) that connect the robot's end-effector to its base. In order to find the forward kinematics of the robot, only one of the legs is considered to derive the forward kinematics equation. Figure 5.15.1 shows the joint variables and the coordinate systems attached to the right leg of the robot. The coordinate systems are chosen based on the Denavit-Hartenberg convention for affixing frames to links, as presented in [1515].

Using the coordinate frames and joint variables introduced in Figure 5.15.1, the Denavit-Hartenberg parameters are as shown in Table 5.15.1. The parameters  $\theta_1$ ,  $\theta_2$ ,  $\theta_3$  and  $d$  represent the pitch, yaw, roll and linear insertion motions respectively.  $L_1$  and  $L_2$  are the lengths of the linkages and  $P$  is the distance between the centres of the base coordinate frame (Frame 0), which is located at the RCM, and Frame 1. As can be seen in the first row of Table 5.15.1, each leg of the robot is inclined by  $\alpha$  ( $-27^\circ$ ) to move the RCM downward. The angle  $\phi$  provides an offset distance of  $L_1 \sin(\phi)$  between the centres of Frame 5 (last joint of the leg) and Frame 6 (surgical tool axis). See [2424] for a detailed explanation of angle  $\phi$  and the offset it provides.

Using the Denavit-Hartenberg parameters and the general transformation matrix, shown in Equation 5.15.1, the transformation matrix between any two consecutive frames can be found as presented in Equations 5.25.2 to 5.85.8.

$${}^i T_{i-1} = \begin{bmatrix} \cos(\theta_i) & -\sin(\theta_i) & 0 & a_{i-1} \\ \sin(\theta_i) \cos(\alpha_{i-1}) & \cos(\theta_i) \cos(\alpha_{i-1}) & -\sin(\alpha_{i-1}) & -\sin(\alpha_{i-1})d_i \\ \sin(\theta_i) \sin(\alpha_{i-1}) & \cos(\theta_i) \sin(\alpha_{i-1}) & -\cos(\alpha_{i-1}) & -\cos(\alpha_{i-1})d_i \\ 0 & 0 & 0 & 1 \end{bmatrix} \quad (5.1)$$

$${}^0 T_1 = \begin{bmatrix} \cos(\alpha) & 0 & \sin(\alpha) & -P \sin(\alpha) \\ -\sin(\alpha) & 0 & \cos(\alpha) & -P \cos(\alpha) \\ 0 & -1 & 0 & 0 \\ 0 & 0 & 0 & 1 \end{bmatrix} \quad (5.2)$$

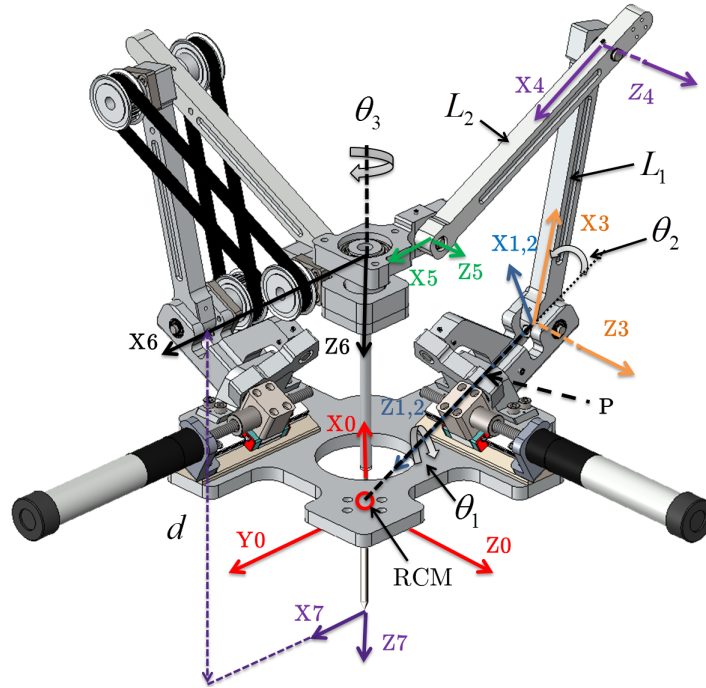


Figure 5.1: Coordinate frames attached to the right leg of the robot.

$${}^1_2T = \begin{bmatrix} \cos(\theta_1) & -\sin(\theta_1) & 0 & 0 \\ \sin(\theta_1) & \cos(\theta_1) & 0 & 0 \\ 0 & 0 & 1 & 0 \\ 0 & 0 & 0 & 1 \end{bmatrix} \quad (5.3)$$

$${}^2_3T = \begin{bmatrix} \sin(\theta_2) & \cos(\theta_2) & 0 & 0 \\ 0 & 0 & -1 & 0 \\ -\cos(\theta_2) & \sin(\theta_2) & 0 & 0 \\ 0 & 0 & 0 & 1 \end{bmatrix} \quad (5.4)$$

$${}^3_4T = \begin{bmatrix} -\cos(\theta_2) & -\sin(\theta_2) & 0 & L_1 \\ \sin(\theta_2) & -\cos(\theta_2) & 0 & 0 \\ 0 & 0 & 1 & 0 \\ 0 & 0 & 0 & 1 \end{bmatrix} \quad (5.5)$$

$${}^4_5T = \begin{bmatrix} \sin(\phi + \theta_2) & \cos(\phi + \theta_2) & 0 & L_2 \\ -\cos(\phi + \theta_2) & \sin(\phi + \theta_2) & 0 & 0 \\ 0 & 0 & 1 & 0 \\ 0 & 0 & 0 & 1 \end{bmatrix} \quad (5.6)$$

$${}^5_6T = \begin{bmatrix} \cos(\theta_3) & -\sin(\theta_3) & 0 & L_1 \sin(\phi) \\ 0 & 0 & 1 & 0 \\ -\sin(\theta_3) & -\cos(\theta_3) & 0 & 0 \\ 0 & 0 & 0 & 1 \end{bmatrix} \quad (5.7)$$

$i$	$\theta_i$	$d_i$	$a_i$	$\alpha_{i-1}$
1	$\alpha$	$P$	0	$-\pi/2$
2	$\theta_1$	0	0	0
3	$\theta_2 - \pi/2$	0	0	$\pi/2$
4	$\pi - \theta_2$	0	$L_1$ (130 mm)	0
5	$\theta_2 + \phi - \pi/2$	0	$L_2$ (120 mm)	0
6	$\theta_3$	0	$L_1 \sin(\phi)$	0
7	0	$d$	0	0

Table 5.1: Denavit-Hartenberg Parameters

$${}^6_7T = \begin{bmatrix} 1 & 0 & 0 & 0 \\ 0 & 1 & 0 & 0 \\ 0 & 0 & 1 & d \\ 0 & 0 & 0 & 1 \end{bmatrix} \quad (5.8)$$

As is shown in 5.95.9, the transformation matrix,  ${}^0_7T$ , between Frames 0 and 7 (tip of the needle) represents the forward kinematics of the right leg. It is produced by multiplying the transformation matrices consecutively.  ${}^0_7T$  provides the orientation and position of the robot's end-effector in the base coordinate system as a function of joint variables  $\theta_1$ ,  $\theta_2$ ,  $\theta_3$  and  $d$ . The complete form of the forward kinematics ( ${}^0_7T$ ) can be found in Appendix AA.

$$\begin{aligned} {}^0_7T &= {}^0_1T \times {}^1_2T \times {}^2_3T \times {}^3_4T \times {}^4_5T \times {}^5_6T \times {}^6_7T \\ &= \begin{bmatrix} \sin(\phi + \theta_2)\dots & -\sin(\phi + \theta_2)\dots & \cos(\phi + \theta_2)\dots & L_2 \sin(\alpha) \\ \sin(\alpha)\dots & \sin(\alpha)\dots & \cos(\phi + \theta_2)\dots & L_2 \cos(\alpha) \\ -\cos(\theta_1)\dots & \cos(\phi + \theta_2)\dots & \sin(\phi + \theta_2)\dots & -(\sin(\theta_1)\dots) \\ 0 & 0 & 0 & 1 \end{bmatrix} \quad (5.9) \end{aligned}$$

The same approach can be used for the left leg of the robot to derive the forward kinematics using coordinate systems attached to the left leg and new sets of joint variables ( $\hat{\theta}_1$ ,  $\hat{\theta}_2$ ,  $\hat{\theta}_3$  and  $\hat{d}$ ), as shown in Figure 5.25.2 and Equation 5.105.10. The forward kinematics for both legs yield the same results since they share the same end-effector and base coordinate frames.

$${}^0_{\hat{7}}\hat{T} = \begin{bmatrix} \sin(\phi + \hat{\theta}_2)\dots & -\sin(\phi + \hat{\theta}_2)\dots & \cos(\phi + \hat{\theta}_2)\dots & \hat{L}_2 \sin(\alpha) \\ \sin(\alpha)\dots & \sin(\alpha)\dots & \cos(\phi + \hat{\theta}_2)\dots & \hat{L}_2 \cos(\alpha) \\ -\cos(\hat{\theta}_1)\dots & \cos(\phi + \hat{\theta}_2)\dots & \sin(\phi + \hat{\theta}_2)\dots & -(\sin(\hat{\theta}_1)\dots) \\ 0 & 0 & 0 & 1 \end{bmatrix} \quad (5.10)$$

There are two sets of joint variables that can provide the forward kinematics of the robot, namely:  $\theta_1$ ,  $\theta_2$ ,  $\theta_3$ ,  $d$  and  $\hat{\theta}_1$ ,  $\hat{\theta}_2$ ,  $\hat{\theta}_3$ ,  $\hat{d}$ , corresponding to each leg of the mechanism. However, the joint variables that are actuated and in turn measured must be used to derive the forward kinematics. Considering the right leg of the robot, it can be realized that joint variables  $\theta_3$

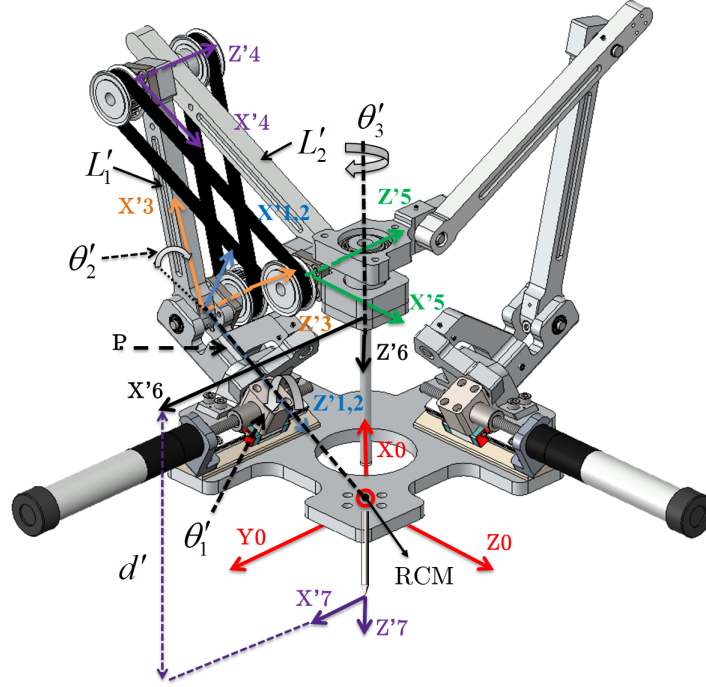


Figure 5.2: Coordinate frames attached to the left leg of the robot.

and  $d$  are actuated by the Roll and linear insertion motors, respectively, and  $\theta_1$  is actuated using a crank-slider mechanism, while  $\theta_2$  is not directly actuated. The same situation exists for the other leg of the robot. The parallel configuration makes it possible to actuate pitch and yaw (i.e.,  $\theta_1$ ,  $\hat{\theta}_1$ ) at the base of the robot to reduce the floating inertia. These two DOFs tilt the needle/probe around the RCM to target the needle. In this regard, it is required to find  $\theta_2$  as a function of  $\theta_1$  and  $\hat{\theta}_1$  and then the forward kinematics is based on the desired four joint variables that are actuated (i.e.,  $\theta_1$ ,  $\hat{\theta}_1$ ,  $\theta_3$ ,  $d$ ). The fact that the two legs can rotate relative to each other makes it complicated to find  $\theta_2$  as a function of  $\theta_1$  and  $\hat{\theta}_1$ . Considering geometry-based relations between frames attached to the legs,  $\theta_2$  can be found as:

$$\theta_2 = \alpha - \arctan\left(\frac{U}{V}\right) + \frac{\pi}{2} - \phi, \quad (5.11)$$

where  $U$  and  $V$  are functions of  $\theta_1$  and  $\hat{\theta}_1$  (more details can be found in Appendix AA). The combination of  ${}^0_7T$  and Equation 5.115.11 provides the analytical forward kinematics of the proposed parallel mechanism using the actuated joint variables.

## 5.2 Inverse Kinematics

The inverse kinematics determine the required motion of each joint in order to guide the robot end-effector towards a desired known position. Given the desired position of the robot end-effector in the base coordinate system,  $[X \ Y \ Z]^T$ , the inverse kinematics is derived as shown in Equation 5.125.12:

$$\begin{aligned}
d &= \sqrt{X^2 + Y^2 + Z^2} + L_1 \cos(\phi) \\
\theta_1 &= \arctan \left( \frac{\mathbf{V}(3)}{\mathbf{V}(2) \sin(\alpha) - \mathbf{V}(1) \cos(\alpha)} \right) \\
\dot{\theta}_1 &= \arctan \left( \frac{-\mathbf{V}(2)}{\mathbf{V}(3) \sin(\alpha) - \mathbf{V}(1) \cos(\alpha)} \right), \\
\text{where } \mathbf{V} &= \begin{bmatrix} X \\ \sqrt{X^2 + Y^2 + Z^2} \\ Y \\ \sqrt{X^2 + Y^2 + Z^2} \\ Z \\ \sqrt{X^2 + Y^2 + Z^2} \end{bmatrix}.
\end{aligned} \tag{5.12}$$

The Roll motion ( $\theta_3$ ) has no effect on the end-effector's position.

### 5.3 Workspace

Table 5.25.2 presents the required range of motion at each degree of freedom. Using the required range of motion from Table 5.25.2 and the forward kinematics of the robot from Equations 5.95.9 and 5.115.11, the end-effector's workspace can be drawn as shown in Figure 5.35.3. As can be seen in Figure 5.35.3, the workspace is part of a sphere centered at the RCM.

DOF	Range of Motion
Pitch ( $\theta_1$ )	$\pm 22.5^\circ$
Yaw ( $\dot{\theta}_1$ )	$\pm 22.5^\circ$
Insertion ( $d$ )	20 cm below the RCM
Roll ( $\theta_3$ )	$0^\circ - 180^\circ$

Table 5.2: Range of motion at each degree of freedom.

### 5.4 Velocity Analysis

#### 5.4.1 Velocity Propagation

Velocity propagation is a method of finding the translational and angular velocity of each link of a mechanism. It starts from the stationary base of the robot and then propagates velocity from one link to the adjoining link. This procedure would be repeated until the velocities related to each link of the robot are found. Equations 5.135.13 and 5.145.14 may be used to compute the velocity propagation from one link to another. Equation 5.135.13 is used when

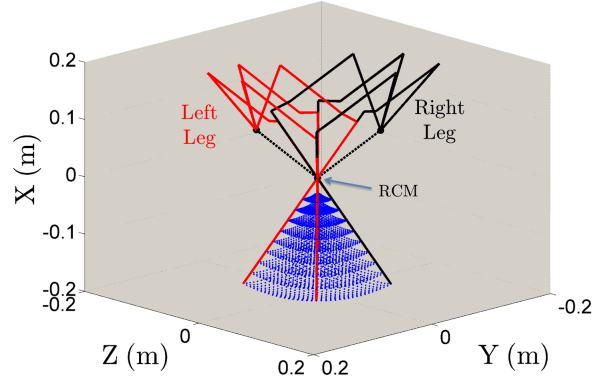


Figure 5.3: Robot's workspace inside its base coordinate system.

Joint  $i+1$  is a revolute joint and Equation 5.145.14 is used when Joint  $i+1$  is prismatic.

$$\begin{aligned} {}^{i+1}\boldsymbol{\omega}_{i+1} &= {}^i R^{i+1} \boldsymbol{\omega}_i + \dot{\theta}_{i+1} {}^{i+1} Z_{i+1} \\ {}^{i+1} \boldsymbol{v}_{i+1} &= {}^i R^{i+1} ({}^i v_i + {}^i \boldsymbol{\omega}_i \times {}^i P_{i+1}) \end{aligned} \quad (5.13)$$

$$\begin{aligned} {}^{i+1}\boldsymbol{\omega}_{i+1} &= {}^i R^{i+1} \boldsymbol{\omega}_i \\ {}^{i+1} \boldsymbol{v}_{i+1} &= {}^i R^{i+1} ({}^i v_i + {}^i \boldsymbol{\omega}_i \times {}^i P_{i+1}) + d^{i+1} Z_{i+1} \end{aligned} \quad (5.14)$$

The superscript shows the coordinate system in which the parameter is expressed and subscript presents the number of link. In this regard,  ${}^{i+1}\boldsymbol{\omega}_{i+1}$  represents the absolute angular velocity of Link  $i+1$  expressed in the coordinate system attached to Link  $i+1$  and  ${}^{i+1} \boldsymbol{v}_{i+1}$  represents the absolute translational velocity of the centre of Frame  $i+1$  in its own coordinate system.  ${}^i R^{i+1}$  provides the rotation matrix from coordinate system  $i$  to coordinate system  $i+1$ . Also,  ${}^i P_{i+1}$  is the position of the centre of Frame  $i+1$  in the coordinate system of Frame  $i$ . In addition,  $\dot{\theta}_{i+1}$  and  $d^{i+1} Z_{i+1}$  are the relative angular and linear velocity of Link  $i+1$  relative to Link  $i$ , respectively.

As with the forward kinematics, the velocities can be propagated for each leg of the parallel mechanism separately and the final result for the velocities of the end-effector (i.e., the needle) are the same. Equations 5.155.15 to 5.205.20 show the velocity propagation for the right leg of the robot. As can be seen in Figure 5.15.1, Links 0 and 1 are stationary, so  ${}^0 \boldsymbol{\omega}_0 = {}^1 \boldsymbol{\omega}_1 = [000]^T$  and  ${}^0 v_0 = {}^1 v_1 = [000]^T$ .

$$\begin{aligned} {}^2 \boldsymbol{\omega}_2 &= {}^2 R^1 \boldsymbol{\omega}_1 + \dot{\theta}_1 {}^2 Z_2 = \begin{bmatrix} 0 \\ 0 \\ \dot{\theta}_1 \end{bmatrix} \\ {}^2 v_2 &= {}^2 R^1 ({}^1 v_1 + {}^1 \boldsymbol{\omega}_1 \times {}^1 P_2) = \begin{bmatrix} 0 \\ 0 \\ 0 \end{bmatrix} \end{aligned} \quad (5.15)$$

$$\begin{aligned}
{}^3\omega_3 &= {}^3_2R^2\omega_2 + \dot{\theta}_2^3Z_3 = \begin{bmatrix} -\dot{\theta}_1 \sin(\theta_2) \\ \dot{\theta}_1 \cos(\theta_2) \\ \dot{\theta}_2 \end{bmatrix} \\
{}^3v_3 &= {}^3_2R({}^2v_2 + {}^2\omega_2 \times {}^2P_3) = \begin{bmatrix} 0 \\ 0 \\ 0 \end{bmatrix}
\end{aligned} \tag{5.16}$$

$$\begin{aligned}
{}^4\omega_4 &= {}^4_3R^3\omega_3 + (-\dot{\theta}_2)^4Z_4 = \begin{bmatrix} \dot{\theta}_1 \\ 0 \\ 0 \end{bmatrix} \\
{}^4v_4 &= {}^4_3R({}^3v_3 + {}^3\omega_3 \times {}^3P_4) = \begin{bmatrix} L_1\dot{\theta}_2 \sin(\theta_2) \\ -L_1\dot{\theta}_2 \cos(\theta_2) \\ -L_1\dot{\theta}_1 \sin(\theta_2) \end{bmatrix}
\end{aligned} \tag{5.17}$$

$$\begin{aligned}
{}^5\omega_5 &= {}^5_4R^4\omega_4 + \dot{\theta}_2^5Z_5 = \begin{bmatrix} \dot{\theta}_1 \sin(\phi + \theta_2) \\ \dot{\theta}_1 \cos(\phi + \theta_2) \\ \dot{\theta}_2 \end{bmatrix} \\
{}^5v_5 &= {}^5_4R({}^4v_4 + {}^4\omega_4 \times {}^4P_5) = \begin{bmatrix} L_1\dot{\theta}_2 \cos(\phi) \\ -L_1\dot{\theta}_2 \sin(\phi) \\ -L_1\dot{\theta}_1 \sin(\theta_2) \end{bmatrix}
\end{aligned} \tag{5.18}$$

$$\begin{aligned}
{}^6\omega_6 &= {}^6_5R^5\omega_5 + \dot{\theta}_3^6Z_6 = \begin{bmatrix} \dot{\theta}_1 \sin(\phi + \theta_2) \cos(\theta_3) - \dot{\theta}_2 \sin(\theta_3) \\ -\dot{\theta}_1 \sin(\phi + \theta_2) \sin(\theta_3) - \dot{\theta}_2 \cos(\theta_3) \\ \dot{\theta}_3 + \dot{\theta}_1 \cos(\phi + \theta_2) \end{bmatrix} \\
{}^6v_6 &= {}^6_5R({}^5v_5 + {}^5\omega_5 \times {}^5P_6) \\
&= \begin{bmatrix} \frac{L_1\dot{\theta}_1 \sin(\theta_3)}{2} (\sin(\theta_2) + \sin(2\phi + \theta_2)) + L_1\dot{\theta}_2 \cos(\phi) \cos(\theta_3) \\ \frac{L_1\dot{\theta}_1 \cos(\theta_3)}{2} (\sin(\theta_2) + \sin(2\phi + \theta_2)) - L_1\dot{\theta}_2 \cos(\phi) \sin(\theta_3) \\ 0 \end{bmatrix}
\end{aligned} \tag{5.19}$$

$$\begin{aligned}
{}^7\omega_7 &= {}^7R^6\omega_6 = \begin{bmatrix} \dot{\theta}_1 \sin(\phi + \theta_2) \cos(\theta_3) - \dot{\theta}_2 \sin(\theta_3) \\ -\dot{\theta}_1 \sin(\phi + \theta_2) \sin(\theta_3) - \dot{\theta}_2 \cos(\theta_3) \\ \dot{\theta}_3 + \dot{\theta}_1 \cos(\phi + \theta_2) \end{bmatrix} \\
{}^7v_7 &= {}^7R \left( {}^6v_6 + {}^6\omega_6 \times {}^6P_7 \right) \\
&= \begin{bmatrix} (L_1 \cos(\phi) - d) (\dot{\theta}_2 \cos(\theta_3) + \dot{\theta}_1 \sin(\theta_3) (\sin(\phi + \theta_2))) \\ (L_1 \cos(\phi) - d) (-\dot{\theta}_2 \sin(\theta_3) + \dot{\theta}_1 \cos(\theta_3) (\sin(\phi + \theta_2))) \\ d \dot{\theta}_3 \end{bmatrix} \quad (5.20)
\end{aligned}$$

The same procedure can be used for the other leg of the robot. The final result, which determines the velocity of robot end-effector, is the same, regardless of which leg was chosen for velocity propagation.

## 5.4.2 Jacobian Matrix

For each leg of the robot a Jacobian matrix ( $J$ ) can be derived that provides a linear transformation from joint velocities ( $\dot{\Theta}$ ) to the end-effector's Cartesian velocities as shown in 5.215.21:

$$v = J(\Theta) \cdot \dot{\Theta} \quad (5.21)$$

The Jacobian matrix can be expressed in any frame. It depends on the frame in which the velocity of the end-effector is expressed. Equation 5.225.22 and 5.235.23 show the Jacobian matrices related to the right leg of the robot for translational and angular velocities of the robot end-effector (i.e., needle). The velocities, and in turn the Jacobian Matrices, are expressed in the end-effector's frame (i.e., Frame 7, shown in Figure 5.15.1).

$$\begin{aligned}
{}^7v_7 &= {}^7J(\Theta) \cdot \dot{\Theta} \\
&= \begin{bmatrix} (L_1 \cos(\phi) - d) \sin(\phi + \theta_2) \sin(\theta_3) & (L_1 \cos(\phi) - d) \cos(\theta_3) & 0 \\ (L_1 \cos(\phi) - d) \sin(\phi + \theta_2) \cos(\theta_3) & (d - L_1 \cos(\phi)) \sin(\theta_3) & 0 \\ 0 & 0 & 1 \end{bmatrix} \cdot \begin{bmatrix} \dot{\theta}_1 \\ \dot{\theta}_2 \\ d \end{bmatrix} \\
\det({}^7J(\Theta)) &= -\sin(\theta_2 + \phi)(d - L_1 \cos(\phi))^2 \quad (5.22)
\end{aligned}$$

$$\begin{aligned}
{}^7w_7 &= {}^7J_w(\Theta) \cdot \dot{\Theta} \\
&= \begin{bmatrix} \sin(\phi + \theta_2) \cos(\theta_3) & -\sin(\theta_3) & 0 \\ -\sin(\phi + \theta_2) \sin(\theta_3) & -\cos(\theta_3) & 0 \\ \cos(\phi + \theta_2) & 0 & 1 \end{bmatrix} \cdot \begin{bmatrix} \dot{\theta}_1 \\ \dot{\theta}_2 \\ \dot{\theta}_3 \end{bmatrix} \\
\det({}^7J_w(\Theta)) &= -\sin(\theta_2 + \phi) \quad (5.23)
\end{aligned}$$

${}^7v_7$  and  ${}^7w_7$  represent the absolute translational and rotational velocities of the end-effector (i.e., needle's tip) expressed in the end-effector frame for the right leg. The same Jacobians can



be found for the left leg of the robot. Separating the Jacobian matrix into the translational and angular velocities of the end-effector (i.e.,  ${}^7J$  and  ${}^7J_w$ ) is a general practice. In this way, the Jacobians are square matrices without redundancy. Thus, depending on the task requirement either one or both of these Jacobians can be used to study the end-effector velocities. As mentioned previously, the Jacobian provides a mapping between the Cartesian velocities of the robot end-effector and the joint velocities. It also can be used to determine the relationship between the static forces applied to the robot end-effector and the required torque/force at each degree of freedom [1515]. This relationship can be derived by considering the principle of Virtual Work and using Equation 5.215.21, as is shown in Equation 5.245.24.

$$\tau = J^T(\Theta)F \quad (5.24)$$

$F$  and  $\tau$  represent the static forces applied to the end-effector and the corresponding required torque/force at each DOF, respectively. The principle of Virtual Work in combination with a simulation model (see Chapter 66) was used to determine the required torques at each degree of freedom. This information was then used to select suitable actuators.

## 5.5 Quantitative Measures of Workspace Attributes

### 5.5.1 Singularities

The values of joint variables that result in the Jacobian matrix becoming singular are called the singularities of a manipulator. At these singularities, the Jacobian is not invertible and as a result the manipulator loses one or more degrees of freedom (as viewed from Cartesian space) [1515]. Considering Equations 5.225.22 and 5.235.23, the singularities for translational and angular velocities can be found as:

$$\begin{aligned} \det({}^7J(\Theta)) &= -\sin(\theta_2 + \phi)(d - L_1 \cos(\phi))^2 = 0 \\ \longrightarrow \begin{cases} \theta_2 = -\phi \pm k\pi & k = 1, 2, 3, \dots \\ d = L_1 \cos(\phi) \end{cases} \end{aligned} \quad (5.25)$$

$$\begin{aligned} \det({}^7J_w(\Theta)) &= -\sin(\theta_2 + \phi) = 0 \\ \longrightarrow \theta_2 &= -\phi \pm k\pi \quad k = 1, 2, 3, \dots \end{aligned} \quad (5.26)$$

None of the singularities lies inside the robot's specified workspace (Table 5.25.2). This configuration, where  $d = L_1 \cos(\phi)$ , means that the robot end-effector is located at the RCM and regardless of any motion in the joint space, the Cartesian translational velocities of end-effector would be zero. This singularity is avoided since, during the actual medical interventions, the tip of needle is always far from the RCM. It should also be noted that the coordinate frame in which the Jacobian matrix is expressed does not affect the singular points. The singularities can be checked for both legs of the robot mechanism with the same results.

### 5.5.2 Manipulability Measure

At singular points, a manipulator loses one or more degrees of freedom, and is not capable of performing certain tasks. In fact, in proximity to singular points, the motion of the manipulator could fail to be well-conditioned [1515]. In other words, the ability of manipulator to move uniformly or apply forces uniformly in all directions is related to the distance from the singular points. Several measurements have been suggested to quantify this effect. Manipulability, suggested in [6262], is one such measure that considers the determinant of the Jacobian matrix as a measure of a robotic manipulator's dexterity. The manipulability measure,  $W$ , is defined as:

$$W = \sqrt{\det(J(\Theta) \cdot J^T(\Theta))} \quad (5.27)$$

However, for a nonredundant manipulator with a square Jacobian matrix, it reduces to:

$$W = |\det(J(\Theta))| \quad (5.28)$$

Accordingly, a good manipulator has large areas of its workspace characterized by high values of manipulability [1515]. In fact, the manipulability measure can be used to quantify the distance from the singularities within the required workspace of a manipulator. Figure 5.45.4 depicts the variation of manipulability measure for each leg of the robot.

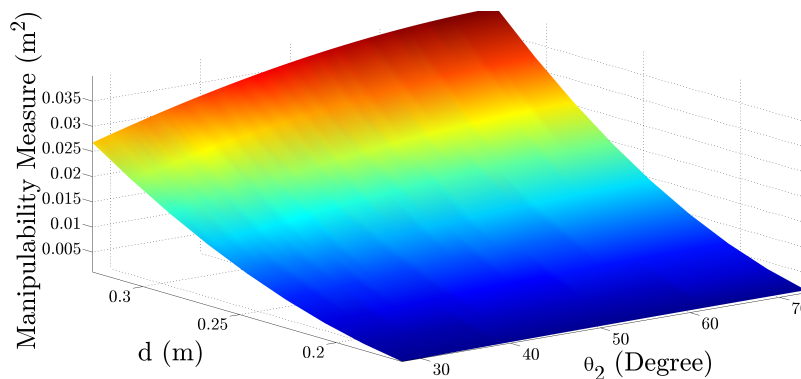


Figure 5.4: Manipulability measure within the required workspace.

Manipulability is a questionable measure of kinematic invertibility. It is clear that the manipulability measure is meant to assess the invertibility of the Jacobian matrix by considering the absolute value of its determinant. However, as was pointed out by Forsythe and Moler, [6363], mathematically, this measure is meaningless for assessing invertibility.

### 5.5.3 Isotropy and Condition Number

Isotropy, suggested by Salisbury and Craig [6464], is defined as the condition number of the Jacobian and has been proven to be a good measure of a manipulator's dexterity in moving or applying forces uniformly in all directions. The condition number is defined as the ratio between the maximum and minimum of Eigen values of the Jacobian matrix as shown in Equation 5.295.29:

$$C(J) = \left| \frac{\sigma_{\max}}{\sigma_{\min}} \right| \quad (5.29)$$

The lower the condition number, the better the ability of the manipulator to produce uniform motions or apply uniform forces in all directions. Also, points within the workspace that have the lowest condition number are the best to minimize error propagation from input (i.e., joint space) to output (i.e., Cartesian space) [6464]. The best condition occurs when  $C(J) = 1$ , meaning that the Jacobian matrix satisfies two conditions: 1) its columns are orthogonal, and 2) its column vectors have equal magnitude. This ideal condition is called isotropy. In an isotropic condition, the manipulator has the same ability to move or apply forces in different directions. This ideal situation may or may not exist for a given design.

### Isotropy of the Parallel Mechanism

As was explained previously, the Jacobian matrix can be used to analyse the kinematic performance of a mechanism and the condition number of the Jacobian matrix can be used to assess directional uniformity. However, for the proposed parallel mechanism, which is a combination of two legs, there is not a linear mapping between the joint velocities (i.e.,  $\dot{\theta}_1, \dot{\theta}_1, \dot{\theta}_3, \dot{d}$ ) and the end-effector velocities in Cartesian space, so a Jacobian matrix cannot be developed. In order to address this issue, the forward kinematics of the robot can be used to check the performance of the whole parallel mechanism. In this regard, at each point within the robot's workspace, the joint variables can be changed by some small value to study the overall effect on the position of the end-effector within Cartesian space. pitch, yaw and linear insertion (i.e.,  $\theta_1, \theta_1$  and  $d$ ) are the three DOFs that determine the position of the end-effector within Cartesian space. Pitch and yaw are the two important DOFs for targeting tumours, while linear insertion is done independently after targeting is finalized and pitch and yaw are locked. Thus, uniformity in the pitch and yaw DOFs is of primary importance for the proposed parallel mechanism and must be studied. The pitch and yaw degrees of freedom correspond to end-effector motions along the Z and Y axes of the base frame as shown in Figure 5.15.1. Thus, at each point within the robot's workspace, the joint variables corresponding to the pitch and yaw motions ( $\theta_1, \theta_1$ ) may be changed by the same small value (i.e.,  $\theta_1 \pm \sigma, \theta_1 \pm \sigma$ ) and the corresponding movements along Z and Y direction may be compared to find the ratio between them. Figure 5.55.5 depicts the ratio variation within the workspace.

As shown in Figure 5.55.5, the motion ratio varies between 0.4 and 2.6. The best condition at any insertion depth within the workspace occurs at the centre of the workspace ( $\theta_1 = 0, \theta_1 = 0$ ), where the ratio is 1, which means a completely isotropic condition. It can also be realized that around the centre of workspace, the pitch and yaw degrees of freedom are completely decoupled. Near the centre of the workspace, the ratio is 1 and by reaching to the extremes of workspace the ratio rises or falls. Figure 5.65.6 presents the distribution of the motion ratio within the entire workspace. As may be observed, the majority of the points in the workspace have a motion ratio around 1, indicating good kinematic performance of the mechanism.

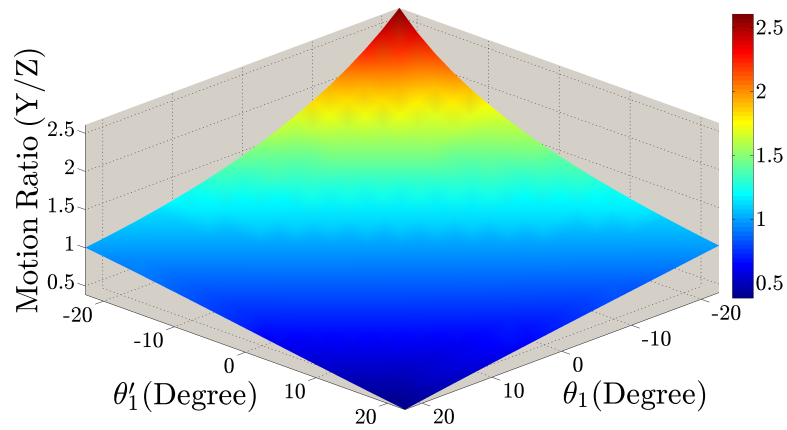


Figure 5.5: Directional uniformity within the robot workspace.

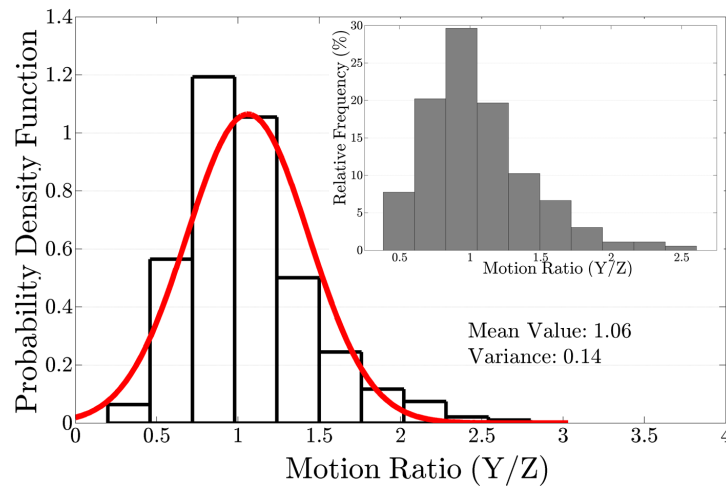


Figure 5.6: Distribution of the motion ratio with the workspace.

### Manipulability Ellipsoid

A manipulability ellipsoid [6565] is a graphical representation of the condition number within the manipulator's workspace. Let the singular value decomposition [6666] of the Jacobian matrix be:

$$J = U\Sigma V \quad (5.30)$$

Where  $U \in R^{m \times m}$  and  $V \in R^{n \times n}$  are orthogonal matrices and:

$$\Sigma = \left[ \begin{array}{ccc|c} \sigma_1 & & & 0 \\ & \sigma_2 & & \\ & & \ddots & \\ 0 & & & \sigma_m \\ & & & & 0 \end{array} \right] \quad (5.31)$$

For a nonredundant Jacobian matrix,  $\Sigma$  is a diagonal matrix as shown in equation 5.325.32.

$$\Sigma = \begin{bmatrix} \sigma_1 & & & 0 \\ & \sigma_2 & & \\ & & \ddots & \\ 0 & & & \sigma_m \end{bmatrix} \quad (5.32)$$

where  $(\sigma_1, \sigma_2, \sigma_m)$  are the Eigenvalues of the Jacobian matrix, and  $U = [U_1 \ U_2 \ \dots \ U_m]$  are the corresponding Eigenvectors. It can be shown that realizable velocities of the manipulator's end-effector using joint velocities  $\dot{\Theta}$  such as  $\dot{\Theta} = \dot{\theta}_1^2 + \dot{\theta}_2^2 + \dots + \dot{\theta}_m^2 \leq 1$ , is an ellipsoid with axes that lie in the direction of the Eigenvectors of the Jacobian and the corresponding Eigenvalues determine the length of each axis [6565]. This ellipsoid is called the manipulability ellipsoid and provides a good means for analysis and design of robotic manipulators. In an isotropic condition ( $C(J) = 1$ ), the manipulability ellipsoid is a sphere.

### Manipulability Ellipsoid for Each Leg of the Robot

Although the proposed parallel mechanism does not have a single unified Jacobian matrix, each leg of the robot has a Jacobian matrix since they are simple serial kinematic chains. Thus, it is possible to study the kinematic performance of each leg by considering the individual Jacobian matrix (Equations 5.225.22 and 5.235.23). Nonetheless, the proposed robot is intended to be used for targeting cancerous cells; therefore, the surgical needle is rotated around the RCM to target the cancerous tumours and then the linear insertion of the surgical tool is performed by another decoupled degree of freedom. Thus, the Jacobian matrix for the angular velocities (Equation 5.235.23) was considered to evaluate the robot's condition number within its workspace by drawing the manipulability ellipsoids. Figure 5.75.7 shows the manipulability ellipsoids for each leg of the robot considering the Jacobian matrix related to the angular velocities of the end-effector.

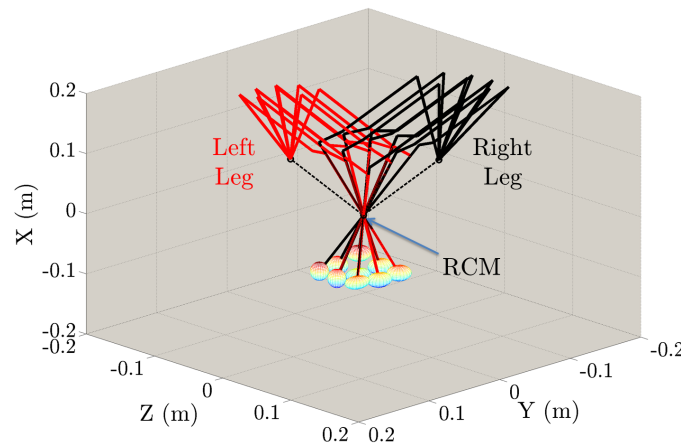


Figure 5.7: Manipulability ellipsoid for each leg of the robot.

As can be seen in Figure 5.75.7, the ellipsoids are the same for both legs of the robot since they have the same Jacobian. The condition number varies between 1 (isotropic condition) to maximum of 1.48, meaning that the proposed robot is capable of orienting the surgical needle

around different axis quite uniformly. Over the workspace of the robot, the ellipsoids are lose to spherical.

## 5.6 Crank–Slider Mechanism

As shown in Figure 5.85.8, the proposed robot benefits from two crank–slider mechanisms that actuate the rotational DOFs (i.e., the pitch and yaw) near the stationary base of the robot. The crank–slider mechanism provides a considerable mechanical advantage to provide the torque required to tilt the trocar while minimizing the amount of angular backlash in the pitch and yaw DOFs. The translational motion along the ball-screw axis actuates the rotational degree of freedom. Thus, the relationship between the angular rotation (i.e.,  $\beta$ ) and the translational motion along the ball-screw axis (i.e.,  $S$ ) must be found.

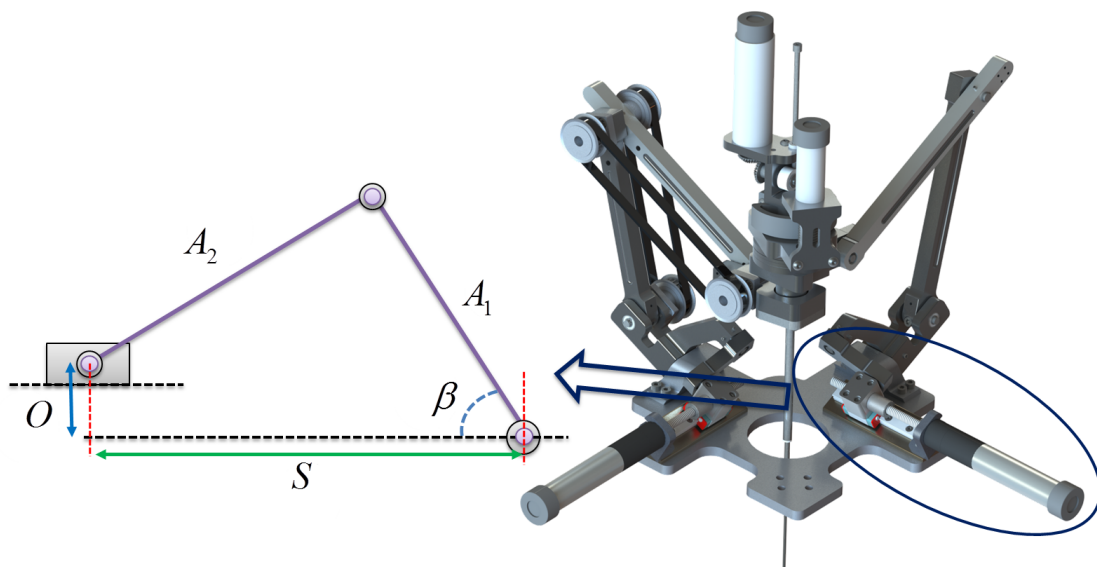


Figure 5.8: Crank–slider mechanism.

As shown in Figure 5.85.8,  $A_1$  and  $A_2$  are the lengths of two linkages and  $O$  is the offset distance between the translational motion axis and the angular rotation axis. Equation 5.335.33 describes the translational motion along the ball-screw axis as a function of the angular tilt of the corresponding leg of the robot around the RCM (i.e., pitch or yaw). In addition, Equations 5.345.34 and 5.355.35 represent the velocity analysis of the crank–slider mechanism.

$$S = A_1 \cos(\beta) + \left( A_2 \sqrt{1 - \left( \frac{A_1 \sin(\beta) - O}{A_2} \right)^2} \right) \quad (5.33)$$

$$\dot{S} = \left( \frac{A_1 \cos(\beta)(O - A_1 \sin(\beta))}{A_2 \sqrt{1 - \left(\frac{A_1 \sin(\beta) - O}{A_2}\right)^2}} - A_1 \sin(\beta) \right) \dot{\beta} \quad (5.34)$$

$$\frac{dS}{d\beta} = \frac{A_1 \cos(\beta)(O - A_1 \sin(\beta))}{A_2 \sqrt{1 - \left(\frac{A_1 \sin(\beta) - O}{A_2}\right)^2}} - A_1 \sin(\beta) \quad (5.35)$$

The angular rotation ( $\beta$ ) as a function of the translational motion ( $S$ ) is required to have a complete solution for both the forward and inverse kinematics of the crank–slider mechanism. As is depicted in Figure 5.95.9, by knowing  $S$ ,  $O$ ,  $A_1$  and  $A_2$ , it is possible to find angle  $\beta$  via the intersection between two circles with the radius of  $A_1$  and  $A_2$ . Using this geometric solution, Equation 5.365.36 determines  $\beta$  as a function of  $S$ .

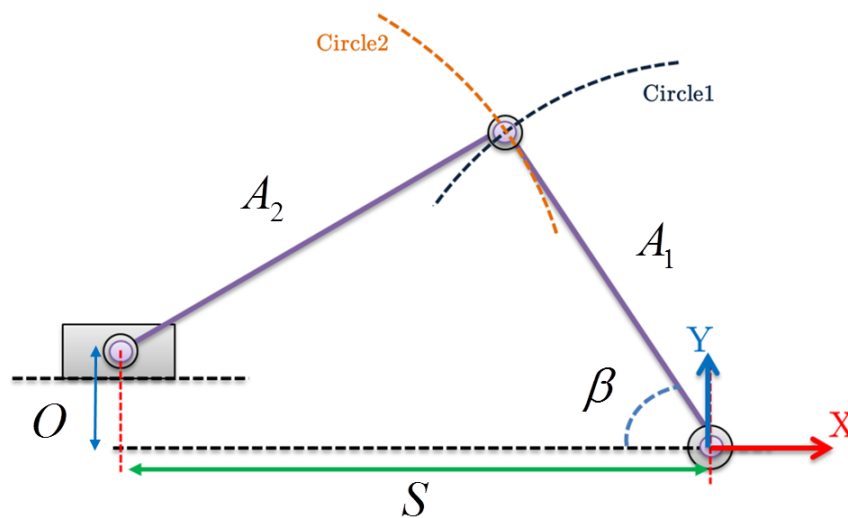


Figure 5.9: Geometry-based solution for crank–slider mechanism.

$$\begin{aligned}
\text{Intersection of the Circles: } &\longrightarrow \begin{cases} X^2 + Y^2 = A_1^2 \\ (X + S)^2 + (Y - O)^2 = A_2^2 \end{cases} \\
\implies OY - XS &= \frac{1}{2}(A_1^2 - A_2^2 + O^2 + S^2), \\
\text{where } Y = A_1 \sin(\beta) \quad \text{and} \quad X &= -A_1 \cos(\beta) \\
\implies O \sin(\beta) + S \cos(\beta) &= \frac{1}{2A_1}(A_1^2 - A_2^2 + O^2 + S^2), \\
\text{where } O \sin(\beta) + S \cos(\beta) &= \sqrt{O^2 + S^2} \sin(\beta + \arctan(\frac{S}{O})) \\
\implies \beta = \pi - \arcsin(\frac{1}{2A_1 \sqrt{O^2 + S^2}}(A_1^2 - A_2^2 + O^2 + S^2)) - \arctan(\frac{S}{O}) &\quad (5.36)
\end{aligned}$$

The forward and inverse kinematics of the parallel mechanism are provided by Equations 5.95.9, 5.115.11 and 5.125.12. The pitch and yaw motions (i.e.,  $\theta_1$  and  $\dot{\theta}_1$ ) are actuated using the crank–slider mechanism, requiring knowledge of the crank–slider kinematics. The angular rotation of the crank ( $\beta$ ) determines the pitch and yaw rotations ( $\theta_1$  and  $\dot{\theta}_1$ ) and the translational motion of the slider ( $S$ ) is the actuation parameter controlled by the linear spindle actuators. Thus, Equations 5.335.33 and 5.365.36 are used as part of a complete kinematic analysis of the parallel mechanism.

## 5.7 Conclusion

A kinematic analysis of the parallel mechanism of the robot was performed and quantitative measures of workspace attributes were studied. Forward kinematics, inverse kinematics and velocity propagation were studied considering one of the robot’s legs and then extended to the parallel mechanism considering the actuated joint variables. Kinematic performance of the robot was studied and it was shown that the robot end-effector’s motion is well-conditioned within the required workspace. The next chapter describes a simulated model of the robot that can be used to validate the kinematic analysis presented in the current chapter.



# Chapter 6

## Simulation

### 6.1 Introduction

In order to evaluate the kinematics and performance of the robot, a kinematics-based simulation of the robot is required. The SimMechanics simulation environment (Matlab R2012b, The MathWorks Inc.) was used to produce an accurate model of the robot. This model provides the possibility of studying both the kinematics and dynamics of the robot. Figure 6.16.1 shows the simulation environment. The simulation model uses numerical methods to solve the kinematics and dynamics of the parallel mechanism and it is completely independent from the analytical solution developed in Chapter 55. Only the length, mass and inertia of the linkages, along with coordinate frames definitions, is specified. Thus, the simulation model may be used to independently evaluate the analytical solution developed in Chapter 55.

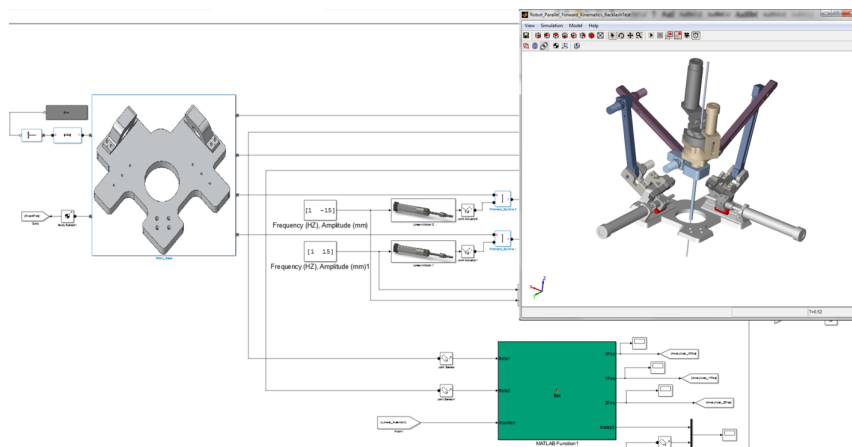


Figure 6.1: Model of the robot in SimMechanics.

The fact that the model of the robot is generated in Simulink (Matlab R2012b, The MathWorks Inc.) makes it easy to evaluate the kinematic analysis of the robot that was presented in the Chapter 55. In addition, the simulation provides a virtual environment for testing control strategies, path planning and other experiments.

## 6.2 Forward Kinematics Evaluation

Evaluation of the forward kinematics was performed by comparing the result of simulation in SimMechanics and the results of the analytical forward kinematics presented by Equations 5.95.9 or 5.105.10. For evaluation purposes, sinusoidal motions were applied to the actuated DOFs in both the analytical and the SimMechanics models and the results (i.e., the absolute position of the robot end-effector) were compared. For the two linear spindles that actuate the crank-slider mechanisms, sinusoidal motions with an amplitude of 15 mm and the frequency of 1 Hz were applied. In addition, the linear insertion was oscillated with an amplitude of 40 mm and a frequency of 0.5 Hz, while the tip of the end-effector (i.e., needle) was initially 8 cm below the RCM. The roll motion has no effect on the absolute position of the robot end-effector so it was excluded from the evaluation procedure. Figures 6.26.2, 6.36.3 and 6.46.4 show the absolute position of the end effector along the axis of the base coordinate system (Frame 0, shown in Figure 5.15.1) for one such motion.

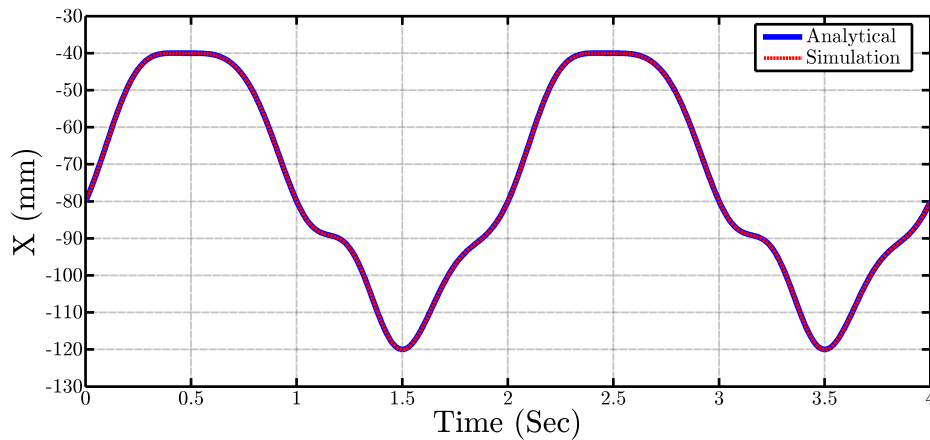


Figure 6.2: End-effector's absolute position along the X axis.

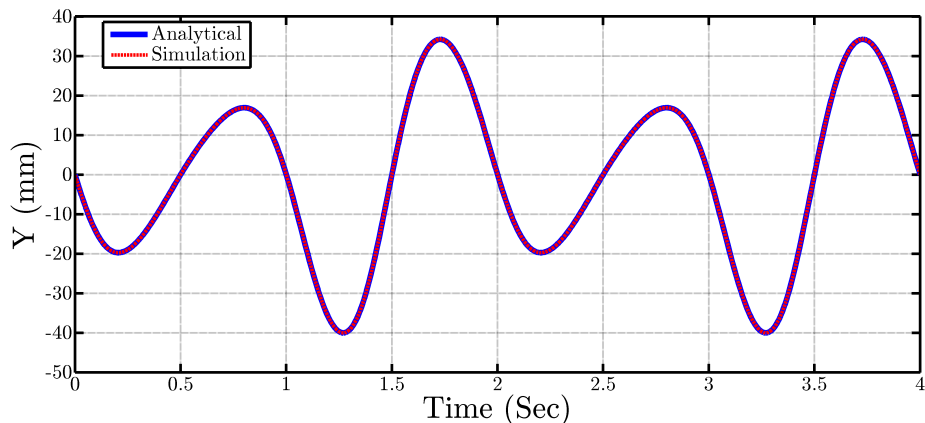


Figure 6.3: End-effector's absolute position along the Y axis.

As is shown in Figures 6.26.2 to 6.46.4, the results from the analytical solution for forward kinematic and the simulation in SimMechanics are completely matched. Although two perfect

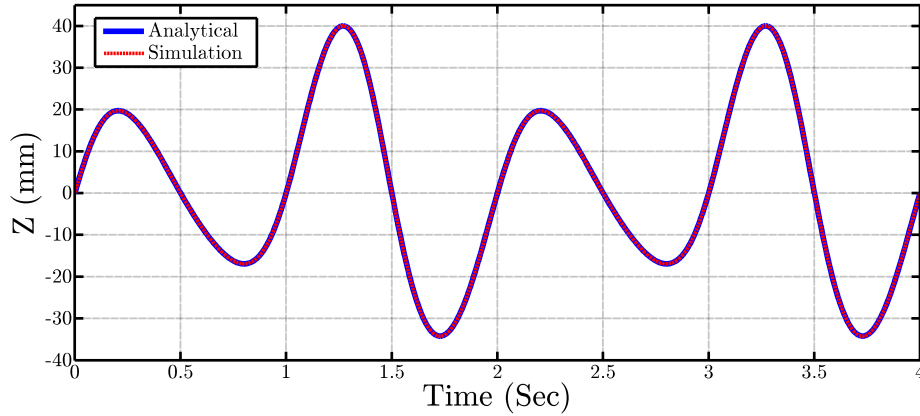


Figure 6.4: End-effector's absolute position along the Z axis.

models of a mechanism are compared here, this evaluation validates both the analytical equations and the simulation accuracy. The analytical solutions will be used to control the robot's motions and applied forces, while the simulation provides a realistic model of the robot to assess its performance in a virtual reality environment.

### 6.3 Inverse Kinematics Evaluation

Tracking a predefined path with the robot end-effector (i.e., needle's tip) is an established method to evaluate the inverse kinematic solution using the simulation model. In this regard, a circular path in Y-Z plane of the base coordinate frame was tracked by the end-effector. As shown in Figure 6.56.5, the circular path has a diameter of 40 mm and is located 80 mm beneath the RCM.

The position of each point along the circular path is known in the base coordinate frame. Thus, given the desired position of the robot end-effector on the circular path in the base coordinate system,  $[X \ Y \ Z]^T$ , the inverse kinematics (Equation 5.125.12) are used to find the corresponding joint motion to track the circular path. Figure 6.66.6 represents the results of the inverse kinematic evaluation for tracking a desired circular path.

### 6.4 Velocities and Jacobian Evaluation

In order to validate the Jacobian matrix using the simulation results from SimMechanics, the same sinusoidal motions (Section 6.26.2) are applied to the corresponding actuated degrees of freedom and the absolute velocities of the robot end-effector expressed at its coordinate system are compared. Figures 6.76.7, 6.86.8 and 6.96.9 show the absolute velocities of the end-effector along the X, Y and Z axes of the end-effector coordinate system.

As shown in Figures 6.76.7, 6.86.8 and 6.96.9, the results of simulation and the analytical Jacobian matrix yield the same results which validates both the analytical solution for the velocity analysis and the simulation model in SimMechanics.

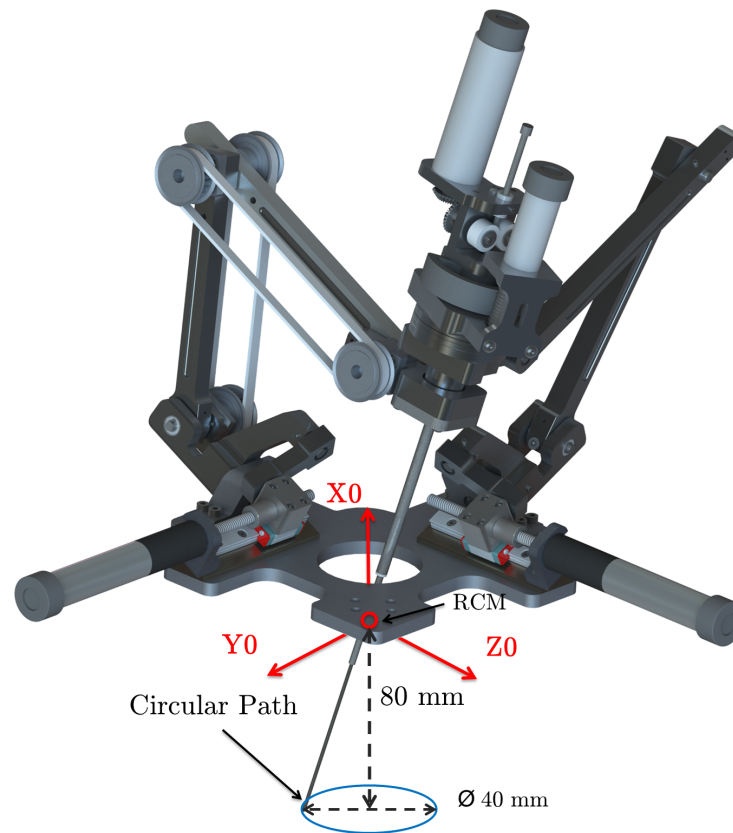


Figure 6.5: The desired circular path for tracking.

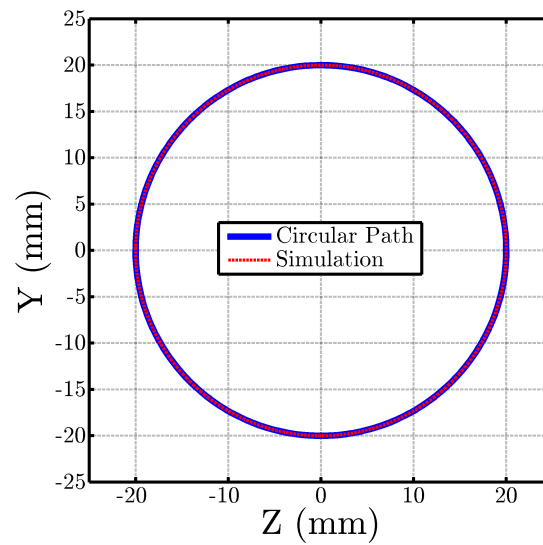


Figure 6.6: Tracking a circular path.

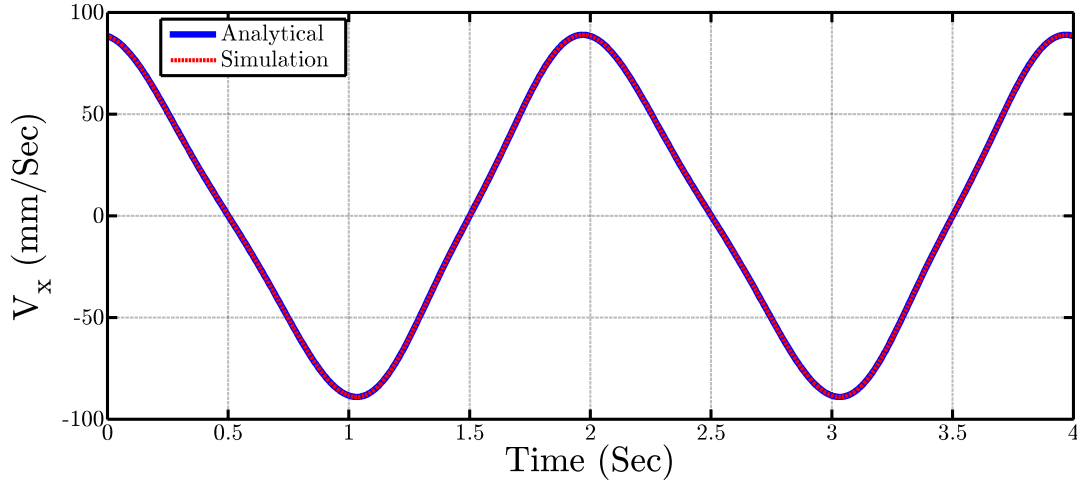


Figure 6.7: End-effector's absolute velocity along the X axis.

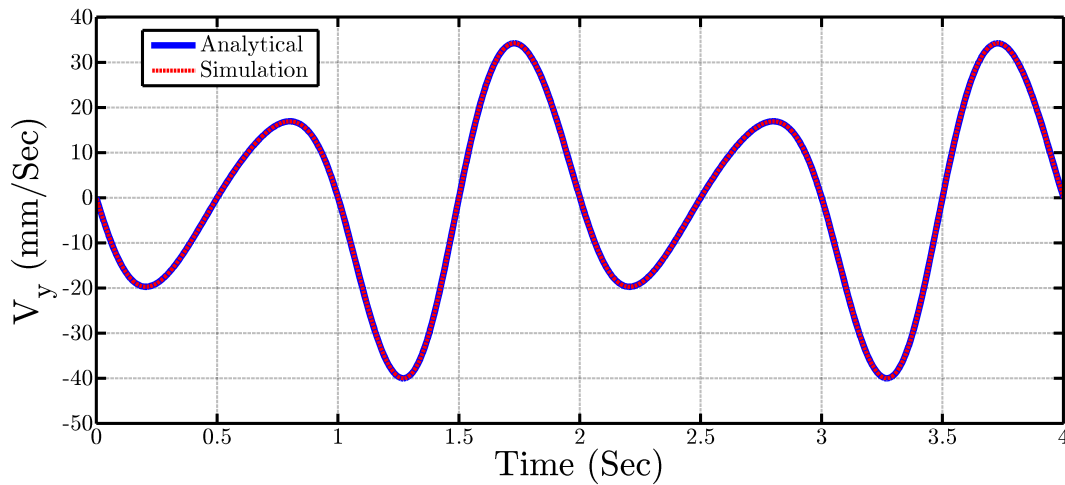


Figure 6.8: End-effector's absolute velocity along the Y axis.

## 6.5 Effect of Possible Mechanical Imperfections

The model of the robot in SimMechanics was mutually validated by the analytical equations from Chapter 55. It was shown that the model of the robot in SimMechanics provides a reliable simulation environment to study the robot's performance. Studying the effect of possible mechanical errors due to imperfections such as backlash in actuators and machining errors is one of the most important issues that need to be studied. In this regard, it is necessary to assess the sensitivity of the robot's positioning accuracy to such mechanical errors.

### 6.5.1 Effect of Backlash on Positioning Accuracy

Backlash is one of the main mechanical imperfections associated with an actuator that can affect its mechanical positioning accuracy. It is required to study the overall effect of actuator backlash on the positioning of the robot's end-effector (i.e., tip of the surgical needle). The

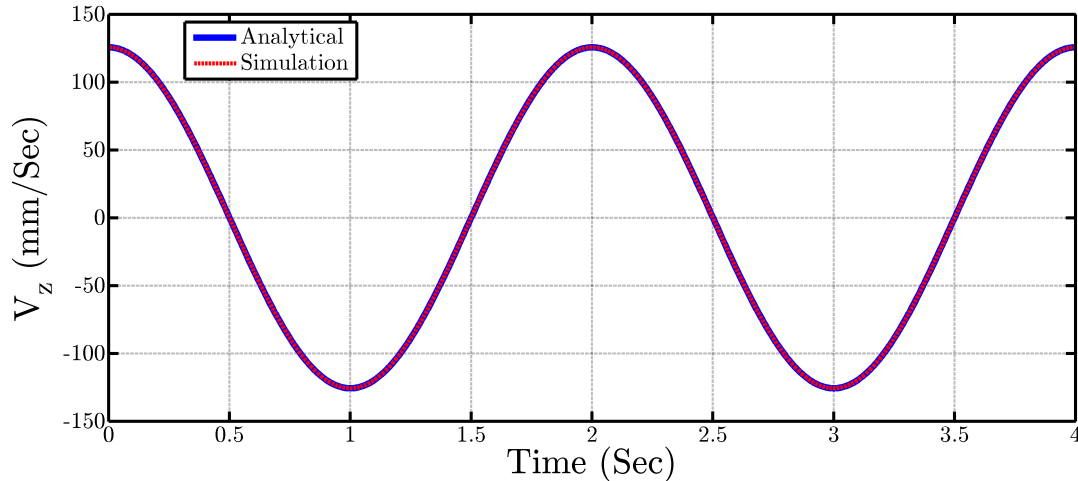


Figure 6.9: End-effector's absolute velocity along the Z axis.

proposed robot has four actuated degrees of freedom to orient and position the end-effector including Pitch, Yaw, Linear insertion and Roll.

The Roll and linear insertion DOFs are actuated using two small brushless DC motors (EC-max 16 and EC 22, Maxon Motor) without a gearbox; motion transmission is performed by cable-driven and friction-based systems, respectively. Therefore, these two DOFs are considered to be zero backlash. On the other hand, small linear spindle drives and ball-screws (GP 16, Maxon Motor) were chosen to actuate the Pitch and Yaw motions via the crank–slider mechanism. This method of actuation provided a compact design to gain high mechanical advantage and positioning accuracy. However, the mechanical positioning accuracy of the spindle drive is still limited by the backlash or play of the nut along the screw. The spindle drives are reported to have an overall backlash of 0.039 mm. Using the SimMechanics model of the robot, it is possible to study the effect of the backlash on the positioning accuracy of the end-effector by adding a known amount of backlash to the positioning commands of the actuators corresponding to Pitch and Yaw degrees of freedom. Figure 6.106.10 shows how backlash is added inside the SimMechanics simulation.

The sinusoidal motion commands (see Section 6.26.2) are applied to Pitch, Yaw and linear insertion motions while the backlash of 0.039 mm is applied to the motion commands of the linear spindles which actuates the crank–sliders. The sinusoidal motion commands cover the entire workspace of the robot, while the positioning error of the end-effector due to the backlash is recorded. Table 6.16.1 reports the maximum positioning error of positioning along the axes of robot's base coordinate frame, as shown in Figure 6.56.5.

As may be observed from Table 6.16.1, the positioning error caused by the existing backlash is small and negligible. However, this source of error should be considered as an intrinsic characteristic of the robot's actuation in the simulation model.

## 6.5.2 Effect of Possible Machining Errors

Although the ideal is to have a perfect machining process, the mechanical imperfections caused by machining errors are inevitable. In this regard, studying the effect of misalignments caused

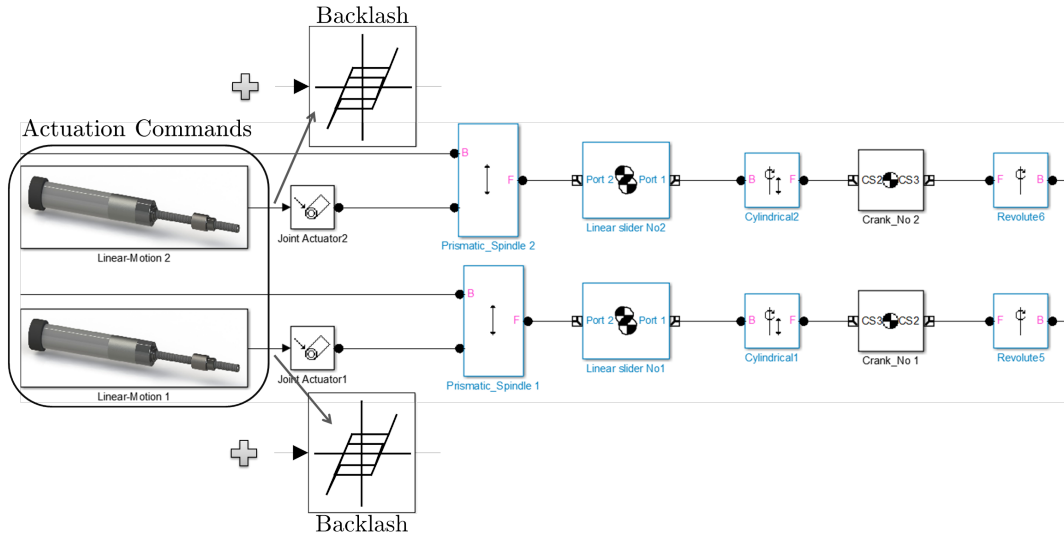


Figure 6.10: End-effector’s absolute velocity along the Y axis.

Table 6.1: The positioning errors caused by actuation backlash.

Source of Error	Positioning Error along X axis	Positioning Error along Y axis	Positioning Error along Z axis
Backlash of the linear spindles (0.039 mm)	0.08 mm	0.04 mm	0.04 mm

by machining and assembly errors prior to the actual construction of the robot provides helpful information about the sensitivity of the robot’s positioning accuracy in response to possible misalignments. In addition, improper machining may cause the mechanism to lock, especially considering the fact that the proposed robot has a parallel mechanism. Thus, it is also required to study the how machining error may affect the motion of the robot.

The model of the robot in SimMechanics provides a virtual simulation environment to study the effect of mechanical imperfections such as machining errors. In this regard, the joint axes were inclined from their ideal orientation in two directions to simulate the effect of joint-misalignment caused by possible machining errors. For example, if the ideal joint axis for one joint is  $[0 \ 1 \ 0]$  in its corresponding coordinate system, the inclined version would be  $[\Sigma \ 1 \ \Sigma]$ , where  $\Sigma$  stands for the amount of joint deviation. There are 9 deviation values (i.e.,  $\Sigma_1, \Sigma_2, \dots, \Sigma_9$ ) for a summation of 9 joints in each leg of the parallel mechanism. The deviation ( $\Sigma$ ) varies between 0 to 0.015 causing angular deviations of up to almost 1 degree in each direction. Since the mechanism has a parallel configuration, it is necessary to check different combination of deviations (in positive and negative directions) and run the model iteratively in SimMechanics to find the maximum positioning error caused by the joint deviations. In this regard, sinusoidal motions (Section 6.26.2) are applied to the corresponding actuated degrees of freedom to ensure that the entire workspace is covered, while considering different combi-

nations of deviations. Figures 6.116.11, 6.126.12 and 6.136.13 show the maximum positioning error along the axes of the robot's base coordinate systems for different combinations of joint deviations.

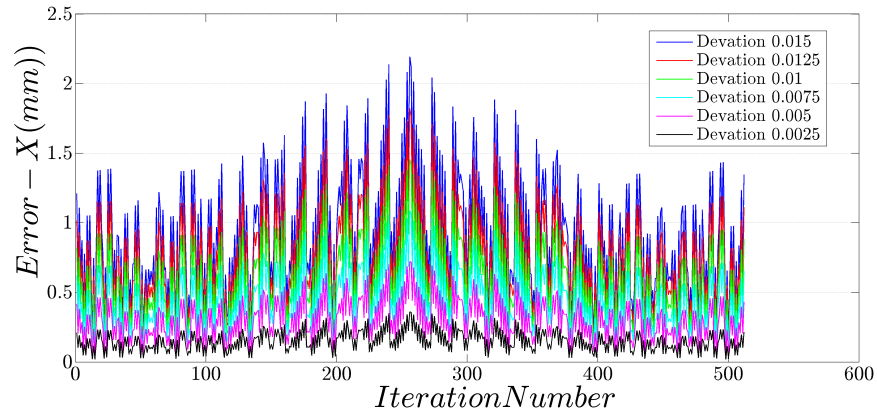


Figure 6.11: Positioning error caused by machining imperfections along X axis.

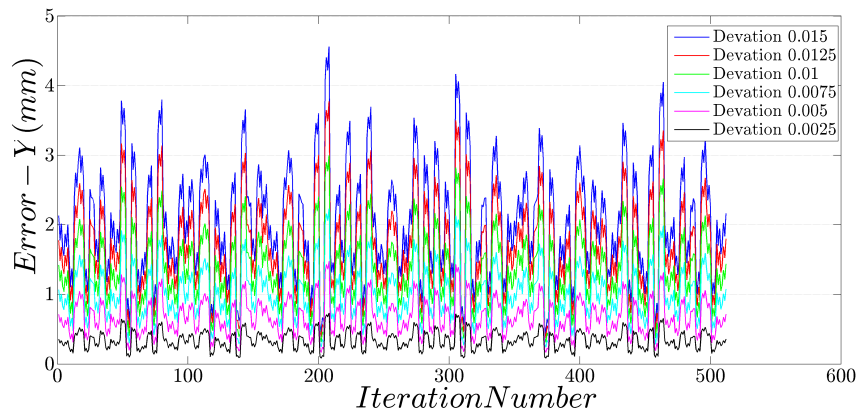


Figure 6.12: Positioning error caused by machining imperfections along Y axis.

Each simulation number in Figures 6.116.11, 6.126.12 and 6.136.13 corresponds to a different combination of deviations. As can be seen, for each axis a certain combination of joint deviations (i.e., simulation number) causes the maximum of positioning error, and the amount of error increases as the deviation increases. In addition, along different axes, different combinations of joint deviation cause the maximum of positioning error. Figure 6.146.14 depicts the maximum positioning error along each axis of the base coordinate-frame as the joint deviation increases.

All of the linkages of the robot's mechanism are considered to be rigid in the SimMechanics model. Thus, it is expected that the simulation model would be locked due to the joint deviations. However, the robot's mechanism is not locked by the joint misalignment because there are two cylindrical joints in the mechanism which allow the robot to run in spite of having a combination of joint deviations in both legs. Figure 6.156.15 shows the cylindrical joints and



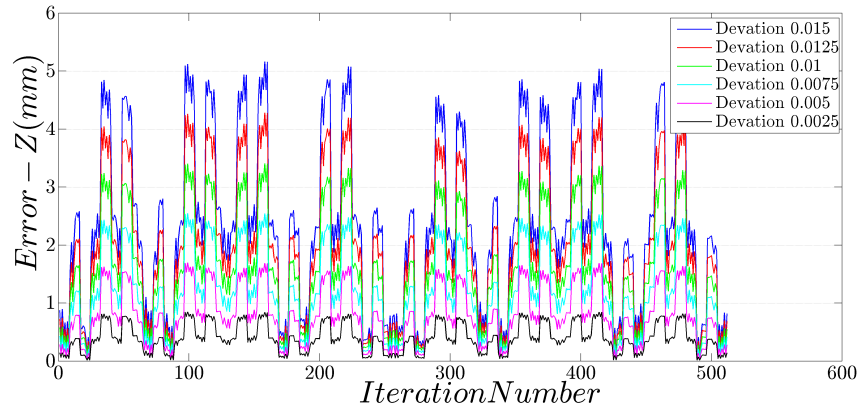


Figure 6.13: Positioning error caused by machining imperfections along Z axis.

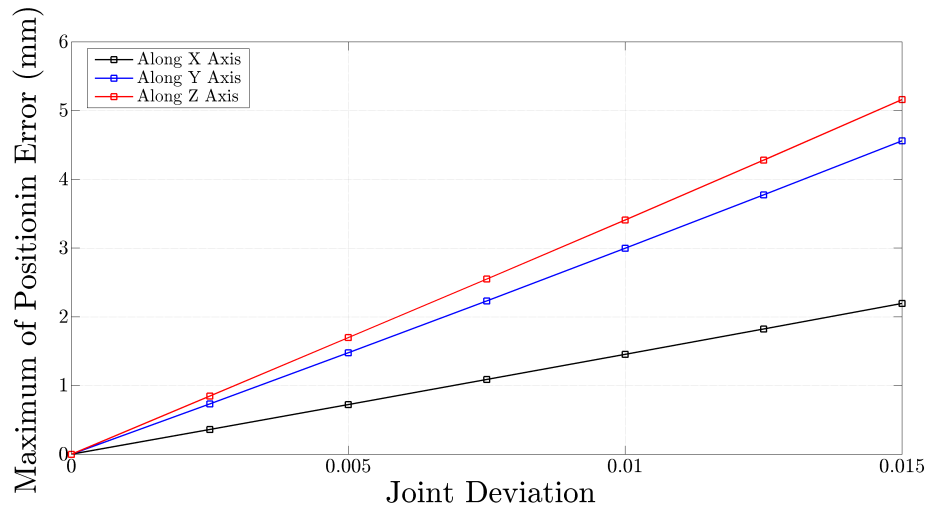


Figure 6.14: Maximum possible positioning error caused by the joint deviations.

how the translational motion along their axes can accommodate joint misalignment without locking the mechanism.

## 6.6 Conclusion

A model of the robot in the SimMechanics simulation environment (Matlab R2012b, The MathWorks Inc.) was developed. The simulation model and the analytical solutions for the robot kinematics (Chapter 55) were mutually validated. In addition, the simulation model provides a reliable virtual environment to assess the robot's performance. In this regard, the effect of mechanical imperfections such as actuation backlash and possible machining errors were studied. Although dynamic analysis of the robot is not required due to the negligible effect of inertial forces, the developed simulation model is capable of performing dynamic analysis as well. The simulation environment can always be used to perform and modify specific experiments such as motion planing prior to implementation on the actual robot.

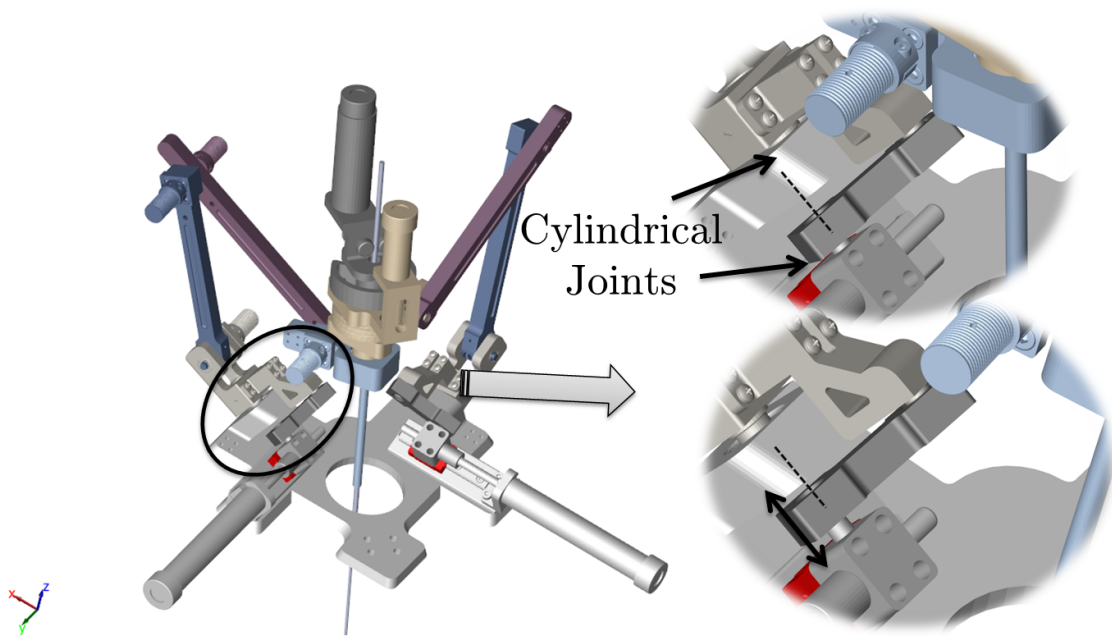


Figure 6.15: Cylindrical joints that prevent the mechanism from locking due to possible mechanical imperfections.

# Chapter 7

## Evaluation of the Final Prototype

### 7.1 Introduction

This chapter describes the final constructed prototype of the robot and outline some of its main features. A number of experiments are used to evaluate the robot's performance and the results are presented in detail. In addition, a graphical user interface, which has been developed to control the actuators and also capture the signals from the integrated force sensor, is introduced.

### 7.2 Overview of the Final Prototype

Figure 7.17.1 presents the final prototype of the parallel robot. As can be seen, the robot has a compact design to provide the degrees of freedom required to orient and position a surgical needle.

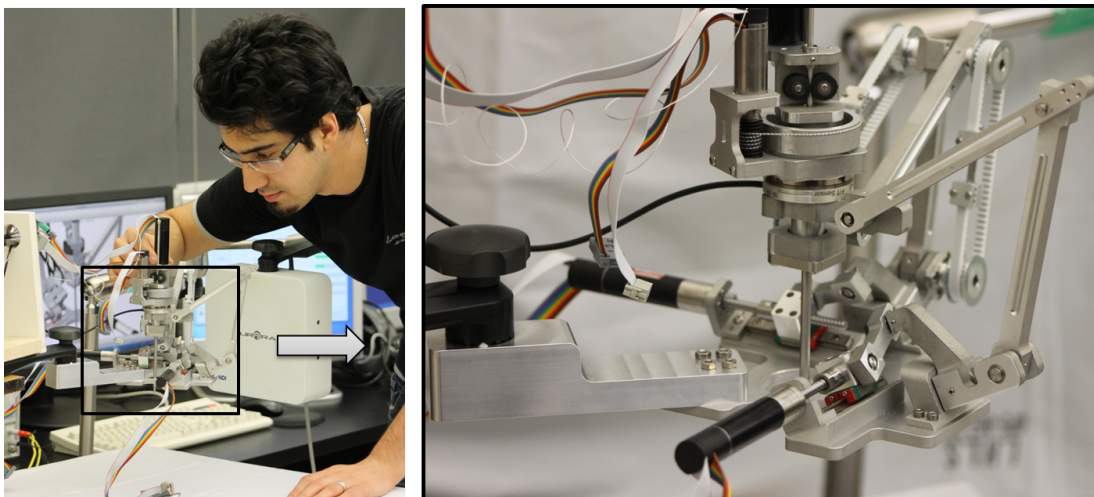


Figure 7.1: The final prototype of the robot.

The parallel structure allows more actuators to be located near the base of the robot. As can be seen in Figure 7.27.2, the Pitch and Yaw DOFs are actuated by two linear spindle

drives located at the stationary base of the robot. As was explained previously, the main leg of the robot provides the RCM, while the ancillary leg forms the parallel structure and enables the mechanism to be actuated by the two crank–slider mechanisms that are located on the stationary base. Figure 7.37.3 shows the main and the ancillary legs of the robot. As can be seen in Figure 7.37.3, the main leg is equipped with two motion constraints (i.e., timing belts and pulleys) to provide the RCM at the desired location.

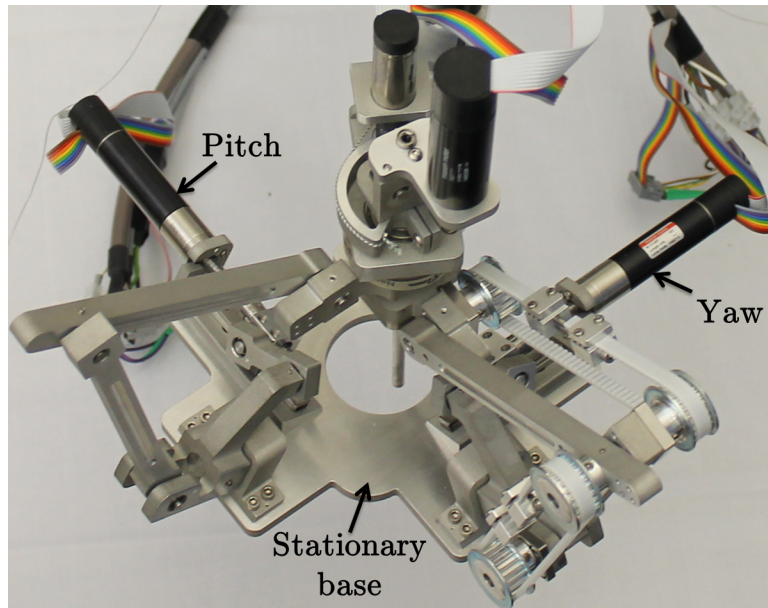


Figure 7.2: The pitch and Yaw DOFs.

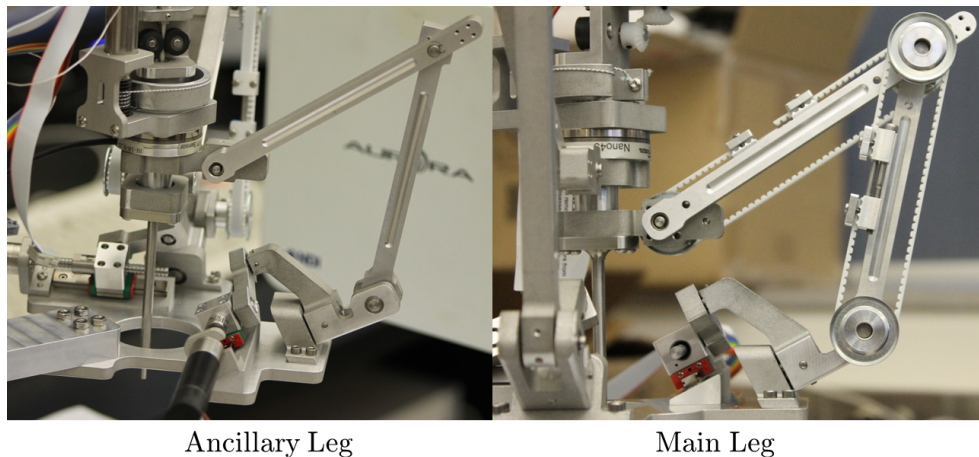


Figure 7.3: The main and ancillary legs of the robot's mechanism.

The timing belts and pulleys (6 mm AT3, BRECOflex Co.) were chosen to have a minimal backlash to ensure that rotational motion is properly transferred from one link of the main leg to another. In addition, each of the belts must have sufficient tension to ensure smooth and consistent motion transfer. Since the axes of the pulleys are fixed and it is not possible to gain

the required tension by moving the pulleys, a compact tensioning mechanism was designed to provide a tunable amount of tension in each of the timing belts. Figure 7.47.4 depicts the details of the tensioning mechanism. As can be seen, the two ends of the belt are clamped between the two metal parts i.e., jaws, and the distance between the two ends of the belts can be tuned using a screw. There is also a guiding pin to provide a prismatic joint for translational motion of the two ends of the belt.

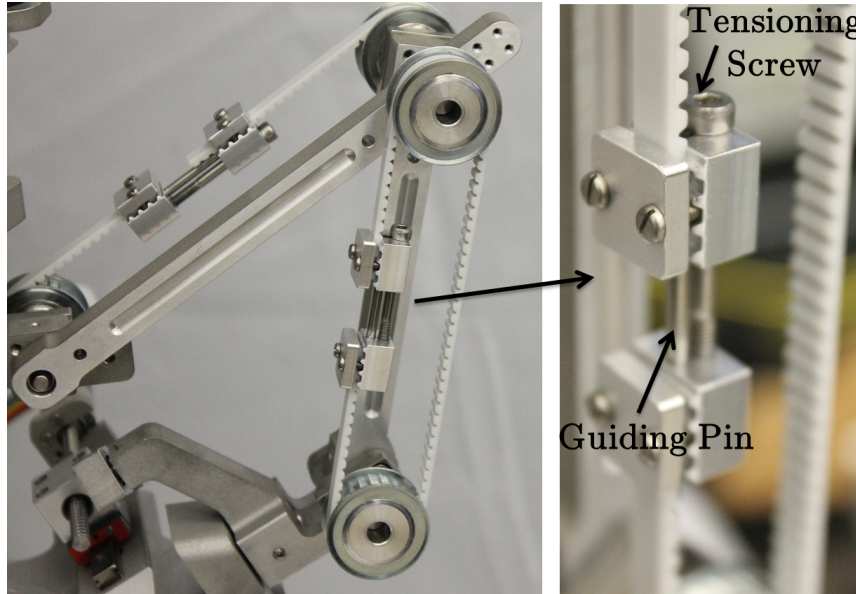


Figure 7.4: The belt tensioning mechanism.

As explained in Chapter 44, a crank–slider mechanism was designed to provide a compact actuation mechanism for the Pitch and Yaw DOFs. Figure 7.57.5 shows the details of the crank–slider mechanism in both the final prototype and CAD model of the robot. A small DC motor actuates the translational motion (i.e., sliding) along the ball screw axis. The sliding motion of the crank–slider mechanisms determines the orientation of the cranks which are connected to the legs of the parallel mechanism. In this way, a compact, high resolution actuation system is provided for the Pitch and Yaw DOFs.

The two legs of the robot are connected together to form the parallel structure. Figure 7.67.6 shows the details of the connection between the two legs. As explained in Chapter 44, there is a rotational degree of freedom between the two legs to avoid locking the mechanism’s movement. As can be seen in Figure 7.67.6, a hollow force sensor (Nano43 6 DOF force/torque sensor, ATI Industrial Automation) is attached at the top of the legs to measure the interaction forces between the surgical needle and tissue.

Roll and insertion are the other two decoupled degrees of freedom that are actuated using small DC brushless motors (Maxon Motor, EC-max 16 and EC 22, respectively). Figure 7.77.7 shows the actuation of these two degrees of freedom in the final prototype of the robot. The linear insertion of the needle is actuated by a friction-based mechanism. As shown in Figure 7.77.7, the needle adapter is pressed between two plastic rollers and one of the rollers is actuated using two bevel gears and a small DC motor. There is also a small linear bearing to ensure that the needle adaptor, and in turn, the surgical needle are aligned at the centre of the trocar.

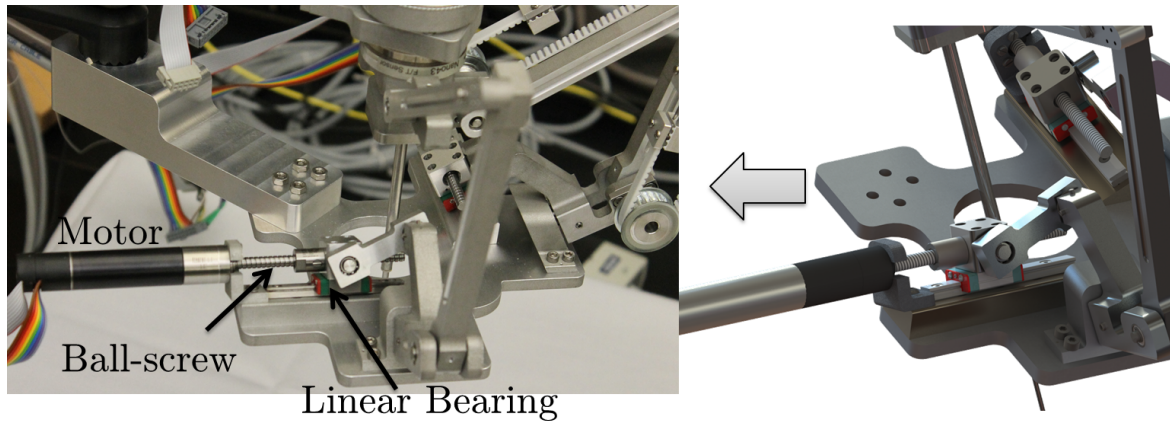


Figure 7.5: The crank–slider mechanism.

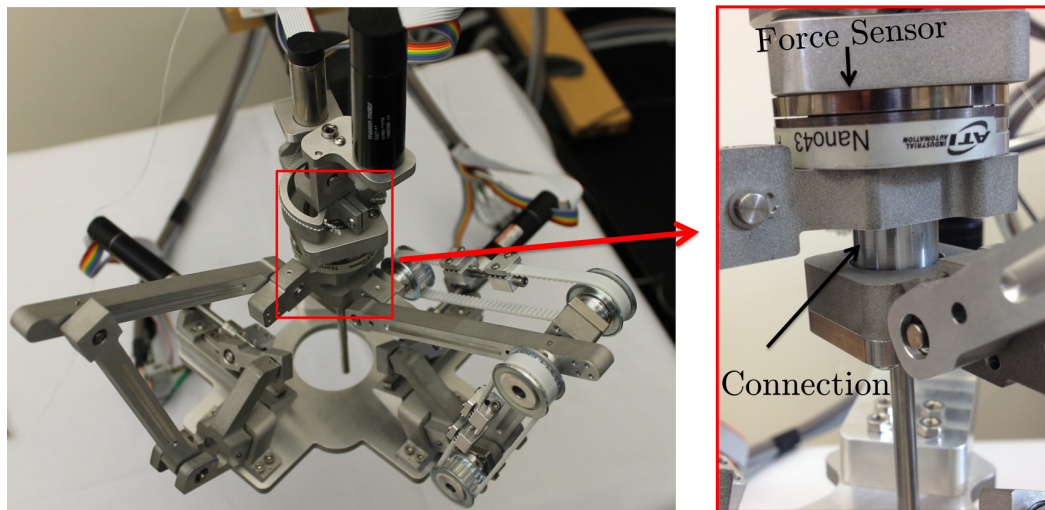


Figure 7.6: The connection between two legs of the mechanism.

On the other hand, the Roll motion is actuated using a cable-driven mechanism and a small DC motor. As a result, the actuation of both the Roll and Insertion motions are considered to be zero backlash.

Figure 7.87.8 shows the robot above an artificial model of deflated lungs. As can be seen, the surgical needle can be oriented using the two linear spindles and then be inserted into the lung through the body of the mechanism, hollow force sensor and interface tube.

The main components of the robot mechanism are introduced in Figures 7.97.9 to 7.117.11. Figure 7.97.9 shows the base of the robot and the axes of the Pitch and Yaw motions. As can be seen, the axes are inclined to move the RCM downward. There are two bearings placed back to back to support the Pitch and Yaw motions and each bearing housing is connected to the base using a combination of two pins and two bolts to achieve perfect alignment.

Figure 7.107.10 shows the linkages that form the legs of the robot and also connect the robot end-effector to the stationary base. Rotational motion between the linkages (i.e., the revolute joints) are provided using two adjoining bearings to properly support the applied loads.

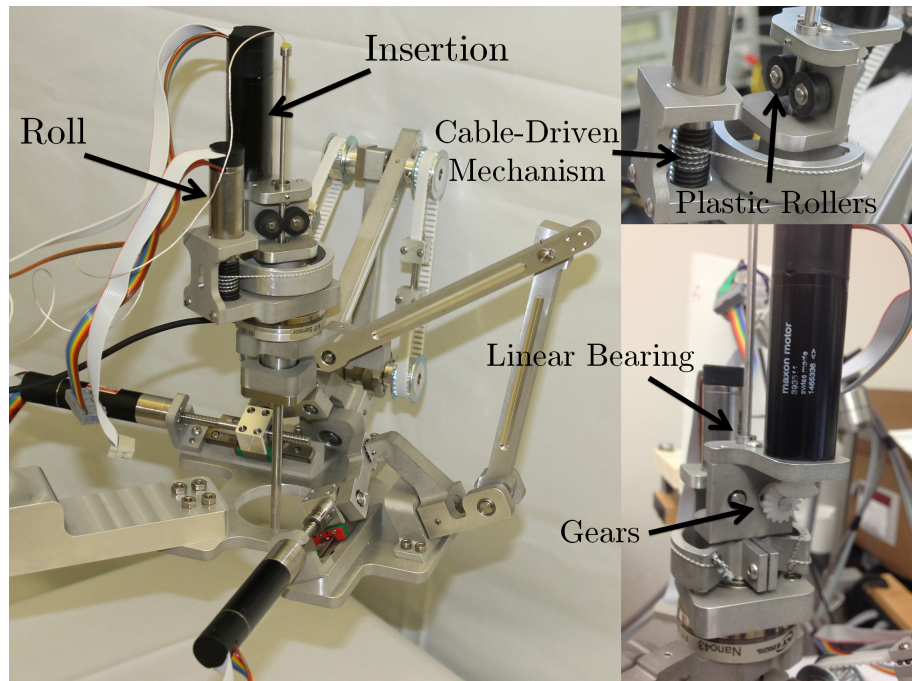


Figure 7.7: The Roll and linear insertion degrees of freedom.

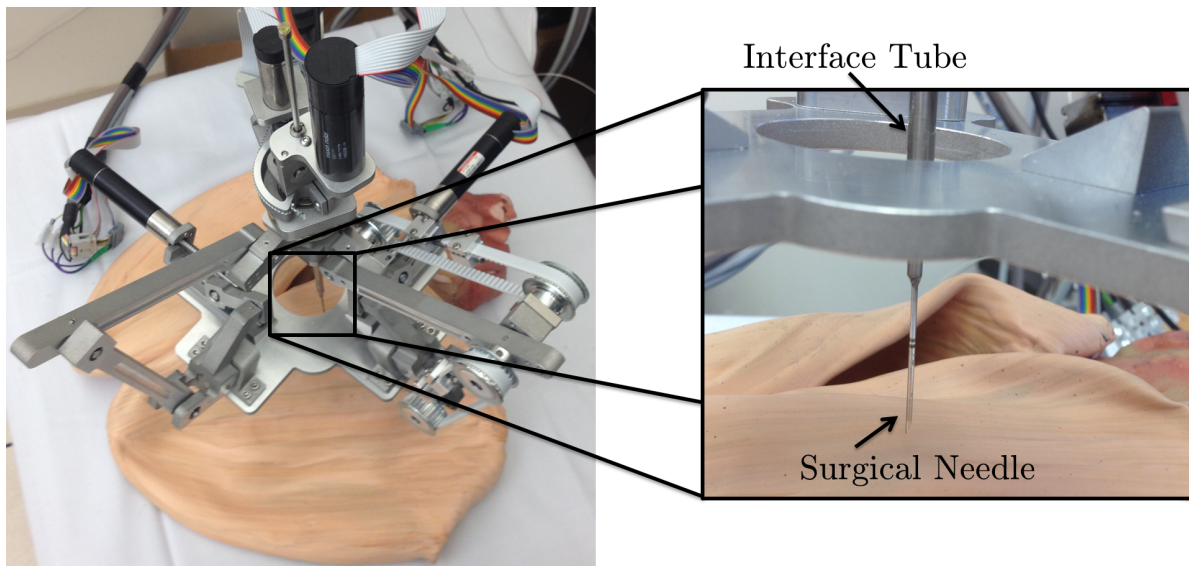


Figure 7.8: The surgical needle supported by the robotic manipulator.

Figure 7.117.11 illustrates how the two legs of the robot are connected to each other. There are two strong bearings on each side to provide the required rotation between the two legs, thereby preventing the mechanism from locking.

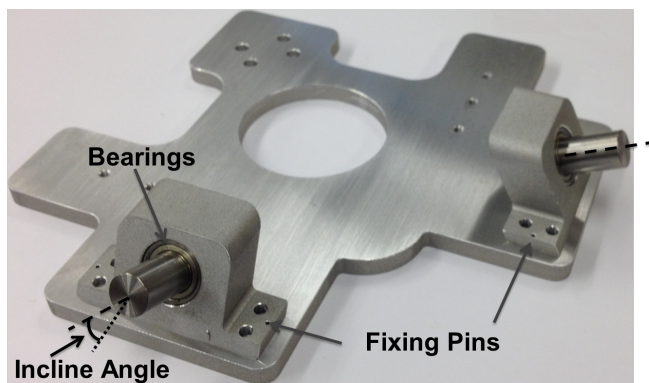


Figure 7.9: The stationary based of the robot.

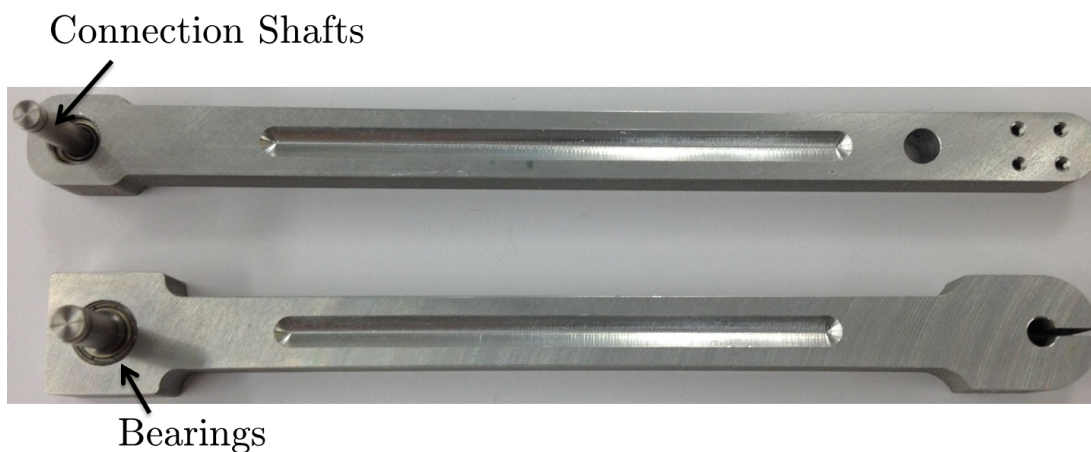


Figure 7.10: The linkage of the robot's legs.

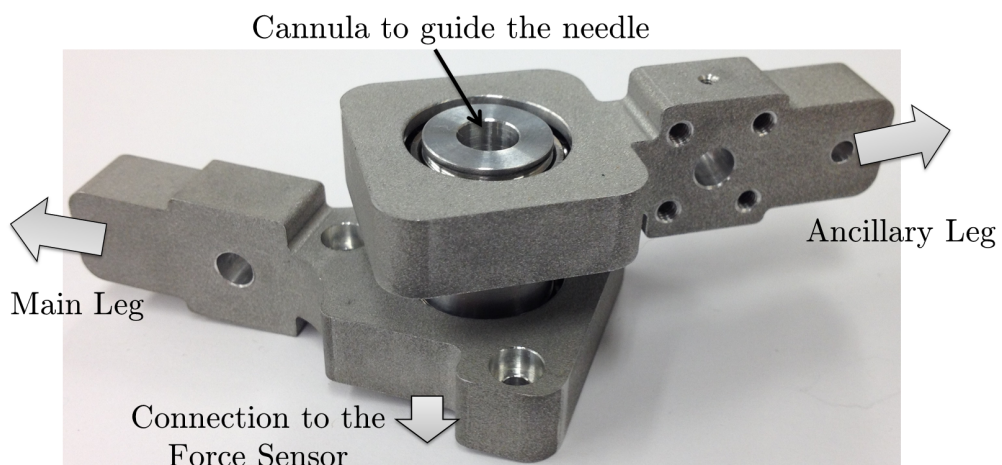


Figure 7.11: The connection between the tow legs.



## 7.3 The Graphical User Interface

As discussed in Chapter 44, small-size, brushless DC motors have been chosen to actuate the four DOFs of the robot. All of these servomotors are equipped with a separate controller unit, the EPOS2, also supplied by Maxon. Using these controllers, it is possible to command the motors simultaneously to control movement of the robot. Figure 7.127.12 shows the graphical user interface (GUI) developed for the robotic system in Visual C++ using the Microsoft Foundation Class (MFC). As shown in Figure 7.127.12, the developed interface enables the user to simply control the robot's motion and also monitor and record the forces acting on the surgical needle.

The user interface is divided into a number of sections, according to function. The top buttons of the user interface are used to start communication with the controllers and also apply the related settings and safety considerations, including maximum following errors (related to positioning commands), velocity and acceleration of the motors.

The interface has a tumour targeting section that enables the user to enter the location of the tumour relative to the base coordinate frame of the robot. The inverse kinematics of the robot is then solved to find the required joint motions and the actuators are moved to obtain the orientation required to target the tumour. After achieving the correct orientation, the insertion command can be run to move the needle along the fixed orientation until the targeted tumour is reached. The main feature of the developed GUI is that it has been programmed using a multi-thread approach to ensure that different tasks and actions can be executed simultaneously and in real-time.

The GUI has also two separate sections to solve the forward and inverse kinematics to evaluate the robot's movements before moving the robot towards the desired location. Motion is achieved using interpolated position mode (IPM) of the EPOS2 controllers. The IPM mode gets position, velocity and time intervals (also known as PVT values) for each motor and makes sure that all the motors arrive at the desired positions on time. For example, if the robot end-effector is supposed to follow a certain path during a manoeuvre, this pass is broken into several points. Then, the position and velocity of each point is mapped into joint space using the inverse kinematics and the Jacobian matrix. The IPM mode interpolates between these discrete points for each motor considering the same time intervals for all of them. As a result, all of the actuators move smoothly to generate the desired path of the robot end-effector.

## 7.4 Testing and Validation

In order to effectively evaluate the performance of the robot and assess its capabilities, a series of experiments was conducted. The results of these experiments are reported in this section.

### 7.4.1 Workspace Evaluation

As discussed in Chapter 33, a total range of  $30^\circ$  degrees for the Pitch and Yaw DOFs is expected to provide sufficient workspace for most needle-based procedures. However, the proposed robot is capable of supporting a larger workspace as it provides a total range of  $45^\circ (\pm 22.5^\circ)$

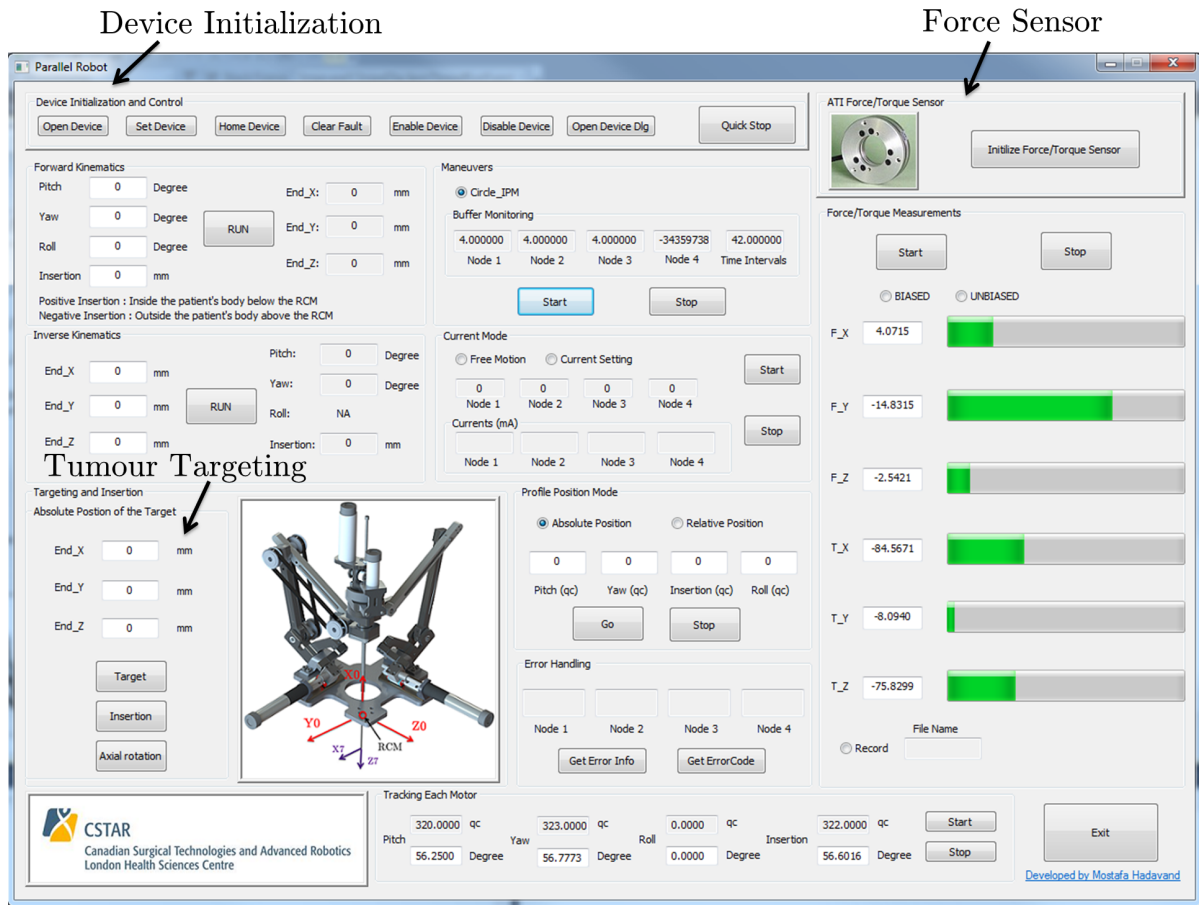


Figure 7.12: Graphical user interface to control the robot and monitor the applied forces.

for the two targeting degrees of freedom (i.e., the Pitch and Yaw). Figure 7.137.13 shows the range of motion for these two degrees of freedom.

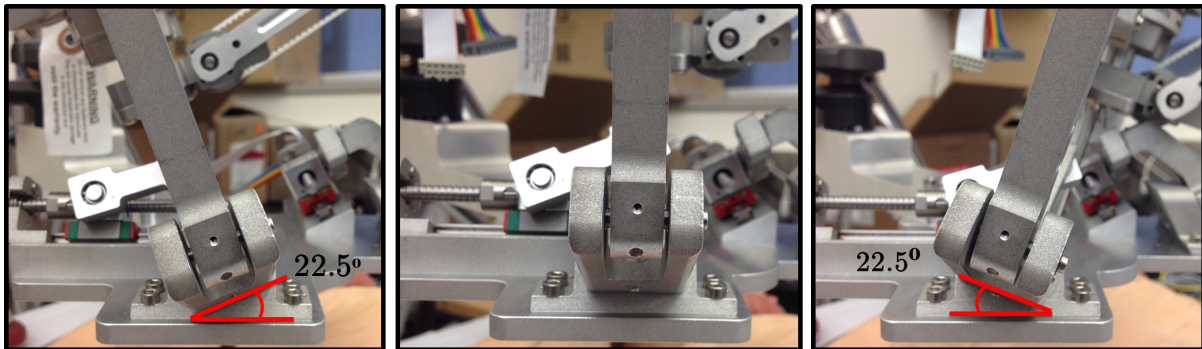


Figure 7.13: Range of motion for the Pitch and Yaw degrees of freedom.

The insertion motion is actuated using two plastic rollers. As a result, the range of motion for the insertion of the needle is not limited and only depends on the length of the needle adaptor. On the other hand, the roll motion has a range of motion of more than 180° which satisfies the application requirements.

### 7.4.2 RCM Assessment

The proposed parallel RCM mechanism is supposed to provide a fixed centre of motion for the surgical needle to minimize the forces acting on the patient's body. In other words, the surgical needle rotates around a fixed point known as the RCM (Remote Centre of Motion). In order to assess the RCM of the robot, the tip of the needle was placed at the RCM, while the needle was moved within its workspace by applying sinusoidal motions to the pitch and yaw DOFs and its motion was tracked by an optical tracking system. The position of the tip of the needle is supposed to remain fixed as the needle is rotating around the RCM. Figure 7.147.14 shows the tracking system and the marker attached to the tip of the needle. The stereo camera used for tracking (S60, Claron Technology Inc.) is reported to have a calibration accuracy of 0.25 mm (RMS) and as can be seen in Figure 7.147.14, it tracks the position of the marker that is attached to the tip of the needle. Figures 7.157.15, 7.167.16 and 7.177.17 show the results of tracking the RCM of the robot by the optical tracking system. The standard deviations of the RCM position along the X, Y and Z axes of the camera are 0.17 mm, 0.31 mm and 0.19 mm, respectively. The results of RCM evaluation show that the mechanism is capable of providing a proper fixed centre of rotation for the surgical needle while it is inserted into the patient's body.

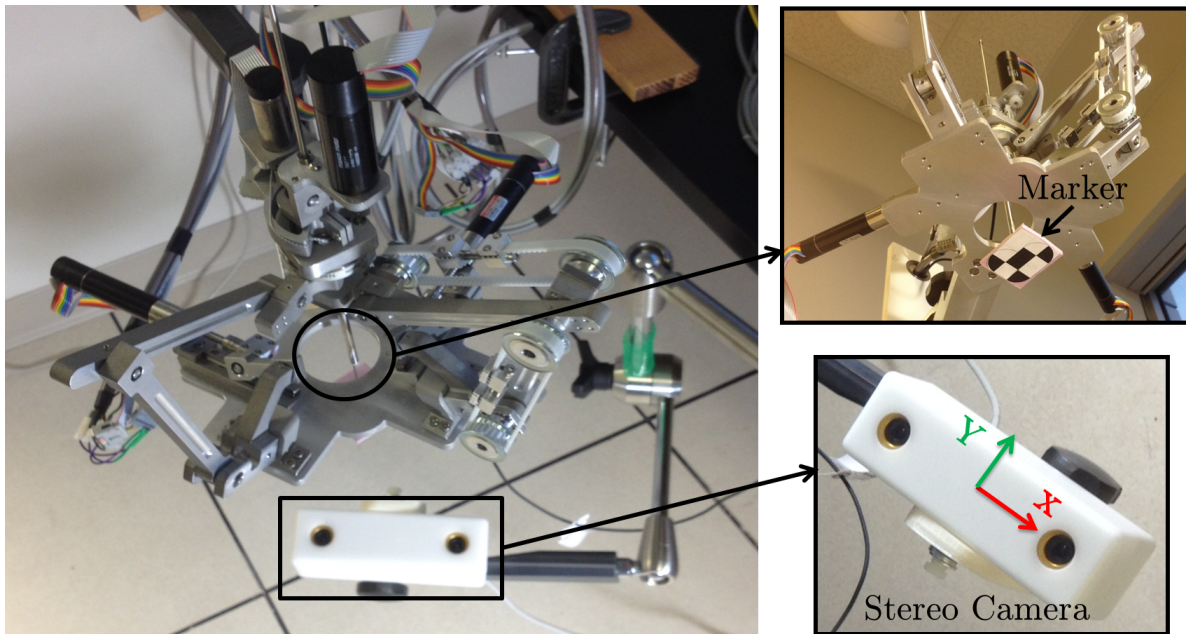


Figure 7.14: Tracking the tip of the needle using the optical tracking system.

### 7.4.3 Path Planning

Tracking a predefined path with the tip of the needle is another experiment performed to evaluate the targeting capabilities of the robot. As can be seen in Figure 7.187.18, a circular path within the YZ plane of the base coordinate frame was generated. Using the robot's inverse kinematics, the joint motions were determined and fed into the corresponding actuators to

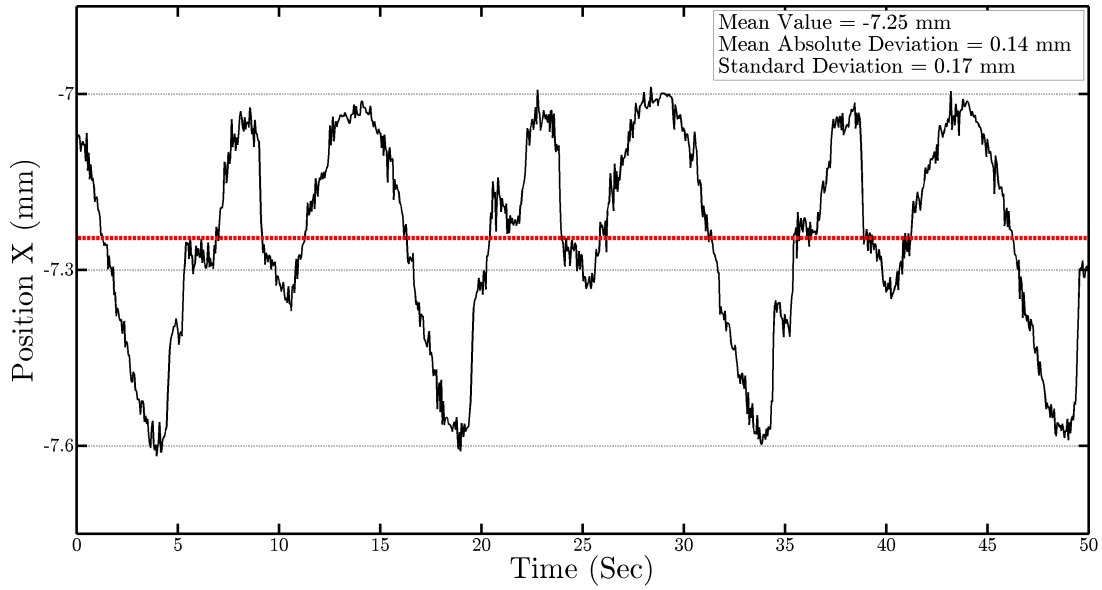


Figure 7.15: Tracking the RCM position along the X axis of the camera.

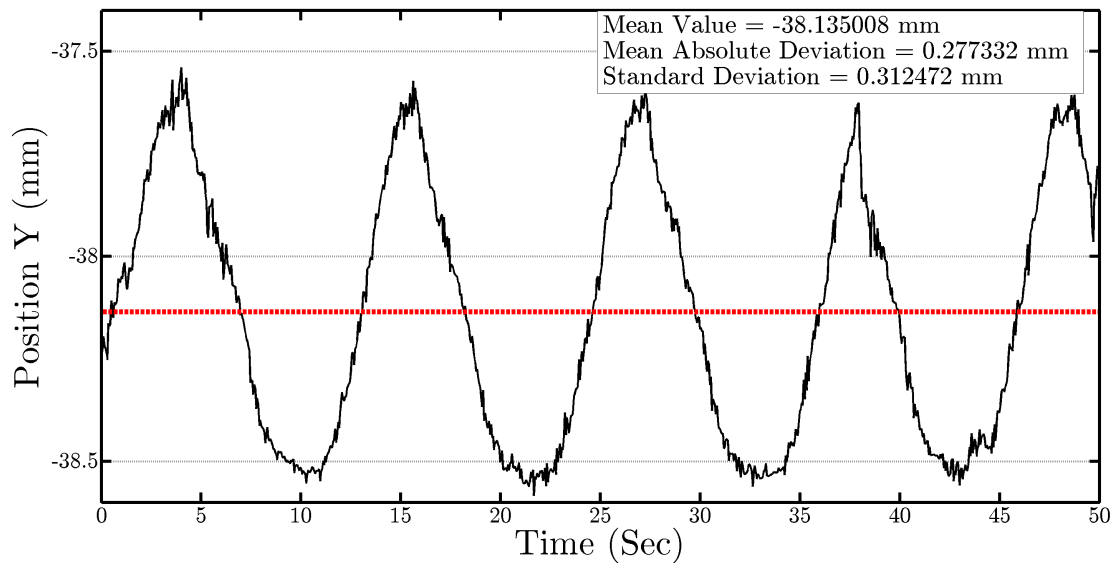


Figure 7.16: Tracking the RCM position along the Y axis of the camera.

move the tip of the needle along the circular path. The tip of the needle was constantly tracked by the stereo camera to assess the accuracy of the robot in tracking the desired path. The circle is located 100 mm beneath the RCM and has a diameter of 20 mm.

The optical tracking system captures the position of the marker attached to the tip of the needle (i.e., tool marker) relative to the coordinate frame of the stereo camera. As a result, the tracked circular path does not necessarily lie within one of the coordinate planes of the camera, so corresponding plane that contains the entire circular path (the YZ plane of the base

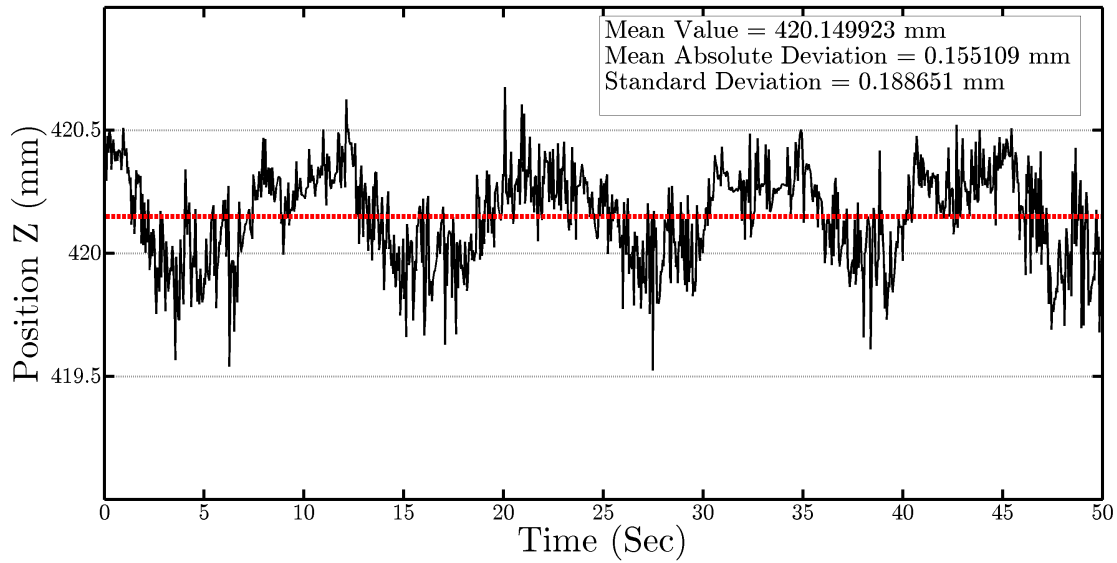


Figure 7.17: Tracking the RCM position along the Z axis of the camera.

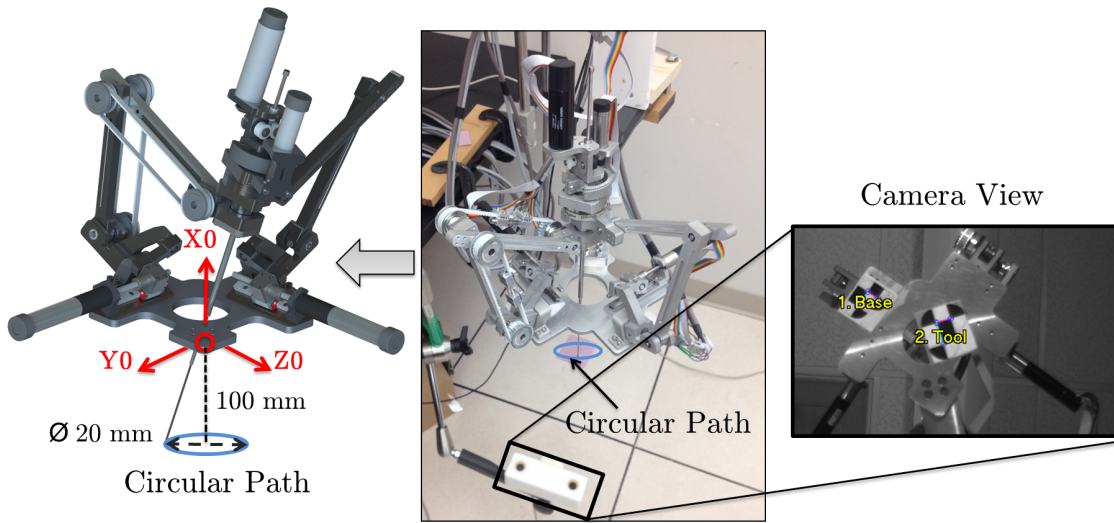


Figure 7.18: Tracking a circular path by the tip of the needle.

coordinate frame of the robot) must be found. The plane is actually the YZ plane of the robot’s base coordinate frame.

To accomplish this, another marker (i.e., base marker) is attached to the stationary base of the robot, as showing in Figure 7.187.18. However, the errors of the rotation matrix between the camera’s coordinate frame and the frame of the base marker doe not let the plane to be found accurately. In order to get around this problem, a plane was fitted into the circular path and the captured position was rotated to that plane. Figure 7.197.19 shows the circular path and its plane within the camera coordinate frame.

Figure 7.207.20 shows the generated circular path and the desired circular path within the YZ plane of the robot’s base coordinate frame (see Figure 7.187.18). The maximum deviation

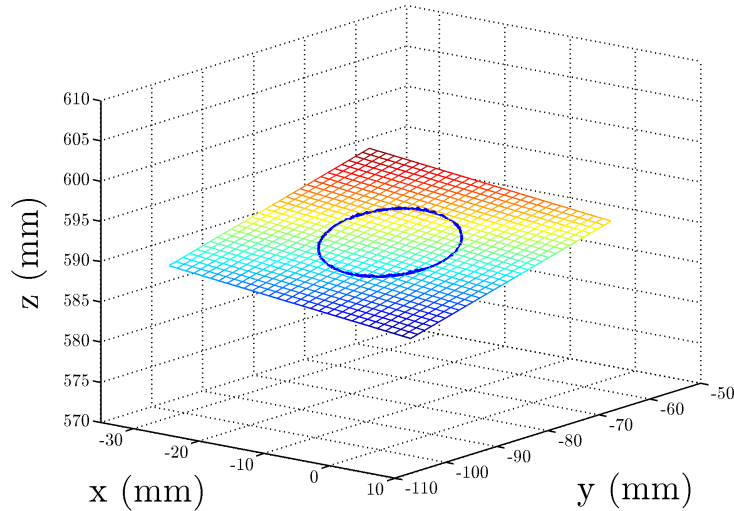


Figure 7.19: The generated circular path by the tip of the needle in camera coordinate frame and its plane.

from the desired path is 1 mm and Figure 7.217.21 depicts the variation of the tracking error along the  $360^\circ$  circular path. The recorded data from the camera consists of several circular paths generated by the tip of the needle to also assess the repeatability of generating the circular path.

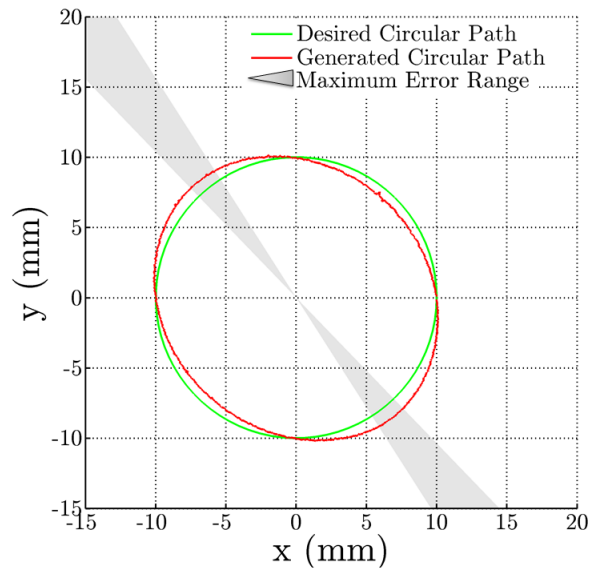


Figure 7.20: The generated circular path and desired one in robot's base coordinate frame.

Path generation was performed using the analytical model of the robot using the calibrated lengths of the linkages. In other words, open-loop position control method was used, without any feedback from the actual position of the end-effector (i.e., tip of the needle). Thus, the tracking error originates from the calibration errors, RCM location and optical tracking. Although the open-loop control of the robot provides the required targeting accuracy for the

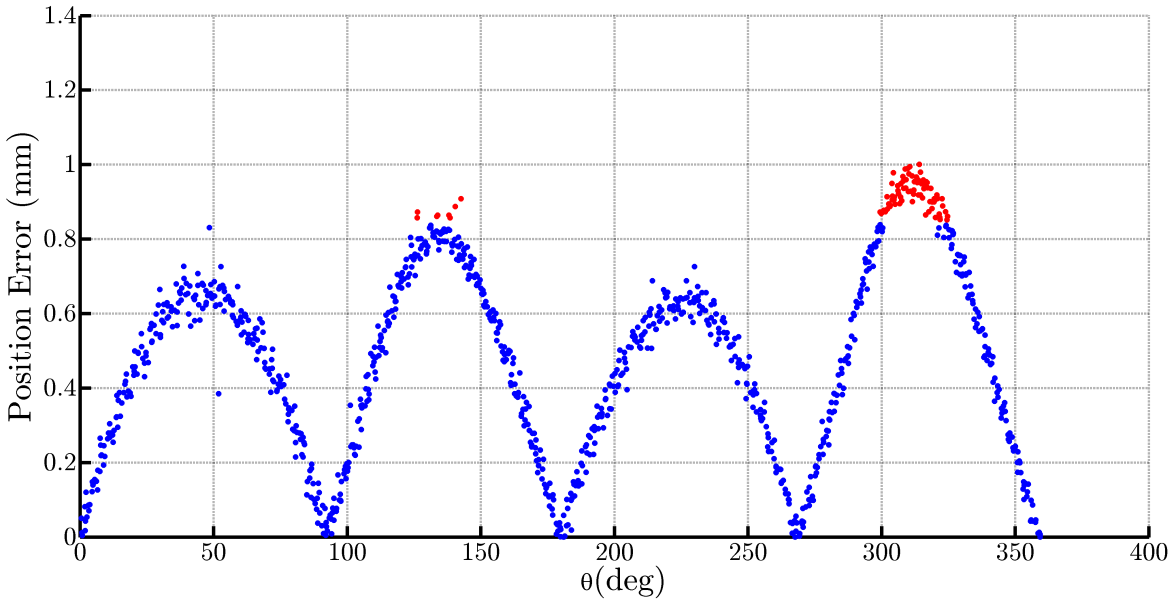


Figure 7.21: Error of tracking the circular path by the tip of the needle.

intended applications, further improvements may be achieved by integrating medical images and using master–slave mode to control the robot. In this regard, the interventionist can control the orientation and position of the surgical needle remotely based on the medical images (i.e., intra-operative ultrasound and CT).

#### 7.4.4 Force Measurements

One of the main features of the proposed robot is that it is capable of measuring the direct interaction forces between the surgical needle and tissue. Although the force sensor is outside of the patient’s body, it does not measure the applied forces/torques acting on the trocar. In a minimally invasive procedure, the applied forces at the trocar from the patient’s body and also the friction between the surgical tool and trocar can cause considerable errors in measuring the interaction forces between the surgical tool and living tissue.

As explained in Chapter 44, the proposed mechanical design makes it possible to separate the needle–tissue interaction forces from applied forces acting at the trocar. Figure 7.227.22 shows an experimental setup developed to measure the interaction forces between a surgical needle and an animal tissue sample. As can be seen in Figure 7.227.22, the robot is attached to a model of human thoracic cavity and the surgical needle is inserted into the cavity through a small trocar (standard 5 mm trocar). A needle insertion experiment is performed on an animal tissue sample (chicken breast) which is placed inside the model of thoracic cavity. The needle was inserted 5 cm inside the tissue and retracted at a speed of 14 mm/sec and the insertion force was recorded by the force sensor. Figure 7.237.23 shows the insertion force applied to the needle during the experiment.

The interaction forces measured between the needle and tissue can be reflected into the surgeon’s hand using a haptic interface. This can help to find the location of the tumour based on the variations in insertion forces applied to the needle, and in turn, to the surgeon’s hand.

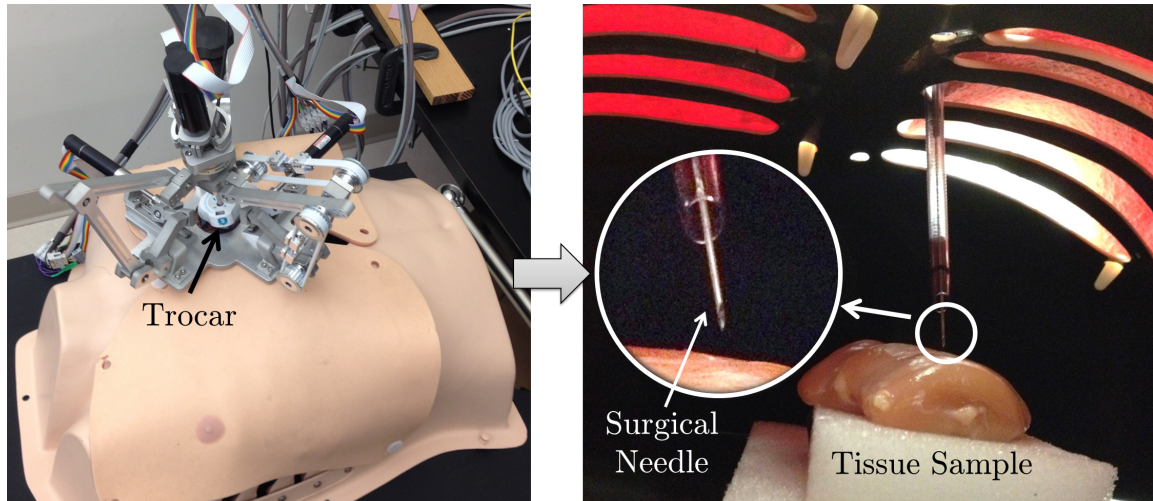


Figure 7.22: Needle insertion into animal tissue using the proposed patient-mounted robot.

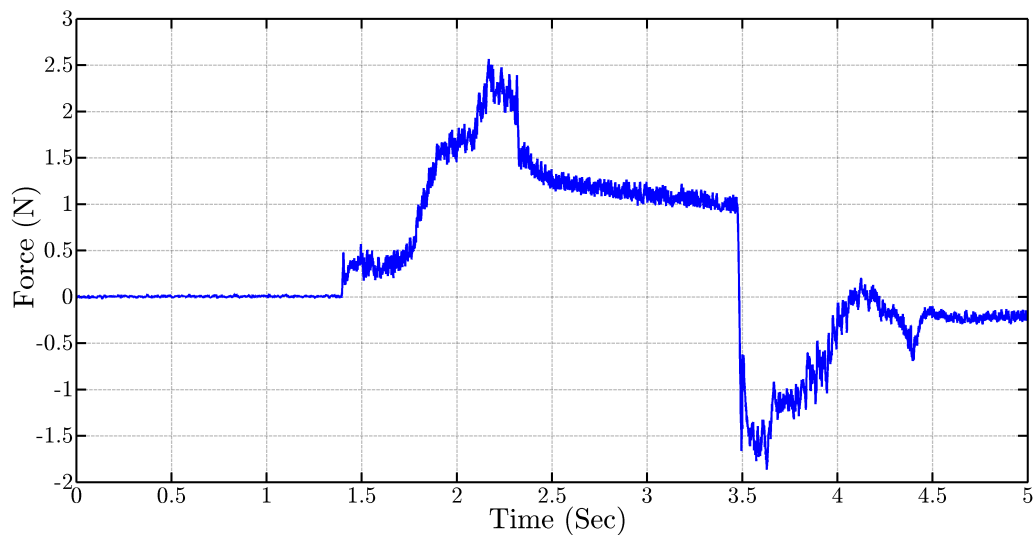


Figure 7.23: Insertion force applied to the surgical needle during the experiment.

This experiment demonstrates that the robot is capable of measuring the direct interaction forces acting of the surgical needle during an intervention. However, further experiments are required to assess the accuracy of force measurement.

## 7.5 Conclusion

It was shown that the workspace of the robot is a cone of  $\pm 22.5^\circ$  which is more than the design requirement mentioned in Chapter 33. It was also shown that the proposed patient-mounted, parallel mechanism provides a fixed RCM at a desired location beneath the skin level. This is the main feature of the proposed design that makes it distinctive among existing RCM mechanisms. In addition, the positioning accuracy of the robot in open-loop control was



assessed by performing a path planning test. Finally, an experimental setup was developed to evaluate force measurement during a simple needle insertion task into an animal tissue sample.

# Chapter 8

## Conclusions

### 8.1 Summary

This thesis describes the design and development of a compact, patient-mounted surgical robotic manipulator for minimally invasive lung cancer diagnosis and treatment. It is intended to support available needle-based interventions including needle biopsy, ablation and high-dose-rate brachytherapy. To do so, the robot's mechanism has a modular design to support different sizes of surgical needles. Accurate positioning of the tip of the surgical needle plays a key roll in the overall success of needle-based interventions. Movements of the patient relative to the robot, which can be caused by physiological motions (i.e., breathing) or repositioning the patient inside/outside a medical imaging scanner, may introduce considerable errors in needle positioning. A simple, effective approach to address this issue is to attach the robot into the patient's body. For this purpose, the robot has a compact design that may be affixed to the patient's body using either straps or double-sided tapes. The light weight of the robot (i.e., around 1.6 kg), allows it to be passively supported while it is attached into the patient's body.

The proposed robot is designed to perform minimally invasive interventions during which a surgical needle may go through a trocar to pass the skin and reach the tissue. For that purpose a Remote Centre of Motion is required to avoid hurting the patient while orienting the needle. A novel parallel RCM mechanism was designed to provide four decoupled degrees of freedom to orient and position a surgical needle within a spherical coordinate system. A comprehensive review of the relevant literature indicates that no such RCM mechanism has been developed before. Apart from the parallel structure, moving the RCM downward to minimize the applied forces into the patient's body, while keeping the required workspace is another major advantage of the proposed mechanism over existing ones.

### 8.2 Concluding Remarks

During this research work, a robotic manipulator with an original design was developed for the effective delivery of needle-based interventions for cancer diagnosis and treatment. This robotic system was developed from ground up and provides a solid basis for future work with the ultimate goal of improving cancer diagnosis and treatment. The robot has three significant features:

### **Compact, Patient-Mounted Design**

The robot consists of a compact design that is capable of being attached to the patient's body to reduce errors that may be caused by the movements of the patient during the surgical intervention. Physiological movements such as breathing and repositioning of the patient during the intervention are the main sources of such errors that may degrade the overall targeting accuracy of a robotic manipulator. Fixing the robot into the patient's body is a simple effective approach to get around such sources of error. The proposed robot is compact enough to be mounted on a patient's body and also fit inside a typical medical imaging scanner bore.

### **Novel Parallel RCM Mechanism**

An original parallel RCM mechanism was developed to hold a surgical needle and orient it around a fixed point. The parallel structure allows two actuators to be placed at the stationary base of the robot to reduce the floating inertia. The improper location (i.e., at or above the skin surface, rather than subcutaneous) of the RCM is one of the main problems associated with the existing patient-mounted robotic systems that have a fixed RCM. In the proposed design, the RCM is moved downward to minimize the forces that act on the patient's body, while providing the required workspace for the surgical needle. Compact and efficient actuation for each degree of freedom is another feature of the robot.

### **Measurement of Needle–Tissue Interaction**

The specific design of the robot along with the proper integration of a hollow force sensor (ATI Industrial Automation) makes it possible to measure the interaction forces between the surgical needle and tissue. The reason is that during a minimally invasive intervention, the Pitch and Yaw DOFs orient the trocar towards target, while the needle is inserted through the force sensor, the body of the mechanism and the trocar using another decoupled degree of freedom (insertion). The force measurement can be used to provide force reflection to the surgeon during the intervention. The force reflection may be helpful to properly guide the needle towards the target (i.e., a tumour) and also to confirm its location within the tissue.

## **8.3 Recommendations and Future Work**

During the course of this work, a prototype of a surgical robot for needle-based interventions was designed and constructed. Preliminary validations were conducted on the robot and the capabilities of the proposed robot were assessed. However, further experiments and trials are required to fully evaluate the robot's performance. Possible future work and recommendations are discussed in three categories: mechanical, control and navigation of the surgical needle and testing and validation.

### **8.3.1 Mechanical Recommendations**

The evaluations of the robot have shown that the mechanical design satisfies the desired requirements. However, some improvements in the mechanical design and the construction pro-

cess may improve the overall performance of the proposed robotic manipulator. First, the robot's structure can be further reinforced as the overall weight of the robot can be supported with a passive spring-based mechanism. The main improvement is related to the bearings that provide the rotational motions at the joints. The use of bigger and stronger bearings is possible without any need to increase the size of the robot. These would provide better alignment of the two legs of the robot and the location of the RCM and improve the structural stiffness of the robot.

The timing belts and pulleys accompanied by the tensioning mechanism has been proven to be effective to transfer rotational motion from one link to another and ultimately provide the RCM. For each motion transfer, there is one timing belt placed at one side of the main leg and applying tension in the timing belts may cause slight deflection in the linkages. Having two timing belts for each motion transfer, located on each side of the main leg can avoid such deflections and improve the robustness of the robotic manipulator. In addition, it is recommended that the linear insertion actuation be improved by selecting better material for the plastic rollers and also using better linear bearings to minimize the amount of friction applied to the needle. As a result, the interaction forces between the tissue and surgical needle can be measured more accurately.

Improving the machining precision is another mechanical recommendation for future prototypes of the proposed mechanism. It is also recommended to develop more needle adaptors for different sizes of surgical needles to support all of the possible needle-based interventions for cancer diagnosis and treatment.

During the course of this research work, a passive mechanism that attaches to the operating table to support the weight of the robot was designed. It is strongly recommended to develop such a mechanism to passively suspend the robot above the patient's body while it is attached to the patient. Finally, registration of the robot into medical images (i.e., CT images) is required to track the tip of the needle while it is inside the patient's body.

### 8.3.2 Control Recommendations

Currently, the robot's motion is controlled by considering the kinematics of the robot and using the servo motor controllers for each degree of freedom. This means that control of the position/orientation of the needle is open loop since there is no feedback from the position of the needle. It is recommended that Master-Slave control be implemented so the robot can be controlled by a surgeon using an interface (i.e. master console) while the location of the needle in medical images is provided for the surgeon. Thus, the needle is simply guided by the surgeon towards the target with direct feedback from the medical images (i.e., CT or ultrasound images). The proposed robot is capable of measuring the pure interaction forces between the needle and tissues, so the force measurement can be used to provide a haptic feedback for the surgeon. Thus, by integrating a commercially-available haptic interface into the robot control system, the surgeon can sense the interaction forces between the needle and the tissue during the intervention. This information can be helpful to confirm the location of a tumour within living tissue.

### **8.3.3 Testing and Validation Recommendations**

Several tests should be done to assess the performance of the robot in a operation room condition. Developing a model of thoracic cavity and artificial tissue samples is recommended to provide an experimental environment to run the required experiments to fully evaluate the robot's performance and identify areas for improvement. The next step is clinical assessment during which several animal trials need to be arranged to study the overall function of the proposed robotic manipulator during a clinical application. These experiments and validations are expected to provide valuable information regarding the strong and weak points of the proposed robotic manipulator.



## Appendix A

### Kinematics Equations

#### Forward Kinematics

$${}^0_7T(1,1) = \sin(\phi + \theta_2)\sin(\alpha)\cos(\theta_3) - \cos(\alpha)\sin(\theta_1)\sin(\theta_3) + \cos(\phi + \theta_2)\cos(\alpha)\cos(\theta_1)\cos(\theta_3)$$

$${}^0_7T(1,2) = -\sin(\phi + \theta_2)\sin(\alpha)\sin(\theta_3) - \cos(\alpha)\cos(\theta_3)\sin(\theta_1) - \cos(\phi + \theta_2)\cos(\alpha)\cos(\theta_1)\sin(\theta_3)$$

$${}^0_7T(1,3) = \cos(\phi + \theta_2)\sin(\alpha) - \sin(\phi + \theta_2)\cos(\alpha)\cos(\theta_1)$$

$${}^0_7T(1,4) = L_2\sin(\alpha) - P\sin(\alpha) + d\cos(\phi + \theta_2)\sin(\alpha) - L_1\sin(\alpha)\cos(\theta_2) - d\sin(\phi + \theta_2)\cos(\alpha)\cos(\theta_1) \\ + L_1\sin(\phi + \theta_2)\sin(\alpha)\sin(\phi) + L_1\cos(\alpha)\cos(\theta_1)\sin(\theta_2) + L_1\cos(\phi + \theta_2)\cos(\alpha)\cos(\theta_1)\sin(\phi)$$

$${}^0_7T(2,1) = \sin(\alpha)\sin(\theta_1)\sin(\theta_3) + \sin(\phi + \theta_2)\cos(\alpha)\cos(\theta_3) - \cos(\phi + \theta_2)\sin(\alpha)\cos(\theta_1)\cos(\theta_3)$$

$${}^0_7T(2,2) = \sin(\alpha)\cos(\theta_3)\sin(\theta_1) - \sin(\phi + \theta_2)\cos(\alpha)\sin(\theta_3) + \cos(\phi + \theta_2)\sin(\alpha)\cos(\theta_1)\sin(\theta_3)$$

$${}^0_7T(2,3) = \cos(\phi + \theta_2)\cos(\alpha) + \sin(\phi + \theta_2)\sin(\alpha)\cos(\theta_1)$$

$${}^0_7T(2,4) = L_2\cos(\alpha) - P\cos(\alpha) + d\cos(\phi + \theta_2)\cos(\alpha) - L_1\cos(\alpha)\cos(\theta_2) + L_1\sin(\phi + \theta_2)\cos(\alpha) * \sin(\phi) \\ + d\sin(\phi + \theta_2)\sin(\alpha)\cos(\theta_1) - L_1\sin(\alpha)\cos(\theta_1)\sin(\theta_2) - L_1\cos(\phi + \theta_2)\sin(\alpha)\cos(\theta_1)\sin(\phi)$$

$${}^0_7T(3,1) = -\cos(\theta_1)\sin(\theta_3) - \cos(\phi + \theta_2)\cos(\theta_3)\sin(\theta_1)$$

$${}^0_7T(3,2) = \cos(\phi + \theta_2)\sin(\theta_1)\sin(\theta_3) - \cos(\theta_1)\cos(\theta_3)$$

$${}^0_7T(3,3) = \sin(\phi + \theta_2)\sin(\theta_1)$$

$${}^0_7T(3,4) = \frac{-1}{2}(\sin(\theta_1)(L_1 * \sin(\theta_2) - 2d\sin(\phi + \theta_2) + L_1\sin(2\phi + \theta_2)))$$

$${}^0_7T(4,1) = 0$$

$${}^0_7T(4,2) = 0$$

$${}^0_7T(4,3) = 0$$

$${}^0_7T(4,4) = 1$$

## U and V functions

$$\begin{aligned} U = & -(\sin(\theta'_1)(\cos(\alpha) + 2\cos^2(0.5\theta_1)\cos^3(\alpha) - 2\cos^3(\alpha)) - \sin(\alpha)(\cos(\theta'_1)(2\cos(\alpha) \\ & - 2\cos^2(0.5\theta_1)\cos(\alpha)) - 2\cos(0.5\theta_1)\sin(0.5\theta_1)\cos(\alpha)\sin(\theta'_1)))/(\cos^2(\theta_1)\cos^2(\theta'_1) \\ & + \cos^2(\alpha)\cos^2(\theta_1)\sin^2(\theta'_1) + \cos^2(\alpha)\cos^2(\theta'_1)\sin^2(\theta_1) + \sin^4(\alpha)\sin^2(\theta_1) \\ & \sin^2(\theta'_1) + 2\cos^2(\alpha)\sin^2(\alpha)\sin^2(\theta_1)\sin^2(\theta'_1) + 2\sin^2(\alpha)\cos(\theta_1) \\ & \cos(\theta'_1)\sin(\theta_1)\sin(\theta'_1) + 2\cos^2(\alpha)\sin(\alpha)\cos(\theta_1)\sin(\theta_1)\sin^2(\theta'_1) \\ & - 2\cos^2(\alpha)\sin(\alpha)\cos(\theta'_1)\sin^2(\theta_1)\sin(\theta'_1)) \end{aligned}$$

$$\begin{aligned} V = & -(\sin(\theta'_1)(\sin(\alpha)(\cos^2(\alpha) - \cos^2(\alpha) * \cos(\theta_1)) - 2\cos(0.5\theta_1)\sin(0.5\theta_1) + 2\cos(0.5\theta_1) \\ & \sin(0.5\theta_1)\cos^2(\alpha)) - \cos(\theta'_1)(\cos(\theta_1) + \cos^2(\alpha) - \cos^2(\alpha)\cos(\theta_1)))/(\cos^2(\theta_1) \\ & \cos(\theta'_1)^2 + \cos^2(\alpha)\cos^2(\theta_1)\sin^2(\theta'_1) + \cos^2(\alpha)\cos^2(\theta'_1)\sin^2(\theta_1) \\ & + \sin^4(\alpha)\sin^2(\theta_1)\sin(\theta'_1)^2 + 2\cos^2(\alpha)\sin^2(\alpha)\sin^2(\theta_1)\sin^2(\theta'_1) \\ & + 2\sin^2(\alpha)\cos(\theta_1)\cos(\theta'_1)\sin(\theta_1)\sin(\theta'_1) + 2\cos^2(\alpha)\sin(\alpha) \\ & \cos(\theta_1)\sin(\theta_1)\sin(\theta'_1)^2 - 2\cos^2(\alpha)\sin(\alpha)\cos(\theta'_1)\sin^2(\theta_1)\sin(\theta'_1)) \end{aligned}$$



# Bibliography

- [1] O. Lababede, M. A. Meziane, and T. W. Rice, “TNM staging of lung cancer—A quick reference chart,” *CHEST Journal*, vol. 115, no. 1, pp. 233–235, 1999.
- [2] The Ohio State University, Comprehensive Cancer Center, “About Small Cell Lung Cancer,” August 2013. [Online]. Available: <http://cancer.osu.edu/>
- [3] A. Häcker, S. Vallo, C. Weiss, R. Grobholz, P. Alken, T. Knoll, and M. S. Michel, “Minimally invasive treatment of renal cell carcinoma: comparison of 4 different monopolar radiofrequency devices,” *European Urology*, vol. 48, no. 4, pp. 584–592, 2005.
- [4] Y. S. Kwoh, J. Hou, E. A. Jonckheere, and S. Hayati, “A robot with improved absolute positioning accuracy for CT guided stereotactic brain surgery,” *IEEE Transactions on Biomedical Engineering*, vol. 35, no. 2, pp. 153–160, 1988.
- [5] D. Stoianovici, J. A. Cadeddu, R. D. Demaree, H. Basile, R. H. Taylor, L. L. Whitcomb, and L. Kavoussi, “A novel mechanical transmission applied to percutaneous renal access,” in *Proceedings of the ASME Dynamic Systems and Control Division*, vol. 61, Dallas, Texas, November 16–21, 1997, pp. 401–406.
- [6] A. Patriciu, D. Stoianovici, L. L. Whitcomb, T. Jarrett, D. Mazilu, A. Stanimir, I. Iordachita, J. Anderson, R. Taylor, and L. R. Kavoussi, “Motion-based robotic instrument targeting under c-arm fluoroscopy,” in *Medical Image Computing and Computer-Assisted Intervention—MICCAI 2000*, Pittsburgh, Pennsylvania, October 11–14, 2000, pp. 988–998.
- [7] S. Xu, G. Fichtinger, R. H. Taylor, F. Banovac, and K. Cleary, “Ct fluoroscopy-guided robotically-assisted lung biopsy,” in *Medical Imaging*. International Society for Optics and Photonics, 2006, pp. 61 411L–61 411L.
- [8] A. Melzer, B. Gutmann, T. Remmele, R. Wolf, A. Lukoscheck, M. Bock, H. Bardenheuer, and H. Fischer, “Innomotion for percutaneous image-guided interventions,” *IEEE Engineering in Medicine and Biology Magazine*, vol. 27, no. 3, pp. 66–73, 2008.
- [9] A. Trejos, A. Lin, M. Pytel, R. Patel, and R. Malthaner, “Robot-assisted minimally invasive lung brachytherapy,” *The International Journal of Medical Robotics and Computer Assisted Surgery*, vol. 3, no. 1, pp. 41–51, 2007.

- [10] H. Bassan, T. Hayes, R. V. Patel, and M. Moallem, "A novel manipulator for 3D ultrasound guided percutaneous needle insertion," in *IEEE International Conference on Robotics and Automation*, Roma, Italy, April 10–14, 2007, pp. 617–622.
- [11] J. Hong, T. Dohi, M. Hashizume, K. Konishi, and N. Hata, "An ultrasound-driven needle-insertion robot for percutaneous cholecystostomy," *Physics in Medicine and Biology*, vol. 49, no. 3, p. 441, 2004.
- [12] B. Maurin, B. Bayle, O. Piccin, J. Gangloff, M. de Mathelin, C. Doignon, P. Zanne, and A. Gangi, "A patient-mounted robotic platform for CT-scan guided procedures," *IEEE Transactions on Biomedical Engineering*, vol. 55, no. 10, pp. 2417–2425, 2008.
- [13] B. Maurin, B. Bayle, J. Gangloff, P. Zanne, M. de Mathelin, and O. Piccin, "A robotized positioning platform guided by computed tomography: Practical issues and evaluation," in *IEEE International Conference on Robotics and Automation (ICRA)*, Orlando, Florida, May 15–19, 2006, pp. 251–256.
- [14] C. J. Walsh, N. C. Hanumara, A. H. Slocum, J.-A. Shepard, and R. Gupta, "A patient-mounted, telerobotic tool for CT-guided percutaneous interventions," *Journal of Medical Devices*, vol. 2, no. 1, pp. 011 007–10, 2008.
- [15] J. J. Craig, *Introduction to Robotics: Mechanics and Control*. Prentice Hall: Englewood Cliffs, NJ, 2004.
- [16] L. B. Rosenberg, "Laparoscopic simulation interface," Apr. 4 2006, US Patent 7,023,423.
- [17] B. Davies, "A review of robotics in surgery," *Proceedings of the Institution of Mechanical Engineers, Part H: Journal of Engineering in Medicine*, vol. 214, no. 1, pp. 129–140, 2000.
- [18] S. Harris, F. Arambula-Cosio, Q. Mei, R. Hibberd, B. Davies, J. Wickham, M. Nathan, and B. Kundu, "The probotan active robot for prostate resection," *Proceedings of the Institution of Mechanical Engineers, Part H: Journal of Engineering in Medicine*, vol. 211, no. 4, pp. 317–325, 1997.
- [19] J.-A. Long, P. Cinquin, J. Troccaz, S. Voros, P. Berkelman, J.-L. Descotes, C. Letoublon, and J.-J. Rambeaud, "Development of miniaturized light endoscope-holder robot for laparoscopic surgery," *Journal of Endourology*, vol. 21, no. 8, pp. 911–914, 2007.
- [20] G. Zong, X. Pei, J. Yu, and S. Bi, "Classification and type synthesis of 1-DOF remote center of motion mechanisms," *Mechanism and Machine Theory*, vol. 43, no. 12, pp. 1585–1595, 2008.
- [21] J. Rosen, J. D. Brown, L. Chang, M. Barreca, M. Sinanan, and B. Hannaford, "The BlueDRAGON—a system for measuring the kinematics and dynamics of minimally invasive surgical tools in-vivo," in *IEEE International Conference on Robotics and Automation Proceedings*, vol. 2, Washington, DC, May 11–15, 2002, pp. 1876–1881.

- [22] B. Davies, S. Starkie, S. J. Harris, E. Agterhuis, V. Paul, and L. M. Auer, "Neurobot: a special-purpose robot for neurosurgery," in *IEEE International Conference on Robotics and Automation*, vol. 4, San Francisco, CA, April 24-28, 2000, pp. 4103–4108.
- [23] J. F. Jensen, "Remote center positioner with channel shaped linkage element," Sept. 1 1998, US Patent 5,800,423.
- [24] A. Faraz and S. Payandeh, "A robotic case study: optimal design for laparoscopic positioning stands," *The International Journal of Robotics Research*, vol. 17, no. 9, pp. 986–995, 1998.
- [25] M. J. Lum, D. C. Friedman, G. Sankaranarayanan, H. King, K. Fodero, R. Leuschke, B. Hannaford, J. Rosen, and M. N. Sinanan, "The raven: design and validation of a telesurgery system," *The International Journal of Robotics Research*, vol. 28, no. 9, pp. 1183–1197, 2009.
- [26] N. Zemiti, G. Morel, T. Ortmaier, and N. Bonnet, "Mechatronic design of a new robot for force control in minimally invasive surgery," *IEEE/ASME Transactions on Mechatronics*, vol. 12, no. 2, pp. 143–153, 2007.
- [27] D. Kim, E. Kobayashi, T. Dohi, and I. Sakuma, "A new, compact mr-compatible surgical manipulator for minimally invasive liver surgery," in *Medical Image Computing and Computer-Assisted Intervention, (MICCAI 2002)*, Tokyo, Japan, September 25-28, 2002, pp. 99–106.
- [28] T. Ortmaier and G. Hirzinger, "Cartesian control issues for minimally invasive robot surgery," in *IEEE/RSJ International Conference on Intelligent Robots and Systems, (IROS 2000)*, vol. 1, Takamatsu, Japan, October 30–November 5, 2000, pp. 565–571.
- [29] G. Tholey, "A teleoperative haptic feedback framework for computer-aided minimally invasive surgery," Ph.D. dissertation, Drexel University, 2007.
- [30] U. Hagn, M. Nickl, S. Jörg, G. Passig, T. Bahls, A. Nothhelfer, F. Hacker, L. Le-Tien, A. Albu-Schäffer, R. Konietschke, *et al.*, "The DLR MIRO: a versatile lightweight robot for surgical applications," *Industrial Robot: An International Journal*, vol. 35, no. 4, pp. 324–336, 2008.
- [31] Canadian Cancer Society's Steering Committee, "Canadian cancer statistics," August 2013. [Online]. Available: <http://www.cancer.ca/>
- [32] T. He, Z. Xue, K. Lu, M. Valdivia y Alvarado, K. K. Wong, W. Xie, and S. T. Wong, "A minimally invasive multimodality image-guided (mimig) system for peripheral lung cancer intervention and diagnosis," *Computerized Medical Imaging and Graphics*, vol. 36, no. 5, pp. 345–355, 2012.
- [33] R. Martínez-Monge, C. Garrán, I. Vivas, and J. M. López-Picazo, "Percutaneous CT-guided 103Pd implantation for the medically inoperable patient with T1N0M0 non-small cell lung cancer: a case report," *Brachytherapy*, vol. 3, no. 3, pp. 179–181, 2004.

- [34] B. Maurin, O. Piccin, B. Bayle, J. Gangloff, M. de Mathelin, L. Soler, and A. Gangi, "A new robotic system for CT-guided percutaneous procedures with haptic feedback," in *Proceedings of the international congress on computer assisted radiology and surgery*, vol. 1268, Chicago, June 23–26, 2004, pp. 515–520.
- [35] N. Abolhassani, R. Patel, and M. Moallem, "Needle insertion into soft tissue: a survey," *Medical Engineering & Physics*, vol. 29, no. 4, pp. 413–431, 2007.
- [36] J. Ricke, P. Wust, G. Wieners, S. Hengst, M. Pech, E. L. Hanninen, and R. Felix, "CT-Guided Interstitial Single-Fraction Brachytherapy of Lung Tumors—Phase I Results of a Novel Technique," *CHEST Journal*, vol. 127, no. 6, pp. 2237–2242, 2005.
- [37] Y. Ohno, H. Hatabu, D. Takenaka, T. Higashino, H. Watanabe, C. Ohbayashi, and K. Sugimura, "CT-guided transthoracic needle aspiration biopsy of small (20 mm) solitary pulmonary nodules," *American Journal of Roentgenology*, vol. 180, no. 6, pp. 1665–1669, 2003.
- [38] A. S. Wright, L. A. Sampson, T. F. Warner, D. M. Mahvi, and F. T. Lee Jr, "Radiofrequency versus microwave ablation in a hepatic porcine model," *Radiology*, vol. 236, no. 1, pp. 132–139, 2005.
- [39] S. Nahum Goldberg, G. Scott Gazelle, L. Solbiati, W. J. Rittman, and P. R. Mueller, "Radiofrequency tissue ablation: increased lesion diameter with a perfusion electrode," *Academic Radiology*, vol. 3, no. 8, pp. 636–644, 1996.
- [40] L. Organ, "Electrophysiologic principles of radiofrequency lesion making," *Stereotactic and Functional Neurosurgery*, vol. 39, no. 2, pp. 69–76, 1976.
- [41] M. G. Skinner, M. N. Iizuka, M. C. Kolios, and M. D. Sherar, "A theoretical comparison of energy sources-microwave, ultrasound and laser-for interstitial thermal therapy," *Physics in Medicine and Biology*, vol. 43, no. 12, p. 3535, 1998.
- [42] P. M. Devlin, *Brachytherapy: applications and techniques*. Lippincott Williams & Wilkins, 2007.
- [43] American Cancer Society, "The History of Cancer," September 2013. [Online]. Available: <http://www.cancer.org>
- [44] K. Cleary, M. Freedman, M. Clifford, D. Lindisch, S. Onda, and L. Jiang, "Image-guided robotic delivery system for precise placement of therapeutic agents," *Journal of Controlled Release*, vol. 74, no. 1, pp. 363–368, 2001.
- [45] D. Stoianovici, L. L. Whitcomb, J. H. Anderson, R. H. Taylor, and L. R. Kavoussi, "A modular surgical robotic system for image guided percutaneous procedures," in *Medical Image Computing and Computer-Assisted Intervention—MICCAI98*, Cambridge, MA, October 11–13, 1998, pp. 404–410.

- [46] A. Patriciu, S. Solomon, L. Kavoussi, and D. Stoianovici, "Robotic Kidney and Spine Percutaneous Procedures Using a New Laser-Based CT Registration Method," in *Medical Image Computing and Computer-Assisted Intervention MICCAI 2001*, vol. 2208, Utrecht, The Netherlands, October 14-17, 2001, pp. 249–257.
- [47] D. Stoianovici, K. Cleary, A. Patriciu, D. Mazilu, A. Stanimir, N. Craciunoiu, V. Watson, and L. Kavoussi, "Acubot: a robot for radiological interventions," *IEEE Transactions on Robotics and Automation*, vol. 19, no. 5, pp. 927–930, 2003.
- [48] K. Cleary, D. Stoianovici, A. Patriciu, D. Mazilu, D. Lindisch, and V. Watson, "Robotically assisted nerve and facet blocks: a cadaveric study," *Academic Radiology*, vol. 9, no. 7, pp. 821–825, 2002.
- [49] P. Berkelman, J. Troccaz, and P. Cinquin, "Body-supported medical robots: a survey," *Journal of Robotics and Mechatronics*, vol. 16, pp. 513–519, 2004.
- [50] P. Berkelman, E. Boidard, P. Cinquin, and J. Troccaz, "LER: The light endoscope robot," in *IEEE/RSJ International Conference on Intelligent Robots and Systems, (IROS 2003)*, vol. 3, Las Vegas, Nevada, October 27–November 1, 2003, pp. 2835–2840.
- [51] A. Seitel, C. J. Walsh, N. C. Hanumara, J.-A. Shepard, A. H. Slocum, H.-P. Meinzer, R. Gupta, and L. Maier-Hein, "Development and evaluation of a new image-based user interface for robot-assisted needle placements with the robopsy system," *Proceedings of the SPIE, Medical Imaging: Visualization, Image-guided Procedures and Modeling*, vol. 7261, p. 72610, 2009.
- [52] B. Maurin, J. Gangloff, B. Bayle, M. de Mathelin, O. Piccin, P. Zanne, C. Doignon, L. Soler, and A. Gangi, "A parallel robotic system with force sensors for percutaneous procedures under CT-guidance," in *Medical Image Computing and Computer-Assisted Intervention—MICCAI 2004*. Saint-Malo, France: Springer, September 26–29, 2004, pp. 176–183.
- [53] P. Berkelman and J. Ma, "A compact modular teleoperated robotic system for laparoscopic surgery," *The International Journal of Robotics Research*, vol. 28, no. 9, pp. 1198–1215, 2009.
- [54] A. Asadian, M. R. Kermani, and R. V. Patel, "Robot-assisted needle steering using a control theoretic approach," *Journal of Intelligent & Robotic Systems*, vol. 62, no. 3–4, pp. 397–418, 2011.
- [55] S. Badaan, D. Petrisor, C. Kim, P. Mozer, D. Mazilu, L. Gruionu, A. Patriciu, K. Cleary, and D. Stoianovici, "Does needle rotation improve lesion targeting?" *The International Journal of Medical Robotics and Computer Assisted Surgery*, vol. 7, no. 2, pp. 138–147, 2011.
- [56] G. Picod, A. Jambon, D. Vinatier, and P. Dubois, "What can the operator actually feel when performing a laparoscopy?" *Surgical Endoscopy and Other Interventional Techniques*, vol. 19, no. 1, pp. 95–100, 2005.

- [57] T. G. Cooper and T. R. Solomon, "Offset remote center manipulator for robotic surgery," September 29, 2009, US Patent 7,594,912.
- [58] R. H. Taylor, J. Funda, B. Eldridge, S. Gomory, K. Gruben, D. LaRose, M. Talamini, L. Kavoussi, and J. Anderson, "A telerobotic assistant for laparoscopic surgery," *IEEE Engineering in Medicine and Biology Magazine*, vol. 14, no. 3, pp. 279–288, 1995.
- [59] M. J. H. Lum, "Kinematic optimization of a 2-DOF spherical mechanism for a minimally invasive surgical robot," Ph.D. dissertation, University of Washington, 2004.
- [60] C.-H. Kuo and J. S. Dai, "Robotics for minimally invasive surgery: a historical review from the perspective of kinematics," in *Proceedings of the International Symposium on History of Machines and Mechanisms*. Springer, 2009, pp. 337–354.
- [61] M. Hadavand, A. Mirbagheri, S. Behzadipour, and F. Farahmand, "A novel remote center of motion mechanism for the force-reflective master robot of haptic tele-surgery systems," *The International Journal of Medical Robotics and Computer Assisted Surgery*, Wiley Online Library, DOI: 10.1002/rcs.1515, 2013.
- [62] T. Yoshikawa, "Manipulability and redundancy control of robotic mechanisms," in *IEEE International Conference on Robotics and Automation. Proceedings*, vol. 2, St. Louis, Missouri, arch 25–28, 1985, pp. 1004–1009.
- [63] G. E. Forsythe and C. B. Moler, *Computer Solution of Linear Algebraic Systems*. Prentice-Hall Englewood Cliffs, NJ, 1967, vol. 7.
- [64] J. K. Salisbury and J. J. Craig, "Articulated hands force control and kinematic issues," *The International Journal of Robotics Research*, vol. 1, no. 1, pp. 4–17, 1982.
- [65] T. Yoshikawa, "Manipulability of robotic mechanisms," *The International Journal of Robotics Research*, vol. 4, no. 2, pp. 3–9, 1985.
- [66] V. Klema and A. Laub, "The singular value decomposition: its computation and some applications," *IEEE Transactions on Automatic Control*, vol. 25, no. 2, pp. 164–176, 1980.

# Curriculum Vitae

**Name:** Mostafa Hadavand

**Post-Secondary Education and Degrees:** Sharif University of Technology  
Tehran, Iran  
2008–2011 M.Sc.,  
Mechanical Engineering

Iran University of Science and Technology  
Tehran, Iran  
2003–2008 B.Sc.,  
Mechanical Engineering

**Honours and Awards:** NSERC CREATE program in Computer-Assisted Medical Interventions (CAMI)  
2012–2014

**Related Work Experience:** Teaching Assistant  
The University of Western Ontario  
2012–2014  
Research Assistant  
The University of Western Ontario  
2012–2014

## Publications:

- **M. Hadavand**, R.V. Patel, M.D. Naish. “A Parallel Remote Center of Motion Mechanism for Needle-Based Medical Interventions.” submitted to *IEEE International Conference on Biomedical Robotics and Biomechatronics (BioRob)*, 2014.
- **Hadavand M.**, Mirbagheri A.R., Behzadipour S., Farahmand F. “A Novel Remote Center of Motion Mechanism for the Force-Reflective Master Robot of Haptic Tele-Surgery Systems”, *International Journal of Medical Robotics and Computer-Assisted Surgery*, 2012.
- **M. Hadavand**, A.R. Mirbagheri and F.Farahmand “Design of a Force-Reflective Master Robot for Haptic Telesurgery Applications: RoboMaster1” *33rd Annual International IEEE EMBS Conference of the IEEE Engineering in Medicine and Biology Society* in Boston Marriott Copley Place, during August 30–September 3, 2011, Boston, MA, USA.